THESIS FOR THE DEGREE OF LICENTIATE OF ENGINEERING IN SOLID AND STRUCTURAL MECHANICS

Computational homogenisation and solution strategies for phase-field fracture

Ritukesh Bharali

CHALMERS
UNIVERSITY OF TECHNOLOGY

Material and Computational Mechanics
Department of Industrial and Materials Science
CHALMERS UNIVERSITY OF TECHNOLOGY
Gothenburg, Sweden, 2021

Computational homogenisation and solution strategies for phase-field fracture

Ritukesh Bharali

Technical Report No. IMS-2021-17
This thesis has been prepared using LaTeX.

Department of Industrial and Materials Science
Chalmers University of Technology
SE-412 96 Gothenburg, Sweden
Phone: +46 (0)31 772 1000
www.chalmers.se

COVER IMAGE: (Left) Multi-scale phase-field fracture model with three different RVEs. (Right) Deformed notched concrete specimen with a hole.

Printed by Chalmers Reproservice
Gothenburg, Sweden, September2021

To my parents.

Computational homogenisation and solution strategies for phase-field fracture

RITUKESH BHARALI
Material and Computational Mechanics
Department of Industrial and Materials Science
Chalmers University of Technology

Abstract

The computational modelling of fracture not only provides a deep insight into the underlying mechanisms that trigger a fracture but also offers information on the post-fracture behaviour (e.g., residual strength) of engineering materials and structures. In this context, the phase-field model for fracture is a popular approach, due to its ability to operate on fixed meshes without the need for explicit tracking of the fracture path, and the straight-forward handling of complex fracture topology. Nevertheless, the model does have its set of computational challenges viz., non-convexity of the energy functional, variational inequality due to fracture irreversibility, and the need for extremely fine meshes to resolve the fracture zone. In the first part of this thesis, two novel methods are proposed to tackle the fracture irreversibility, (i) a micromorphic approach that results in local irreversibile evolution of the phase-field, and (ii) a slack variable approach that replaces the fracture irreversibility inequality constraint with an equivalent equality constraint. Benchmark problems are solved using a monolithic Newton-Raphson solution technique to demonstrate the efficiency of both methods.

The second aspect addressed in this thesis concerns multi-scale problems. In such problems, features such as the micro-cracks are extremely small (several orders of magnitude) compared to the structure itself. Resolving these features may result in a prohibitively computationally expensive problem. In order to address this issue, a computational homogenisation framework for the phase-field fracture is developed. The framework allows the computational of macro (engineering)-scale quantities using different homogenising (averaging) approaches over a microstructure. It is demonstrated that, based on the choice of the homogenisation approaches, local and non-local macro-scale material behaviour is obtained.

Keywords: phase-field fracture, multi-scale, homogenisation, micromorphic, slack variable, irreversibility, brittle, quasi-brittle.

Preface

This thesis is a result of my work in the Materials and Computational Mechanics group, Department of Industrial and Material Science, Chalmers University of Technology, over a period of two and a half years (March 2019 - August 2021). The funding from the Swedish Research Council for Sustainable Development (FORMAS) under Grant 2018-01249 and the Swedish Research Council (VR) under Grant 2017-05192 is gratefully acknowledged.

Acknowledgments

At the outset, I would like to express a sincere gratitude to my supervisors, Prof. Ralf Jänicke and Prof. Fredrik Larsson for accepting me as your doctoral student, and your excellent mentorship towards moulding me into an independent researcher. Thank you for your support and guidance in matters related to computational mechanics and beyond, for your *open-door policy* that meant I was never stuck on something for too long, and for granting the freedom to explore (many a times, outrageous) new ideas. I would also like to thank Prof. Minna Karstunen and Prof. Jelke Dijkstra for willing to be my co-supervisors, and their plan to offer support for the latter part of my doctoral studies.

Furthermore, I would like to thank Jessica Twedmark and Paula Arhanto for excellent administrative and house-hunting support. Göteborg has been a home away from home for the past couple of years, all thanks to the past and present colleagues at Chalmers and the Assamese community in the city. The social activities, be it lunch football, after-work, or road-trips, enabled me to unwind from the monotonous work schedule and kept my sanity intact.

I thank Prof. Christine Räisänen for the excellent 'Writing up for publication' course, from which I greatly benefited. I am also grateful to my former supervisors, Prof. Bert Sluys at TU Delft and Prof. Dan Givoli at Technion, for introducing me to the computational mechanics arena.

My mother has been my pillar of support, strength and inspiration. I am blessed to be her son, and I cannot thank her enough. Finally, I would like to thank my best friend, Amrita, for steering the ship with me through good and bad times, for all the constructive criticism and finding ways to improve ourselves and our productivity, and celebrating our tiny successes.

Acronyms

AT:	Ambrosio-Tortorelli
DBC:	Dirichlet Boundary Condition
FEM:	Finite Element Method
KKT:	Karush-Kuhn-Tucker
LBB:	Ladyzhenskaya–Babuška–Brezzi
NBC:	Neumann Boundary Condition
PFFM:	Phase-field Fracture Model
PFCZM:	Phase-field regularised Cohesive Zone Model
RVE:	Representative Volume Element
SPBC:	Strongly Periodic Boundary Condition
VCH:	Variationally Consistent Homogenisation
WPBC:	Weakly Periodic Boundary Condition

Mathematical symbols

Ω	computational domain
Γ	domain boundary
$\Gamma_D^{\mathbf{u}}$	Dirichlet boundary
$\Gamma_N^{\mathbf{u}}$	Neumann boundary
$\mathbf{u}$	displacement
$\mathbf{u}^p$	prescribed displacement
$\mathbf{t}_p^{\mathbf{u}}$	prescribed traction
$\boldsymbol{\epsilon}$	Symmetric deformation gradient (strain)
$\boldsymbol{\sigma}$	Cauchy stress
Ψ	elastic strain energy density
Ψ^+	fracture driving strain energy density
Ψ^-	residual strain energy density
λ	Lame parameter
μ	Shear modulus
K	Bulk modulus
φ	phase-field
G_c	Griffith fracture energy
l	fracture length-scale
c_w	normalisation constant
θ	slack variable
t	(pseudo) time
$\Omega_\square$	sub-scale (RVE) domain
$\bullet^M$	macro-scale quantity
$\bullet^S$	sub-scale (RVE) quantity
$\langle\bullet\rangle_\square$	volume-averaged (homogenised) quantity
$\bar{\bullet}$	volume-averaged (homogenised) quantity

List of Publications

This thesis is based on the following publications:

[A] **Ritukesh Bharali**, Fredrik Larsson, Ralf Jänicke, "A micromorphic phase-field model for fracture". *Manuscript to be submitted for publication.*

[B] **Ritukesh Bharali**, Fredrik Larsson, Ralf Jänicke, "Phase-field fracture irreversibility using the slack variable approach". *Manuscript to be submitted for publication.*

[C] **Ritukesh Bharali**, Fredrik Larsson, Ralf Jänicke, "Computational homogenisation of phase-field fracture". European Journal of Mechanics - A/Solids, 88, 104247, DOI: `10.1016/j.euromechsol.2021.104247`.

Other publications by the author, not included in this thesis, are:

Ritukesh Bharali, Ralf Jänicke, Fredrik Larsson, 2019, "Computational aspects of the weak micro-periodicity saddle point problem". *PAMM*, 20(1), DOI: `10.1002/pamm.202000259`.

Contents

Abstract i

Preface iii

Acknowledgements iii

Acronyms v

Mathematical symbols vii

List of Papers ix

I Overview 1

1 Introduction 3

1.1 Background 3

1.2 Research objectives 7

1.3 Thesis outline 8

1.4 Computational framework 8

2 Phase-field model for fracture **11**
2.1 Phase-field representation of fracture 11
2.2 Euler-Lagrange equations 15
2.3 Computational challenges 18
2.4 Micromorphic phase-field fracture model 20
2.5 Slack-variable based fracture irreversibility 22
2.6 Discussion 25

3 Multi-scale fracture modelling **29**
3.1 Variationally Consistent Homogenisation 29
3.2 Multi-scale phase-field fracture framework 34
3.3 Discussion 36

4 Summary of included papers **37**
4.1 Paper A 37
4.2 Paper B 38
4.3 Paper C 38

5 Concluding Remarks and Future Work **41**

References **45**

II Papers **59**

Paper A **A1**

Paper B **B1**

Paper C **C1**

Part I

Overview

CHAPTER 1

Introduction

This chapter provides a background for the growing interest in phase-field modelling of fracture. Thereafter, research questions are formulated based on the gaps in the current state-of-the-art. The chapter concludes with sections on the computational framework, thesis outline, and notations adopted.

1.1 Background

"*Why and how do things break/fracture?*" is a fundamental question in the design of engineering structures and materials. Fracture is a common failure mechanism, and is often associated with catastrophic consequences. Popular examples studied in the literature include the breaking of Liberty ships of World War II due to hull and deck fractures [1], and collapse of civil engineering infrastructure (buildings, dams, bridges) due to earthquakes and wind loading [2–6]. However, controlled fracture may also be a desired phenomenon. In this context, a simple example from daily lives would be opening a beverage can. The initiation of fracture is usually traced back to material defects/impurities (weak zones much smaller than the structure itself), that may be introduced in the manufacturing process, workmanship errors, or ex-

posure to adverse environmental/loading conditions. Therefore, an insight into the underlying process(es) triggering a fracture is not only important in preventing the breaking up of engineering structures but also to engineer controlled fracture. In this context, the computational modelling of fracture provides key information, such as the fracture path and the residual strength post-fracture.

The state-of-the-art models for computational modelling of fracture within the finite element method [7, 8] is broadly classified into two categories, discrete models and smeared/continuous models. Fractures are modelled explicitly in discrete models, allowing the displacement field to be discontinuous across a fracture surface. In the case of smeared models, the displacement field is assumed to be continuous and the material strength (stresses) are degraded. Examples of the discrete models include the cohesive zone model [9–11], eXtended Finite Element Method (XFEM) [12–14], and intra-element (embedded) discontinuity approaches [15, 16]. These models are often reliant on *a priori* knowledge of the fracture path, re-meshing techniques to eliminate mesh bias, and additional *ad-hoc* criteria and tedious discontinuity tracking techniques for complex fracture topology (branching, kinking, merging of cracks). As a consequence, the discrete model approach is used for simulating one or more dominant cracks [17], and there is a growing interest in smeared fracture models. Examples of smeared fracture models include the phase-field model for fracture, gradient damage [18, 19], and peridynamics, the first being the focus in this thesis. The reader is referred to [20–22] for a discussion on peridynamics.

The phase-field model for fracture emerged from the Francfort and Marigo's pioneering work on variational approach to Griffith's brittle fracture [23]. A computationally viable implementation of the same was proposed in [24, 25], adopting the Ambrosio-Tortorelli regularisation of the Mumford-Shah potential [26]. With this approach, an auxiliary field variable, the phase-field, is introduced. The phase-field variable is bounded between one and zero, corresponding to total loss of integrity and intact material states respectively. Based on global energy minimisation, the phase-field model does not require additional *ad-hoc* criteria or *a priori* knowledge for fracture initiation, propagation, and for handling topologically complex fracture (branching, kinking, merging of cracks). It also circumvents the need for tedious discontinuity tracking and re-meshing techniques, as it is able to operate on a fixed mesh.

For these reasons, the phase-field model for fracture has grown in popularity over the past decade. Figures 1.1(a) and 1.1(b) illustrates the increasing trend in the number of article published and citations acquired in the past decade (2011-2021). Note that the numbers merely indicate the trend and are not absolutely representative. This is because some researchers also refer to the phase-field fracture model as gradient damage, variational fracture or variational damage models.

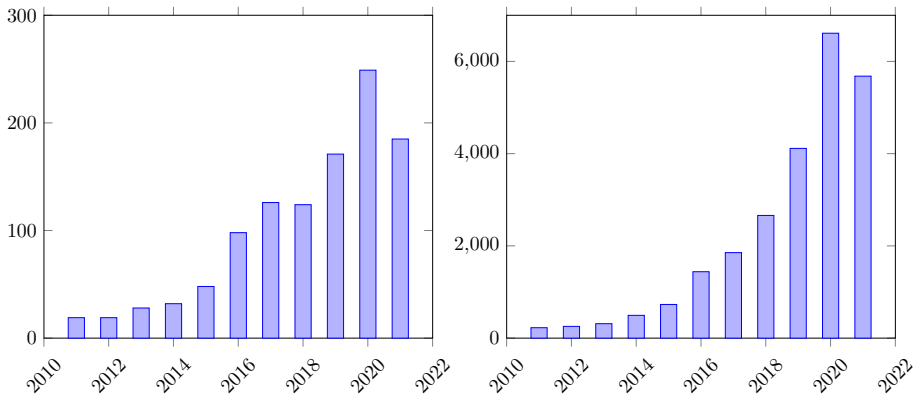

(a) Articles per year **(b)** Citations per year

Figure 1.1: Figure shows (a) articles per year, and (b) citations per year, corresponding to keywords 'phase-field fracture' from the year 2011 until 2021. Data obtained from Scopus on August 11, 2021.

A thermodynamically consistent framework for phase-field fracture model was developed in [27], based on an energetic crack driving criterion. The work was later extended towards generalised stress-based crack driving criterion [28], inclusion of plasticity for modelling ductile fracture [29–32], anisotropic fracture [33, 34], hydraulic fracture [35–37], desiccation cracking [38–40], corrosion [41, 42] in a non-exhaustive list of single-scale brittle fracture applications. Furthermore, [43] proposed a unified phase-field fracture theory capable of modelling both brittle and quasi-brittle fractures.

In the context of multi-scale modelling, concurrent approaches remain popular, with the use of different types of overlapping domain decomposition techniques. For instance, [44, 45] proposed a multi-scale method where a sub-scale domain lives within a coarse element. The multi-scale basis func-

tions are then computed numerically on-the-fly. A similar approach is also adopted by [46, 47]. A larger sub-scale domain adaptively encompassing several elements was proposed in [48, 49] based on a non-intrusive global-local scheme [50]. The aforementioned contributions rely on the equivalence in the length scales of the macro-scale domain and the sub-scale features. However, when there is separation of scales between the macro-scale and the sub-scale domain, concurrent approaches are prohibitively expensive. In such a situation, hierarchical approaches seem to be the only computationally feasible option. In this context, [51] developed a multi-scale model based on offline sub-scale computations, and obtained a closed-form homogenised constitutive tensor based on interpolation of the phase-field variable. Such a method is reliant on offline training phases encompassing all possible fracture evolution topologies. In [52], the homogenised elasticity tensor is computed based on heterogeneous microscopic pore structures. This is a top-down approach with more information, w.r.t. fracture, living on the macro-scale and microstructural cracks are not accounted for. The research gap identified in this regard is a generic hierarchical multi-scale framework, able to model all microstructural features (material heterogenities, microcracks) in the sub-scale, while offering the choice of selectively homogenising macro-scale quantities.

Furthermore, the phase-field model for fracture has its own set of computational challenges, viz., (A) non-convex energy functional simultaneously w.r.t. the displacement and the phase-field variable, (B) variational inequality formulation due to fracture irreversibility, and (C) the requirement of extremely fine meshes in the smeared crack region. In order to alleviate convergence issues of the monolithic solution scheme due to non-convex energy functional (A), [53] proposed a modified line-search method allowing the possibility of a negative line-search parameter. An alternative, robust yet questionable[1] scheme was used in [54] based on linear extrapolation of the phase-field in the momentum balance (equilibrium) equation. Other monolithic solution techniques include the use of dissipation-based arc-length solvers [55–57], modified Newton-Raphson method [58], error-oriented Newton-Raphson method [59], and trust regions methods [60]. However, the development of monolithic solution schemes is still an active area of research as neither of the aforementioned monolithic solution techniques are robust. In an alternative approach, [61] suggested the use of alternative minimisation approach, since the energy

[1] Regularity of the phase-field in time is not established.

functional is convex w.r.t. the displacement field for fixed phase-field and vice-versa. Several researchers have also proposed different techniques for treatment the variational inequality problem (B). These include the penalisation technique [53, 62], primal-dual active set strategy as a semi-smooth Newton method [54], Augmented Lagrangian method based on the Moreau-Yoshida indicator function [58, 59], and the history variable approach proposed by [61]. Apart from the history variable approach, all other methods preserve the variational nature of the phase-field fracture problem. Finally, the phase-field fracture model requires extremely fine meshes to resolve the smeared crack region (C). This can be handled either using uniformly refined mesh or pre-refining the mesh in certain sub-domains if the crack path is known in advance. The use of uniformly refined meshes significantly increases the computational expense and may require parallel computing resources [24]. Alternatively, adaptive mesh refinement techniques are proposed in the literature, based on the phase-field reaching a certain threshold value [54, 63], recovery-based error indicator [64], posteriori error estimation based on the dual-weighted residual method [65], and the local increase of tensile energy [66]. Other approaches include the the finite cell method [67], and dual meshes for displacement and phase-field with different mesh refinement indicators [68].

1.2 Research objectives

The review of literature pertaining to the phase-field model for fracture has revealed critical research gaps and scope for further addition to the current state-of-the-art. They are formulated as research objectives of this thesis, and are presented below:

- Investigate alternative, monolithic solution strategies for the phase-field fracture model, focused on the treatment of fracture irreversibility. In the context of hierarchical FE^2 multi-scale problems, monolithic solution strategies at the RVE level ensures an efficient computation of the homogenised tangent moduli [69].
- Developing a hierarchical multi-scale phase-field fracture framework. The framework should be extensible and capable of accounting for all microstructural features, and provide different homogenisation choices.

The first research objective is treated in Sections 2.4 and 2.5 and in the appended Papers A and B. The second research objective is addressed in Chapter 3 and the appended Paper C.

1.3 Thesis outline

The remaining part of this chapter explains the computational framework developed for this thesis work. Chapter 2 introduces the phase-field model for fracture, followed by the contributions made to the state-of-the-art solution strategies. Thereafter, in Chapter 3, the reader is introduced to the Variationally Consistent Homogenisation (VCH) technique. The VCH technique is then used to develop a multi-scale phase-field fracture framework. Chapter 4 presents the summary of the appended papers. Concluding remarks and future research directions are presented in Chapter 5. Finally, the set of appended papers concludes this thesis.

1.4 Computational framework

The numerical experiments carried out in this thesis comprises of single-scale and multi-scale FE^2 fracture problems. To this end, a computational framework is developed using the commercial finite element software package COMSOL Multiphysics (COMSOL) and the scientific computing software MATLAB. All implementations are open-source and hosted in the author's Github account, `https://github.com/rbharali`.

The single-scale models are developed entirely in COMSOL, using the Solid Mechanics and the Weak Form PDE Interface for the momentum balance equation and the phase-field evolution equation respectively.

The multi-scale FE^2 'openFE2' [70] is more involved as it relies on MATLAB's interaction with COMSOL, and the two-way data transfer between them. COMSOL's Livelink for MATLAB [71] provides an efficient two-way data transfer and also allows controlling the COMSOL model from MATLAB. Furthermore, the package is developed such that the relatively cheaper macro-scale problem is solved in MATLAB, while the sub-scale (RVE) problems are solved in COMSOL, in parallel. Such a setup is possible via the parallel for-loop (parfor) offered by MATLAB's Parallel Computing Toolbox. As illustrated in Figure 1.2, the '*parfor*' command creates several copies of

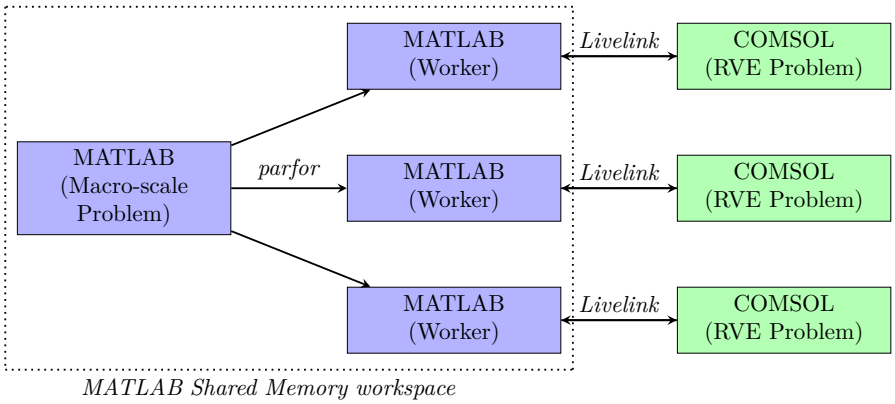

Figure 1.2: An illustration of the MATLAB-COMSOL interaction for a multi-scale FE^2 problem.

the MATLAB program itself, each linked to a COMSOL Server dealing with an RVE problem.

CHAPTER 2

Phase-field model for fracture

In this chapter, the reader is introduced to the main components of the phase-field model for fracture along with pertinent computational challenges. Thereafter, the contribution of this thesis towards the state of the art of solution strategies for phase-field fracture model is presented. This latter part of the chapter is based on Papers A and B.

2.1 Phase-field representation of fracture

The variational approach towards brittle fracture, pioneered by [23], and its regularised formulation introduced in [24, 25] laid down the framework for phase-field representation of fracture. Within this framework, a discrete crack is approximated using a scalar continuous field variable φ that localises into a band of finite width, l. An illustration of this approximation is presented in Figure 2.1, where a continuum body $\Omega \in \mathbb{R}^2$ embedded with a discrete crack is presented in (a) and its phase-field (φ) regularised counterpart is shown in (b). Furthermore, the scalar variable $\varphi : \Omega \longrightarrow [0, 1]$, where zero and one correspond to the intact and fully fractured material phases, with $(0, 1)$ representing the transition zone. This lends the name phase-field model for

fracture[1].

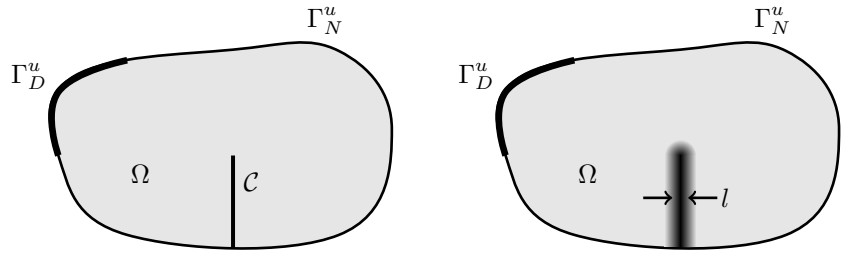

(a) discrete crack **(b)** diffused (smeared) crack

Figure 2.1: A solid $\Omega \in \mathbb{R}^2$ embedded with (a). discrete crack $\mathcal{C}$ and (b). diffused (smeared) crack, with Dirichlet and Neumann boundaries indicated as Γ_D^u and Γ_N^u respectively. Figure reproduced from [72].

The energy functional for the phase-field regularised fracturing continuum in Figure 2.1(b) is described by [24] as,

$$E(\mathbf{u},\varphi) = \int_\Omega g(\varphi)\,\Psi(\boldsymbol{\epsilon}[\mathbf{u}])\,\mathrm{d}\Omega - \int_{\Gamma_N^u} \mathbf{t}_p^u \cdot \mathbf{u}\,\mathrm{d}\Gamma + \int_\Omega \frac{G_c}{c_w}\left(\frac{w(\varphi)}{l} + l|\boldsymbol{\nabla}\varphi|^2\right)\mathrm{d}\Omega, \tag{2.1}$$

in the absence of body forces. In the above equation, $g(\varphi)$ is a degradation function acting on the elastic strain energy density Ψ, $\mathbf{t}_p^u$ denotes the prescribed traction over the boundary Γ_N^u, G_c is the Griffith fracture toughness, c_w is a normalisation constant linked with the choice of locally dissipated fracture energy $w(\varphi)$ [73]. Moreover, $\boldsymbol{\epsilon}[\mathbf{u}]$ is the symmetric part of the deformation gradient, $\mathbf{u}$ being the displacement.

The choice of the degradation function $g(\varphi)$ and the local part of the dissipated fracture energy $w(\varphi)$ plays an important role in the observed fracture phenomenon. Even though there is a flexibility in choosing $g(\varphi)$, it is required to meet the following criteria:

- $g(0) = 1$ and $g(1) = 0$, since $\varphi = 0$ and 1 represent the intact material

[1]The similarity of the phase-field variable with damage in terms of representing loss of material integrity has led to many researchers using the term 'phase-field damage' or 'gradient damage'.

state and total loss of integrity respectively,

- $g'(\varphi) < 0$, for a strictly decreasing monotone, and
- $g'(1) = 0$, in order to ensure that the energy converges to a finite value for a fractured material state.

The criterion $g'(1) = 0$ ensures a zero crack driving force in the event of a fully developed fracture, i.e., $\varphi = 1$. This prevents the growth of the localisation band in the orthogonal direction, a phenomenon observed in classical non-local/gradient-enhanced damage models [74]. Table 2.1 presents some frequently used degradation functions for phase-field fracture problems along with their contributors. The quadratic degradation function suggested by [24] is a popular choice for modelling brittle fracture, whereas the polynomials proposed by [75] and [43] are adopted for quasi-brittle fracture. These models involve additional material parameters (p,a_1,a_2,a_3), and the reader is referred to the corresponding manuscripts for more details.

$g(\varphi)$	Contribution
$(1-\varphi)^2$	Bourdin et. al., [24]
$3(1-\varphi)^2 - 2(1-\varphi)^3$	Borden et. al., [76]
$\dfrac{(1-\varphi)^2}{(1-\varphi)^2 + \varphi + p\,\varphi^2}$	Lorentz and Godard, [75]
$\dfrac{(1-\varphi)^p}{(1-\varphi)^p + a_1\varphi + a_1a_2\varphi^2 + a_1a_2a_3\varphi^3}$	Wu, [43]

Table 2.1: Commonly used degradation functions in the phase-field fracture literature

Abbreviated name	$w(\varphi)$	c_w
AT1	φ	$8/3$
AT2	φ^2	2
PFCZM	$2\varphi - \varphi^2$	π

Table 2.2: Commonly used local fracture energy functions in the phase-field fracture literature

Furthermore, the commonly used local dissipation fracture energy functions, $w(\varphi)$ is presented in Table 2.2. Here, AT and PFCZM are abbreviations for Ambrosio-Tortorelli [77] and Phase-Field regularised Cohesive Zone Model [43] respectively. While the AT2 model lacks an initial elastic stage, in AT1 and PFCZM an elastic stage precedes the onset of phase-field fracture evolution.

Remark. *Papers A, B and C in this thesis deal with brittle fracture, as such, the quadratic degradation function [24] is adopted along with the AT2 model. Refer to Tables 2.1 and 2.2 for the explicit expressions.*

Strain energy density split

In the energy functional (2.1), proposed by [24], the degradation function $g(\varphi)$ is applied to the entire strain energy density term, Ψ. In such a model, the total strain, irrespective of its tensile or compressive nature, contributes to the evolution of the phase-field. As a consequence, the model has (i) an unrealistic symmetric behaviour in terms of crack propagation under tension and compression, and (ii) possible crack interpenetration under compressive loading [78]. In order to alleviate the aforementioned drawbacks, several researchers have proposed an additive decomposition of the strain energy density into a crack driving part Ψ^+, and a residual part Ψ^- [61, 79, 80]. Thereafter, the degradation function is attached only to Ψ^+. Table 2.3 provides the frequently adopted strain energy density decompositions in the phase-field literature.

Ψ^+	Ψ^-	Contribution
$\mu\,\boldsymbol{\epsilon}_{dev} : \boldsymbol{\epsilon}_{dev}$	$\frac{1}{2}K tr^2(\boldsymbol{\epsilon})$	Lancioni and Royer-Carfagni [79]
$\frac{1}{2}K\langle tr(\boldsymbol{\epsilon})\rangle_+^2 + \mu\,\boldsymbol{\epsilon}_{dev} : \boldsymbol{\epsilon}_{dev}$	$\frac{1}{2}K\langle tr(\boldsymbol{\epsilon})\rangle_-^2$	Amor et. al. [80]
$\frac{1}{2}\lambda\langle tr(\boldsymbol{\epsilon})\rangle_+^2 + \mu\,\boldsymbol{\epsilon}^+ : \boldsymbol{\epsilon}^+$	$\frac{1}{2}\lambda\langle tr(\boldsymbol{\epsilon})\rangle_-^2 + \mu\,\boldsymbol{\epsilon}^- : \boldsymbol{\epsilon}^-$	Miehe et. al. [61]

Table 2.3: Frequently adopted strain energy density decompositions in the phase-field fracture literature

In the context of Table 2.3, K, λ and μ are material constants representing the bulk modulus, Lamé constant and shear modulus respectively. The trace operator is given by tr, while $\langle\bullet\rangle_\pm$ represents the positive/negative Macaulay brackets. The latter is given by $0.5(\bullet \pm |\bullet|)$, where $|\bullet|$ indicates the absolute value of '$\bullet$'. Furthermore, $\boldsymbol{\epsilon}_{dev}$ is the deviatoric strain tensor, and $\boldsymbol{\epsilon}^\pm$ indicates

the tensile/compressive strain tensors, obtained through spectral decomposition of the strain tensor.

The use of any of the strain energy density decompositions from Table 2.3 modifies the phase-field fracture energy functional (2.1), resulting in

$$\begin{aligned} E(\mathbf{u},\varphi) = &\int_\Omega g(\varphi)\Psi^+(\boldsymbol{\epsilon}[\mathbf{u}])\,\mathrm{d}\Omega + \int_\Omega \Psi^-(\boldsymbol{\epsilon}[\mathbf{u}])\,\mathrm{d}\Omega - \int_{\Gamma_N^u} \mathbf{t}_p^u \cdot \mathbf{u}\,\mathrm{d}\Gamma \\ &+ \int_\Omega \frac{G_c}{c_w}\left(\frac{w(\varphi)}{l} + l|\boldsymbol{\nabla}\varphi|^2\right)\mathrm{d}\Omega \end{aligned} \tag{2.2}$$

Remark. *The tension-compression strain energy density decomposition proposed in [61] is used in this thesis, owing to its popularity in modelling brittle fracture. The author is aware of the limitations and drawbacks of this decomposition, discussed in [78, 81].*

2.2 Euler-Lagrange equations

The Euler-Lagrange[2] equations for the phase-field fracture problem is derived upon minimising the energy functional (2.2) w.r.t. its solution fields, vector-valued displacement $\mathbf{u}$, and scalar-valued phase-field φ. This results in the compact form:

Problem 1. *For $\mathbf{u}(t)$ and $\varphi(t)$ defined in appropriate spaces, and in (pseudo) time $t \in [0, T]$,*

$$\arg\,\min_{\mathbf{u}(t),\varphi(t)}\; E(\mathbf{u}(t),\varphi(t)) \quad s.t. \quad \partial_t\varphi \geq 0. \tag{2.3}$$

Here, T refers to the final time in a simulation, and the inequality constraint $\partial_t\varphi \geq 0$ corresponds to fracture irreversibility (no healing of crack is allowed). ■

Elaborating on the minimisation process, taking the first variation of the energy functional (2.2) w.r.t. the displacement $\mathbf{u}$ yields the momentum balance equation (2.4a), while a variation w.r.t the phase-field φ results in the phase-field evolution equation (2.4b). Moreover, the inequality constraint in (2.3) manifests in the form of a variational inequality (2.4b). With appropriately

[2] Also referred to as 'space-variational form' or 'weak equations'

defined test and trial Sobolev[3] spaces H^1, the complete problem statement takes the form:

Problem 2. *Find* $(\mathbf{u}, \varphi) \in \mathbb{U} \times \mathbb{P}$ *with*

$$E'(\mathbf{u}, \varphi; \delta\mathbf{u}) = \int_\Omega \left(g(\varphi) \frac{\partial \Psi^+(\boldsymbol{\epsilon}[\mathbf{u}])}{\partial \boldsymbol{\epsilon}} + \frac{\partial \Psi^-(\boldsymbol{\epsilon}[\mathbf{u}])}{\partial \boldsymbol{\epsilon}} \right) : \boldsymbol{\epsilon}[\delta\mathbf{u}] \, \mathrm{d}\Omega \tag{2.4a}$$

$$- \int_{\Gamma_N^u} \mathbf{t}_p^u \cdot \delta\mathbf{u} \, \mathrm{d}\Gamma = 0 \qquad \forall \, \delta\mathbf{u} \in \mathbb{U}^0$$

$$E'(\mathbf{u}, \varphi; \hat{\varphi}) = \int_\Omega \left(g'(\varphi) \Psi^+(\boldsymbol{\epsilon}[\mathbf{u}]) + \frac{G_c}{c_w \, l} w'(\varphi) \right) (\hat{\varphi} - \varphi) \, \mathrm{d}\Omega \tag{2.4b}$$

$$+ \int_\Omega \frac{G_c l}{c_w} \boldsymbol{\nabla}\varphi \cdot \boldsymbol{\nabla}(\hat{\varphi} - \varphi) \, \mathrm{d}\Omega \geq 0 \qquad \forall \, \hat{\varphi} \in \mathbb{P}$$

using pertinent time-dependent Dirichlet boundary conditions $\mathbf{u}^p$ *on* Γ_D^u *and* φ^p *on* Γ_D^φ*, and Neumann boundary condition* $\mathbf{t}_p^u$ *on* Γ_N^u*. The trial and test spaces are defined as*

$$\mathbb{U} = \{\mathbf{u} \in [H^1(\Omega)]^{\dim} | \mathbf{u} = \mathbf{u}^p \ \textit{on} \ \Gamma_D^u\}, \tag{2.5a}$$

$$\mathbb{U}^0 = \{\mathbf{u} \in [H^1(\Omega)]^{\dim} | \mathbf{u} = \mathbf{0} \ \textit{on} \ \Gamma_D^u\}, \tag{2.5b}$$

$$\mathbb{P} = \{\varphi \in [H^1(\Omega)] | \varphi \geq {}^n\varphi | \varphi = \varphi^p \ \textit{on} \ \Gamma_D^\varphi\}. \tag{2.5c}$$

In (2.5c), the left superscript n refers to the previous time-step. ■

As mentioned earlier, the phase-field evolution equation (2.4b) belongs to the variational inequality category. The treatment of variational inequality is not new to the mathematics literature, as such, several techniques from optimisation theory made its way into the phase-field fracture models. In this regard, a penalisation approach was suggested in [53, 62], whereas [54] opted for the primal-dual active set strategy as a semi-smooth Newton method, and [58, 59] adopted Augmented Lagrangian formulations based on the Moreau-Yoshida indicator function. Other techniques include inequality enforcement via Dirichlet constraints in [24, 25, 83], and interior point methods in [84]. An alternative, rather 'heuristic' approach was proposed by [61], where the cracking driving energy Ψ^+ is replaced by its maximum value over the loading

[3] A function u for which $\int_\Omega (u)^2 + (\boldsymbol{\nabla} u)^2 < \infty$, belongs to Sobolev space of degree one, denoted by H^1. For more on function spaces, the reader is referred to [82].

history. This maximum value of Ψ^+ is stored in an implicit 'history variable' $\mathcal{H}$. Mathematically,

$$\mathcal{H} = \max_{[0,t]} \Psi^+(t), \tag{2.6}$$

where t is the current (pseudo) time. Incorporating $\mathcal{H}$ in (2.4b) transforms Problem 2 into a variational equality problem given by:

Problem 3. *Find* $(\mathbf{u}, \varphi) \in \mathbb{U} \times \mathbb{P}$ *with*

$$E'(\mathbf{u}, \varphi; \delta\mathbf{u}) = \int_\Omega \left(g(\varphi) \frac{\partial \Psi^+(\boldsymbol{\epsilon}[\mathbf{u}])}{\partial \boldsymbol{\epsilon}} + \frac{\partial \Psi^-(\boldsymbol{\epsilon}[\mathbf{u}])}{\partial \boldsymbol{\epsilon}} \right) : \boldsymbol{\epsilon}[\delta\mathbf{u}] \, \mathrm{d}\Omega \tag{2.7a}$$

$$- \int_{\Gamma_N^u} \mathbf{t}_p^u \cdot \delta\mathbf{u} \, \mathrm{d}\Gamma = 0 \qquad \forall \, \delta\mathbf{u} \in \mathbb{U}^0$$

$$E'(\mathbf{u}, \varphi; \delta\varphi) = \int_\Omega \left(g'(\varphi)\mathcal{H} + \frac{G_c}{c_w \, l} w'(\varphi) \right) \delta\varphi \, \mathrm{d}\Omega \tag{2.7b}$$

$$+ \int_\Omega \frac{G_c l}{c_w} \boldsymbol{\nabla}\varphi \cdot \boldsymbol{\nabla}\delta\varphi \, \mathrm{d}\Omega = 0 \qquad \forall \, \delta\varphi \in \mathbb{P}^0$$

using pertinent time-dependent Dirichlet boundary conditions $\mathbf{u}^p$ *on* Γ_D^u *and* φ^p *on* Γ_D^φ*, and Neumann boundary condition* $\mathbf{t}_p^u$ *on* Γ_N^u*. The trial and test spaces are defined as*

$$\mathbb{U} = \{\mathbf{u} \in [H^1(\Omega)]^{\dim} | \mathbf{u} = \mathbf{u}^p \text{ on } \Gamma_D^u\}, \tag{2.8a}$$

$$\mathbb{U}^0 = \{\mathbf{u} \in [H^1(\Omega)]^{\dim} | \mathbf{u} = \mathbf{0} \text{ on } \Gamma_D^u\}, \tag{2.8b}$$

$$\mathbb{P} = \{\varphi \in [H^1(\Omega)] | \varphi = \varphi^p \text{ on } \Gamma_D^\varphi\}, \tag{2.8c}$$

$$\mathbb{P}^0 = \{\varphi \in [H^1(\Omega)] | \varphi = 0 \text{ on } \Gamma_D^\varphi\}. \tag{2.8d}$$

■

Remark. *With the use of the implicit 'history variable' in Problem 3, the variational consistency is lost. In particular, there is no proof that the solution to (2.7b) corresponds to minimisation of the energy functional (2.2). However, the use of the history variable relaxes the function space for the phase-field and its test function (cf. (2.5c) with (2.8c), (2.8d)).*

2.3 Computational challenges

The phase-field model for fracture comes with its set of computational challenges, viz., (A) non-convex energy functional simultaneously w.r.t. the displacement and phase-field variables, (B) fracture irreversibility and associated variational inequality formulation (2.4b), and (C) the requirement for extremely fine meshes in the diffused (smeared) crack region of the continuum (see Figure 2.1(b)). The treatment of the aforementioned challenges in this thesis is presented in the next sub-sections.

(A) Non-convex energy functional

The phase-field fracture energy functional (2.2) is non-convex simultaneously w.r.t the displacement $\mathbf{u}$ and the phase-field φ. This can be observed from the integrand of the first integral in (2.2), i.e., $g(\varphi)\Psi^{+}(\boldsymbol{\epsilon}[\mathbf{u}])$, where $g(\varphi)$ is a second or higher order polynomial in φ, and Ψ^{+} being quadratic w.r.t to the strain $\boldsymbol{\epsilon}[\mathbf{u}]$.

A non-convex energy functional impacts the robustness of fully coupled solution techniques (e.g., Newton-Raphson method) due to a possible indefinite Hessian. However, the energy functional is convex w.r.t. $\mathbf{u}$ and φ individually while keeping the other fixed. This has enabled the use of the robust alternate minimisation[4] solution technique, a popular approach in the phase-field fracture literature [24, 25, 61]. Irrespective of solution techniques, there is no guarantee that a solution corresponding to a stationary (critical) point is the global minimum. In order to prove otherwise, every stationary point has to be assessed. Despite the uncertainties w.r.t. the global minimum, several researchers have used fully coupled and alternate minimisation solvers for fracture problems. In this thesis too, Papers A and B adopt the fully coupled Newton-Raphson method, while in Paper C, the alternate minimisation solver is used.

(B) Fracture irreversibility

The concept of fracture irreversibility hinges on the fact that no healing of cracks is permitted. In that sense, it is similar to Continuum Damage Mechanics (CDM) where the damage variable is considered irreversible. However, in

[4]The term 'alternate minimisation' has been used interchangeably with 'staggered solver' in the phase-field literature.

the case of CDM, the damage variable is local, as such the enforcement of irreversibility constraints using the Karush-Kuhn-Tucker (KKT) conditions is simpler. For the phase-field fracture model, the phase-field variable is a global field quantity with regular requirement pertaining to the existence of its derivative. Therefore, the KKT conditions apply in a global sense, yielding a variational inequality problem (see Problem 2).

In this thesis, alternative methods are explored for the enforcement of fracture irreversibility for the phase-field fracture problem. In Paper A, a micromorphic extension of the phase-field fracture energy functional is carried out in the spirit of [85]. Consequently, the phase-field variable is local, while a micromorphic variable regularises the fracture problem. The energy functional and the Euler-Lagrange equations are presented in Section 2.4. For numerical experiments in brittle fracture, the reader in referred to the Paper A.

Adopting an alternative strategy, the fracture irreversibility (inequality) constraint is transformed into an equality constraint using a slack variable approach [86–88]. Thereafter, the constraint is introduced into the phase-field fracture energy functional 2.2 using Method of Multipliers and the Penalisation method. Section 2.5 presents the mathematical details. Numerical experiments in brittle fracture is carried out in Paper B.

(C) Extremely fine mesh

The finite element implementation of the phase-field model for fracture requires an extremely fine mesh to resolve the diffused (smeared) crack region. In this context, an upper bound, half of the fracture length-scale was proposed by [27] for elements in the crack region. When the crack path is known in advance, pre-refining the mesh in selective parts of the computational domain is an easier approach. For Papers A and B, the numerical experiments on benchmark problems are carried out on pre-refined meshes since the crack path is known '*a priori*'. However, for certain Representative Volume Elements (RVEs) in Paper C, uniformly refined meshes were used as the crack path was not known in advance.

2.4 Micromorphic phase-field fracture model

A micromorphic extension of the energy functional (2.2) based on [85] assumes the form,

$$\begin{aligned} E(\mathbf{u},\varphi,d) = &\int_\Omega g(\varphi)\Psi^+(\boldsymbol{\epsilon}[\mathbf{u}])\,\mathrm{d}\Omega + \int_\Omega \Psi^-(\boldsymbol{\epsilon}[\mathbf{u}])\,\mathrm{d}\Omega - \int_{\Gamma_N^u} \mathbf{t}_p^u \cdot \mathbf{u}\,\mathrm{d}\Gamma \\ &+ \int_\Omega \frac{G_c}{c_w}\left(\frac{w(\varphi)}{l} + l|\boldsymbol{\nabla} d|^2\right)\mathrm{d}\Omega + \int_\Omega \frac{\alpha}{2}(\varphi - d)^2\,\mathrm{d}\Omega, \end{aligned} \tag{2.9}$$

where a new micromorphic variable d is introduced, that appears in the gradient term of the fracture energy. This modification comes at the cost of introducing an energy associated with the difference between the phase-field and the micromorphic variable. In the limit $(\varphi - d) \longrightarrow 0$, the original phase-field fracture energy functional (2.2) is recovered.

The first variation of the energy functional (2.9) w.r.t its solution variables $\mathbf{u}$, φ and d, along with the fracture irreversibility constraint $\partial_t \varphi \geq 0$ results in,

$$\begin{aligned} E'(\mathbf{u},\varphi,d;\delta\mathbf{u}) = &\int_\Omega \left(g(\varphi)\frac{\partial \Psi^+(\boldsymbol{\epsilon}[\mathbf{u}])}{\partial \boldsymbol{\epsilon}} + \frac{\partial \Psi^-(\boldsymbol{\epsilon}[\mathbf{u}])}{\partial \boldsymbol{\epsilon}}\right) : \boldsymbol{\epsilon}[\delta\mathbf{u}]\,\mathrm{d}\Omega \\ &- \int_{\Gamma_N^u} \mathbf{t}_p^u \cdot \delta\mathbf{u}\,\mathrm{d}\Gamma = 0 \end{aligned} \tag{2.10a}$$

$$\begin{aligned} E'(\mathbf{u},\varphi,d;\delta\varphi) = &\int_\Omega \left(g'(\varphi)\Psi^+(\boldsymbol{\epsilon}[\mathbf{u}]) + \frac{G_c}{c_w\, l} w'(\varphi)\right)(\hat{\varphi} - \varphi)\,\mathrm{d}\Omega \\ &+ \int_\Omega \alpha(\varphi - d)(\hat{\varphi} - \varphi)\,\mathrm{d}\Omega \geq 0 \end{aligned} \tag{2.10b}$$

$$\begin{aligned} E'(\mathbf{u},\varphi,d;\delta d) = &\int_\Omega G_c l \boldsymbol{\nabla} d \cdot \boldsymbol{\nabla}\delta d\,\mathrm{d}\Omega \\ &- \int_\Omega \alpha(\varphi - d)\delta d\,\mathrm{d}\Omega = 0. \end{aligned} \tag{2.10c}$$

These equations constitute the Euler-Lagrange form for the micromorphic phase-field model for fracture. However, the test and trial spaces are yet to be defined. For the momentum balance equation (2.10a) and the micromorphic

variable equation (2.10c), the function spaces must belong to the H^1 Sobolev space, due to the presence of gradient terms involving $\mathbf{u}$ and d. However, the phase-field evolution equation (2.10b) is local, as such φ can be computed on Gauss (integration) points in the computational domain. In particular, the root(s) of

$$g'(\varphi)\Psi^+(\boldsymbol{\epsilon}[\mathbf{u}]) + \frac{G_c}{c_w l} w'(\varphi) + \alpha(\varphi - d) = 0 \tag{2.11}$$

yields the phase-field φ, if ${}^n\varphi < \varphi < 1$. Equipped with the locally computed phase-field, the complete problem statement for micromorphic phase-field fracture takes the form:

Problem 4. *Find* $(\mathbf{u},\, d) \in \mathbb{U} \times \mathbb{D}$ *with*

$$E'(\mathbf{u}, d; \delta\mathbf{u}) = \int_\Omega \left(g(\varphi) \frac{\partial \Psi^+(\boldsymbol{\epsilon}[\mathbf{u}])}{\partial \boldsymbol{\epsilon}} + \frac{\partial \Psi^-(\boldsymbol{\epsilon}[\mathbf{u}])}{\partial \boldsymbol{\epsilon}} \right) : \boldsymbol{\epsilon}[\delta\mathbf{u}] \, \mathrm{d}\Omega \tag{2.12a}$$

$$- \int_{\Gamma_N^u} \mathbf{t}_p^u \cdot \delta\mathbf{u} \, \mathrm{d}\Gamma = 0 \qquad \forall\, \delta\mathbf{u} \in \mathbb{U}^0$$

$$E'(\mathbf{u}, d; \delta d) = \int_\Omega \frac{G_c l}{c_w} \boldsymbol{\nabla} d \cdot \boldsymbol{\nabla} \delta d \, \mathrm{d}\Omega \tag{2.12b}$$

$$- \int_\Omega \alpha(\varphi - d)\delta d \, \mathrm{d}\Omega = 0 \qquad \forall\, \delta d \in \mathbb{D}^0$$

using pertinent time-dependent Dirichlet boundary conditions $\mathbf{u}^p$ *on* Γ_D^u*, and Neumann boundary condition* $\mathbf{t}_p^u$ *on* Γ_N^u*. The trial and test spaces are defined as*

$$\mathbb{U} = \{\mathbf{u} \in [H^1(\Omega)]^{\dim} | \mathbf{u} = \mathbf{u}^p \ \textit{on}\ \Gamma_D^u\}, \tag{2.13a}$$

$$\mathbb{U}^0 = \{\mathbf{u} \in [H^1(\Omega)]^{\dim} | \mathbf{u} = \mathbf{0} \ \textit{on}\ \Gamma_D^u\}, \tag{2.13b}$$

$$\mathbb{D} = \{d \in [H^1(\Omega)] | d = d^p \ \textit{on}\ \Gamma_D^d\}, \tag{2.13c}$$

$$\mathbb{D}^0 = \{d \in [H^1(\Omega)] | d = 0 \ \textit{on}\ \Gamma_D^d\}. \tag{2.13d}$$

■

Remark. *Problem 4 maintains the generic format w.r.t. the choice of degradation function* $g(\varphi)$ *and the local fracture energy function* $w(\varphi)$*. However, there is a possibility of multiple solutions for* φ *if the order of* $g(\varphi)$ *and/or*

$w(\varphi)$ is greater than 2. For brittle fracture AT1 and AT2 models with the quadratic degradation function (see Table 2.1), the issue of multiple solutions is circumvented. As such, the AT2 model is adopted for Paper A. For AT1,

$$\varphi = \min\left(\max\left(\frac{2\Psi^{+} + \alpha d - \frac{3G_c}{8l}}{2\Psi^{+} + \alpha}, {}^{n}\varphi\right), 1\right), \tag{2.14}$$

and for AT2,

$$\varphi = \min\left(\max\left(\frac{2\Psi^{+} + \alpha d}{2\Psi^{+} + \alpha + \frac{G_c}{l}}, {}^{n}\varphi\right), 1\right). \tag{2.15}$$

2.5 Slack-variable based fracture irreversibility

The use of slack variable is popular in the optimisation theory for converting inequality constraints into equality constraints [87, 88]. Adopting this approach, the phase-field fracture irreversibility constraint,

$$h(\varphi) = \partial_t \varphi \geq 0 \quad \text{or} \quad \varphi - {}^{n}\varphi \geq 0, \tag{2.16}$$

could be converted into an equivalent equality constraint of the form

$$h(\varphi) - \theta^2 = 0, \tag{2.17}$$

where θ is the slack variable. By construction, $\theta^2 \geq 0$, thereby fulfilling the phase-field fracture irreversibility constraint (2.16). In the next sub-sections, the introduction of the irreversibility constraint (2.17) into the phase-field fracture energy functional (2.2) by means of Method of Multipliers and the Penalisation method are discussed.

Method of Multipliers

The augmentation of the phase-field fracture energy functional (2.2) with the irreversibility constraint (2.17) via the Lagrange multiplier Λ, results in

$$E(\mathbf{u},\varphi,\theta,\Lambda) = \int_\Omega g(\varphi)\Psi^+(\boldsymbol{\epsilon}[\mathbf{u}])\,\mathrm{d}\Omega + \int_\Omega \Psi^-(\boldsymbol{\epsilon}[\mathbf{u}])\,\mathrm{d}\Omega - \int_{\Gamma^u_N} \mathbf{t}^u_p \cdot \mathbf{u}\,\mathrm{d}\Gamma + \int_\Omega \frac{G_c}{c_w}\left(\frac{w(\varphi)}{l} + l|\boldsymbol{\nabla}\varphi|^2\right)\mathrm{d}\Omega + \int_\Omega \Lambda\big(h(\varphi)-\theta^2\big)\,\mathrm{d}\Omega, \tag{2.18}$$

where Λ is the Lagrange multiplier. Similar to the previous section, the Euler-Lagrange equations are obtained on taking the first variation of the energy functional (2.18) w.r.t. the solution variables. With appropriately defined test and trial spaces (H^1 Sobolev space for $\mathbf{u}$ and φ, and L^2 Lebesgue space for θ and Λ), the complete problem statement takes the form:

Problem 5. *Find ($\mathbf{u}$, φ, θ, Λ) $\in \mathbb{U}\times\mathbb{P}\times\mathbb{T}\times\mathbb{A}$ with*

$$E'(\mathbf{u},\varphi,\theta,\Lambda;\delta\mathbf{u}) = \int_\Omega \left(g(\varphi)\frac{\partial\Psi^+(\boldsymbol{\epsilon}[\mathbf{u}])}{\partial\boldsymbol{\epsilon}} + \frac{\partial\Psi^-(\boldsymbol{\epsilon}[\mathbf{u}])}{\partial\boldsymbol{\epsilon}}\right) : \boldsymbol{\epsilon}[\delta\mathbf{u}]\,\mathrm{d}\Omega \tag{2.19a}$$
$$- \int_{\Gamma^u_N} \mathbf{t}^u_p \cdot \delta\mathbf{u}\,\mathrm{d}\Gamma = 0 \qquad \forall\,\delta\mathbf{u}\in\mathbb{U}^0$$
$$E'(\mathbf{u},\varphi,\theta,\Lambda;\delta\varphi) = \int_\Omega \left(g'(\varphi)\Psi^+ + \frac{G_c}{c_w\,l}w'(\varphi) + \Lambda\right)\delta\varphi\,\mathrm{d}\Omega \tag{2.19b}$$
$$+ \int_\Omega \frac{G_c l}{c_w}\boldsymbol{\nabla}\varphi\cdot\boldsymbol{\nabla}\delta\varphi\,\mathrm{d}\Omega = 0 \qquad \forall\,\delta\varphi\in\mathbb{P}^0$$
$$E'(\mathbf{u},\varphi,\theta,\Lambda;\delta\theta) = \int_\Omega -2\Lambda\theta\delta\theta = 0\,\mathrm{d}\Omega \qquad \forall\,\delta\theta\in\mathbb{T} \tag{2.19c}$$
$$E'(\mathbf{u},\varphi,\theta,\Lambda;\delta\Lambda) = \int_\Omega \big(h(\varphi)-\theta^2\big)\delta\Lambda = 0\,\mathrm{d}\Omega \qquad \forall\,\delta\Lambda\in\mathbb{A} \tag{2.19d}$$

using pertinent time-dependent Dirichlet boundary conditions $\mathbf{u}^p$ on Γ^u_D, and Neumann boundary condition $\mathbf{t}^u_p$ on Γ^u_N. The trial and test spaces are defined as

$$\mathbb{U} = \{\mathbf{u}\in[H^1(\Omega)]^{\dim}|\mathbf{u}=\mathbf{u}^p \text{ on } \Gamma^u_D\}, \tag{2.20a}$$
$$\mathbb{U}^0 = \{\mathbf{u}\in[H^1(\Omega)]^{\dim}|\mathbf{u}=\mathbf{0} \text{ on } \Gamma^u_D\}, \tag{2.20b}$$

$$\mathbb{P} = \{\varphi \in [H^1(\Omega)] | \varphi = \varphi^p \ on \ \Gamma_D^\varphi\}, \tag{2.20c}$$
$$\mathbb{P}^0 = \{\varphi \in [H^1(\Omega)] | \varphi = 0 \ on \ \Gamma_D^\varphi\}. \tag{2.20d}$$
$$\mathbb{T} = \{\theta \in [L^2(\Omega)]\}. \tag{2.20e}$$
$$\mathbb{A} = \{\Lambda \in [L^2(\Omega)]\}. \tag{2.20f}$$

■

Penalisation method

Adopting the Penalisation method, the irreversibility constraint (2.17) is added to the phase-field fracture energy functional (2.2) using a penalty parameter η. This results in,

$$\begin{aligned} E(\mathbf{u},\varphi,\theta) = &\int_\Omega g(\varphi)\Psi^+(\boldsymbol{\epsilon}[\mathbf{u}])\,\mathrm{d}\Omega + \int_\Omega \Psi^-(\boldsymbol{\epsilon}[\mathbf{u}])\,\mathrm{d}\Omega - \int_{\Gamma_N^u} \mathbf{t}_p^u \cdot \mathbf{u}\,\mathrm{d}\Gamma \\ &+ \int_\Omega \frac{G_c}{c_w}\left(\frac{w(\varphi)}{l} + l|\boldsymbol{\nabla}\varphi|^2\right)\mathrm{d}\Omega + \int_\Omega \frac{\eta}{2}||\big(h(\varphi)-\theta^2\big)||^2\,\mathrm{d}\Omega. \end{aligned} \tag{2.21}$$

Next, the Euler-Lagrange equations are derived upon taking the first variation of the energy functional (2.21) w.r.t the solution variables. Along with appropriately defined test and trial spaces (H^1 Sobolev space for $\mathbf{u}$ and φ, and L^2 Lebesgue space for θ), the complete problem statement takes the form:

Problem 6. *Find* $(\mathbf{u},\ \varphi,\ \theta) \in \mathbb{U} \times \mathbb{P} \times \mathbb{T}$ *with*

$$E'(\mathbf{u},\varphi,\theta;\delta\mathbf{u}) = \int_\Omega \left(g(\varphi)\frac{\partial\Psi^+(\boldsymbol{\epsilon}[\mathbf{u}])}{\partial\boldsymbol{\epsilon}} + \frac{\partial\Psi^-(\boldsymbol{\epsilon}[\mathbf{u}])}{\partial\boldsymbol{\epsilon}}\right) : \boldsymbol{\epsilon}[\delta\mathbf{u}]\,\mathrm{d}\Omega \tag{2.22a}$$
$$- \int_{\Gamma_N^u} \mathbf{t}_p^u \cdot \delta\mathbf{u}\,\mathrm{d}\Gamma = 0 \qquad \forall\, \delta\mathbf{u} \in \mathbb{U}^0$$
$$E'(\mathbf{u},\varphi,\theta;\delta\varphi) = \int_\Omega \left(g'(\varphi)\Psi^+ + \frac{G_c}{c_w\,l}w'(\varphi) + \eta\big(h(\varphi)-\theta^2\big)\right)\delta\varphi\,\mathrm{d}\Omega \tag{2.22b}$$
$$+ \int_\Omega \frac{G_c l}{c_w}\boldsymbol{\nabla}\varphi\cdot\boldsymbol{\nabla}\delta\varphi\,\mathrm{d}\Omega = 0 \qquad \forall\, \delta\varphi \in \mathbb{P}^0$$

$$E'(\mathbf{u},\varphi,\theta;\delta\theta) = \int_\Omega -2\eta\theta\big(h(\varphi)-\theta^2\big)\delta\theta \,\mathrm{d}\Omega = 0 \qquad \forall\, \delta\theta \in \mathbb{T} \quad (2.22c)$$

using pertinent time-dependent Dirichlet boundary conditions $\mathbf{u}^p$ *on* Γ_D^u*, and Neumann boundary condition* $\mathbf{t}_p^u$ *on* Γ_N^u*. The trial and test spaces are defined as*

$$\mathbb{U} = \{\mathbf{u} \in [H^1(\Omega)]^{\dim} | \mathbf{u} = \mathbf{u}^p \ \textit{on}\ \Gamma_D^u\}, \quad (2.23a)$$
$$\mathbb{U}^0 = \{\mathbf{u} \in [H^1(\Omega)]^{\dim} | \mathbf{u} = \mathbf{0} \ \textit{on}\ \Gamma_D^u\}, \quad (2.23b)$$
$$\mathbb{P} = \{\varphi \in [H^1(\Omega)] | \varphi = \varphi^p \ \textit{on}\ \Gamma_D^\varphi\}, \quad (2.23c)$$
$$\mathbb{P}^0 = \{\varphi \in [H^1(\Omega)] | \varphi = 0 \ \textit{on}\ \Gamma_D^\varphi\}. \quad (2.23d)$$
$$\mathbb{T} = \{\theta \in [L^2(\Omega)]\}. \quad (2.23e)$$

■

2.6 Discussion

Two novel methods are proposed in this thesis for computational treatment of fracture irreversibility, the micromorphic approach and the slack variable method. The micromorphic approach to phase-field fracture (see Section 2.4) enables a simpler treatment of the fracture irreversibility as well as the enforcement of the upper and lower bounds, through max and min operations, since the phase-field variable is local. For AT1 and AT2 brittle fracture models, explicit expressions for the phase-field exist (see Equations (2.14) and (2.15)), since (2.11) is linear. However, for quasi-brittle fracture, multiple solutions exist, as the order of (2.11) is 2 or higher. As such, the micromorphic approach to phase-field fracture is more suited to brittle fracture than for quasi-brittle fracture. For this reason, in Paper A, the numerical experiments are carried out on AT2 brittle fracture benchmark problems.

Another aspect associated with the micromorphic approach to phase-field fracture concerns the choice of the additional parameter α, and its effect on the the global response (e.g., load-displacement curves) and the fracture length-scale. To this end, the parametrisation $\alpha = \beta G_c/l$ is adopted and a parametric study is carried out with several β values. It is observed that an optimal value of β exists, corresponding to the least micromorphic energy to fracture energy

ratio. As this ratio becomes lower, the micromorphic model converges towards the original phase-field model. The numerical experiments on the benchmark problems, carried out in Paper A also indicate that the optimal β yield load-displacement curves closer to those found in the literature. Furthermore, for the β values in the vicinity of its optimum, the fracture length-scale also remains similar to that observed for the original phase-field model for fracture. This observation is in contrast with [89] where the fracture length-scale is reported as $l/\sqrt{\beta}$. Backed by the numerical experiments conducted in Paper A, it is postulated that $l/\sqrt{\beta}$ is not the fracture length-scale of the micromorphic model. Also, in Paper A, it is postulated that α could be treated either for regularisation purpose or as a material parameter. In the former case, α is chosen such that it results in a behaviour similar (in terms of fracture length-scale and global response) to that from the original phase-field model for fracture. In the latter case, α needs to the calibrated from experimental data. In that case, the micromorphic phase-field fracture model must be treated as a separate fracture model with its own set of parameters.

The slack variable based approach to fracture irreversibility (see Section 2.5) enables the transformation of the variational inequality Problem 2 into a variational equality problem using the Method of Multipliers and the Penalisation method (see Problem 5 and 6). Unlike the micromorphic approach, the phase-field variable remains non-local with regularity requirements w.r.t its derivative. Furthermore, in an investigation carried out in Paper B, it is observed that tangent terms corresponding to the slack variable Euler-Lagrange equation may be close to zero, rendering the global stiffness matrix (Jacobian) singular. Such a situation occurs only during the first iteration of each step, and a dummy stiffness is added to circumvent the problem. Also, the computational expense of the slack variable based methods are higher than the micromorphic approach or the history variable based monolithic or staggered solvers. In this context, the Penalisation method requires an additional Degree Of Freedom (DOF), while the Method of Multipliers required two additional DOFs per node in the computational mesh. However, the slack variable method is applicable to any phase-field fracture model in a straight-forward fashion.

A concise comparison of the solution techniques developed in this thesis with the history-variable based approach [61] is presented in Table 2.4.

Features	Micromorphic Approach	Slack Variable Method of Multipliers	Slack Variable Penalisation	History Variable Staggered
Additional DOFs	0	2	1	0
Fracture Irreversibility	Local	Non-local	Non-local	Local
Variational Consistency	Yes	Yes	Yes	No
Additional Parameter	Penalty	None	Penalty	None
Brittle Fracture	Applicable	Applicable	Applicable	Applicable
Quasi-brittle Fracture	Multiple local solutions	Applicable	Applicable	Applicable

Table 2.4: A comparison of solution techniques used in this thesis.

CHAPTER 3

Multi-scale fracture modelling

This chapter deals with multi-scale fracture modelling in the context of the phase-field model for fracture. To this end, the reader is first introduced to the Variationally Consistent Homogenisation (VCH) technique. Thereafter, an overview of the multi-scale phase-field fracture framework developed in Paper C [72] is presented. The chapter concludes with a discussion on the framework.

3.1 Variationally Consistent Homogenisation

The Variationally Consistent Homogenisation (VCH) technique [90] is one of the methods used to derive the macro-scale and sub-scale (RVE) problems from a *fine-scale*[1] problem. The essential ingredients of the VCH technique are (A) the separation of scales via the Variational Multi-Scale (VMS) method [91, 92], (B) the computational homogenisation approach, (C) prolongation of solution fields using Taylor series expansion, and (D) establishing the macro-homogeneity conditions.

[1] A *fine-scale* problem is fully resolved w.r.t. all physics across several scales, and requires computationally expensive direct numerical simulation.

(A) Variational Multi-scale Method

Let $\Omega \in \mathbb{R}^{dim}$ ($dim \geq 1$) be a smooth, open bounded domain with smooth boundary Γ. For appropriately defined H^1 Sobolev trial and test spaces, a continuum equilibrium problem assumes the form,

$$\int_{\Omega} \boldsymbol{\sigma}(\mathbf{u}) \colon \boldsymbol{\epsilon}(\delta\mathbf{u}) \, \mathrm{d}\Omega = 0 \quad \forall \, \delta\mathbf{u} \in \mathbb{U}^0, \tag{3.1}$$

in the absence of body forces, and $\boldsymbol{\sigma}$, $\boldsymbol{\epsilon}$ and $\mathbf{u}$ are the stress, strain and displacement respectively. Assuming the above problem belongs to the multi-scale category, the Variational Multi-Scale (VMS) method allows a sum decomposition of the displacement (solution) field $\mathbf{u}$ into a smooth macro-scale component $\mathbf{u}^M$ and rapidly fluctuating part $\mathbf{u}^S$. Adopting a similar decomposition for the test function $\delta\mathbf{u}$, (3.1) can be decoupled as,

$$\int_{\Omega} \boldsymbol{\sigma}[\mathbf{u}^M + \mathbf{u}^S] \colon \boldsymbol{\epsilon}[\delta\mathbf{u}^M] \, \mathrm{d}\Omega = 0, \tag{3.2a}$$

$$\int_{\Omega} \boldsymbol{\sigma}[\mathbf{u}^M + \mathbf{u}^S] \colon \boldsymbol{\epsilon}[\delta\mathbf{u}^S] \, \mathrm{d}\Omega = 0, \tag{3.2b}$$

for appropriately defined trial and test spaces for the macro-scale and sub-scale problem. In the absence of further assumptions, Equations (3.2a) and (3.2b) must be solved for the entire computational domain Ω. However, based on suitable assumptions, the sub-scale problem (3.2b) could be formulated as a series of independent problems on patches within Ω. The patches could be of any size, encompassing either a single element or multiple elements, or associated with only a single integration point. All of these approaches lie within the broader category of domain decomposition methods, suitable only for multi-scale problems with moderate difference in the length scales. Furthermore, domain decomposition methods are not the focus of this thesis. As such, the reader is referred to [93–97] for more on the topic.

Without venturing into the details of the domain decomposition method, it can be assessed that a large difference in the length scales of a multi-scale problem would lead to a prohibitively huge computational resource demand. The reason for this is the extremely fine meshes required for resolving small length scales in the sub-scale domain. In such a scenario, the computational homogenisation approach [98–101] is a computationally viable alternative, as

it only requires the sub-scale domain to contain enough statistical information about the heterogeneities in the underlying microstructure, and is independent of the macro-scale discretisation. For this reason, the sub-domain is also referred to as the Representative Volume Element (RVE) or Statistical Volume Element (SVE). At this point, the reader is referred to [102, 103] for more details on the choice of RVE/SVE for random media. The use of the computational homogenisation approach in conjunction with the VMS method lends the name Variationally Consistent Homogenisation (VCH) technique, and separates the latter from domain decomposition methods.

(B) Computational Homogenisation

In the context of partial differential equations, homogenisation refers to the process of replacing a spatially rapidly varying coefficient with an uniform (effective) one. The effective coefficient is computed as an average over a certain spatial domain. In the context of a multi-scale problem, the averaging takes place over the RVE domain, denoted as $\Omega_\square$, here onwards. To put it in a mathematical perspective, consider an integral expression over a macro-scale domain,

$$\int_\Omega f(\mathbf{x})\,\mathrm{d}\Omega, \tag{3.3}$$

for an arbitrary rapidly oscillating function $f(\mathbf{x})$. Assuming that an RVE exist for all $\mathbf{x} \in \Omega$, the integrand $f(\mathbf{x})$ in the above expression is approximated as,

$$f(\mathbf{x}) \approx \overline{f} := \frac{1}{|\Omega_\square|}\int_{\Omega_\square} f\,\mathrm{d}\Omega, \tag{3.4}$$

with $\Omega_\square$ centered at $\bar{\mathbf{x}}$. However, in the context of the finite element method, integral expressions such as (3.3) are evaluated through numerical integration. As such, finite number of RVEs is required, each RVE associated with a macroscopic integration point.

The VCH approach replaces every integrand in the macro-scale (3.2a) and RVE-scale (3.2b) equation with an approximation of the form (3.4). For large expressions, the notation $\langle f\rangle_\square = \overline{f}$ is introduced, and will be used throughout

the thesis. This results in,

$$\int_{\Omega} \langle \boldsymbol{\sigma}[\mathbf{u}^M + \mathbf{u}^S] \colon \boldsymbol{\epsilon}[\delta \mathbf{u}^M] \rangle_{\square} \, \mathrm{d}\Omega = 0, \tag{3.5a}$$

$$\int_{\Omega} \langle \boldsymbol{\sigma}[\mathbf{u}^M + \mathbf{u}^S] \colon \boldsymbol{\epsilon}[\delta \mathbf{u}^S] \rangle_{\square} \, \mathrm{d}\Omega = 0. \tag{3.5b}$$

Although the macro-scale problem (3.5a) must be solved over the macro-scale domain Ω, the RVE equation (3.5*b*) is a set of independent problems of the form,

$$\langle \boldsymbol{\sigma}[\mathbf{u}^M + \mathbf{u}^S] \colon \boldsymbol{\epsilon}[\delta \mathbf{u}^S] \rangle_{\square} = 0, \tag{3.6}$$

since every RVE is local to a macro-scale integration point.

(C) Prolongation and first-order homogenisation

The VCH approach assumes the existence of a smooth displacement (solution) field $\bar{\mathbf{u}}$ on the macro-scale, as shown in Figure 3.1 (left). The smooth solution field $\bar{\mathbf{u}}$ contributes $\mathbf{u}^M$ (indicated by the red line in right sub-figure) towards the RVE solution field, $\mathbf{u}$. This operation is termed as prolongation. In this thesis, only first-order homogenisation is considered. Consequently, $\mathbf{u}^M$ is obtained through a Taylor series expansion of $\bar{\mathbf{u}}$ about $\bar{\mathbf{x}}$, until the first-order derivative term. This results,

$$\mathbf{u}^M(\bar{\mathbf{u}}, \bar{\mathbf{x}}, \mathbf{x}) = \bar{\mathbf{u}} + \boldsymbol{\nabla}^{\mathrm{sym}} \bar{\mathbf{u}}\big|_{\bar{\mathbf{x}}} \cdot [\mathbf{x} - \bar{\mathbf{x}}]. \tag{3.7}$$

with $\mathbf{u}^M$ varying linearly within the RVE domain $\Omega_{\square}$.
Adopting the notation $\boldsymbol{\epsilon}[\bar{\mathbf{u}}(\bar{\mathbf{x}})] = \boldsymbol{\nabla} \bar{\mathbf{u}}\big|_{\bar{\mathbf{x}}}$, the consequences of (3.7) are,

$$\bar{\mathbf{u}}(\bar{\mathbf{x}}) = \langle \mathbf{u}^M(\bar{\mathbf{u}}, \bar{\mathbf{x}}, \mathbf{x}) \rangle_{\square}, \tag{3.8a}$$

$$\boldsymbol{\epsilon}[\bar{\mathbf{u}}(\bar{\mathbf{x}})] = \langle \boldsymbol{\epsilon}[\mathbf{u}^M(\bar{\mathbf{u}}, \bar{\mathbf{x}}, \mathbf{x})] \rangle_{\square}. \tag{3.8b}$$

Therefore, the macro-scale problem (3.5a) is equivalent to,

$$\int_{\Omega} \bar{\boldsymbol{\sigma}} \colon \boldsymbol{\epsilon}[\delta \bar{\mathbf{u}}] \, \mathrm{d}\Omega = 0, \tag{3.9}$$

where, the effective stress given by,

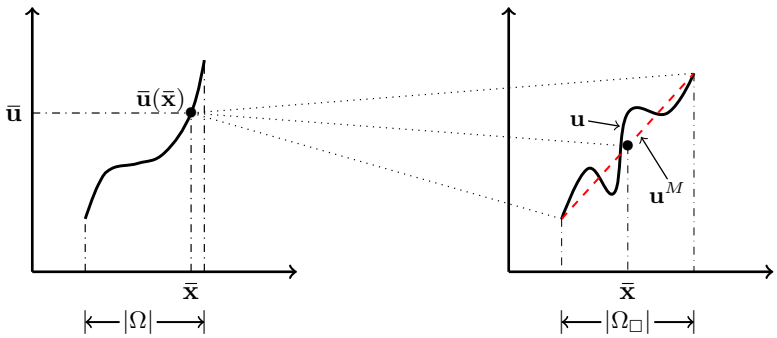

Figure 3.1: Figures showing the smooth solution field $\bar{\mathbf{u}}$ on the macro-scale domain Ω (left), and the rapidly oscillating solution field $\mathbf{u}$ on the RVE domain $\Omega_\square$ (right). The linear macro-scale contribution $\mathbf{u}^M$ from $\bar{\mathbf{u}}$ is denoted by the dashed red line in the right sub-figure.

$$\bar{\boldsymbol{\sigma}} = \langle \boldsymbol{\sigma} \rangle_\square. \tag{3.10}$$

Following the computation of $\bar{\mathbf{u}}$ using the above equation, augmented with appropriate test and trial spaces, $\mathbf{u}^M$ is obtained from (3.7). Thereafter, the RVE problems are driven by $\mathbf{u}^M$, as observed from (3.6). However, constraints must be enforced on the oscillating RVE solution field, $\mathbf{u}^S$ in order to guarantee solvability of the RVE problem. This step is carried out using the (Hill-Mandel) macro-homogeneity conditions [104–106].

(D) Macro-homogeneity condition

The macro-homogeneity condition establishes the equivalence of the virtual work between the macro-scale integration point and the RVE domain. To that end, first, a strain identity,

$$\boldsymbol{\epsilon}[\bar{\mathbf{u}}] = \langle \boldsymbol{\epsilon}[\mathbf{u}] \rangle_\square \tag{3.11}$$

is assumed to hold. Using (3.8b), the necessary condition satisfying the above equation is $\langle \boldsymbol{\epsilon}[\mathbf{u}^S] \rangle_\square = 0$. This is achieved through Dirichlet, Neumann, and Strongly Periodic boundary conditions on the RVE problem (commonly adopted in the computational homogenisation literature). Recalling the stress

identity (3.10), and on using the aforementioned boundary conditions, the virtual work identity or the macro-homogeneity condition,

$$\bar{\boldsymbol{\sigma}} : \boldsymbol{\epsilon}[\bar{\mathbf{u}}] = \langle \boldsymbol{\sigma} : \boldsymbol{\epsilon}[\mathbf{u}] \rangle_{\square}, \tag{3.12}$$

is fulfilled. The above expression is the classical form of the macro-homogeneity condition, popular in the computational homogenisation literature [107]. For a generalised form of the macro-homogeneity condition, the reader is referred to [90].

3.2 Multi-scale phase-field fracture framework

The multi-scale phase-field fracture framework is developed in Paper C using the VCH approach, in a similar way to the continuum problem in Section 3.1. The steps (A)-(D) are followed for the momentum balance equation and the phase-field evolution equation. These equations are taken from Problem 3 in Chapter 2. Furthermore, the presented multi-scale framework is developed only for AT2 brittle fracture, a choice motivated by the ease in the numerical implementation. The degradation function and the local fracture energy dissipation function are chosen accordingly (see Tables 2.1 and 2.2). The extension towards the AT1 brittle fracture as well as the PFCZM quasi-brittle fracture is deemed straight-forward.

The derivation of the multi-scale problem is presented in detail in Paper C. As such, a brief summary is provided, with the equations/problem statements being referred from the aforementioned manuscript. The starting point in the VCH approach is the set of Euler-Lagrange equations corresponding to the fully resolved problem. In this thesis, the equations for the AT2 brittle model serves as the fully resolved problem (see Problem Statement 3 in Paper C). Thereafter, analogous to step (A) in Section 3.1, an additive decomposition is introduced for the displacement field and the phase-field, and their respective test functions. Also, the integrands in the momentum balance equation and phase-field evolution equation are replaced by their homogenised counterparts (B). Finally, the prolongation operation (C) is introduced for the displacement, phase-field and their respective test functions. This operation is analogous to the prolongation for the displacement field, shown in Figure 3.1 and given by (3.7). In Paper C, step (B) is presented in Section 3.1, whereas the steps (A) and (C) are in Section 3.2. This leads to the definition of the macro-

scale problem for AT2 brittle fracture, shown in Problem Statement 4 in the aforementioned manuscript.

Furthermore, the steps (A) and (B) also results in an RVE problem, similar to (3.6). However, in Paper C, the RVE problem is augmented with constraints (boundary conditions) that fulfil the macro-homogeneity conditions (D). In this context, four different RVE problems are defined (Problem Statements 5-8), pertaining to Weakly Periodic Boundary Condition (WPBC), Strongly Periodic Boundary Condition (SPBC), Neumann Boundary Condition (NBC), and Dirichlet Boundary Condition (DBC). The WPBC requires special treatment during implementation in terms of generating an optimal mesh for the Lagrange multipliers. As such, RVE studies with WPBC is avoided in the manuscript. Nevertheless, the RVE WPBC problem (Problem Statement 5) is regarded as a general problem, since the other boundary conditions can be derived from it, upon making certain choices in the test and trial function spaces.

The multi-scale phase-field fracture framework is then expanded in terms of the different homogenisation measures that can be pursued. This is possible as the VCH approach does not impose any restrictions on the homogenisation measures that replaces an integrand of the Euler-Lagrange equations (Step (B) in Section 3.1). Therefore, a certain integrand may be evaluated using an RVE surface-averaging measure instead of a volume-average. The RVE surface-averaging measure is explored in this thesis (Paper C) in the context of the smooth phase-field on the macro-scale, and it leads to an alternative multi-scale phase-field fracture model within the multi-scale framework.

Yet another multi-scale fracture model is developed using the concept of selective homogenisation. Selective homogenisation allows a certain solution field to live only on the RVE domain. In that case, the macroscopic counterpart of the solution field and its corresponding test function would cease to exist. In Section 3.6 of Paper C, the selective homogenisation is applied only to the phase-field. Mathematically, it means that the RVE phase-field $\varphi = \varphi^S$ and $\delta\varphi = \delta\varphi^S$. Consequently, it eliminates the macro-scale phase-field evolution equation.

3.3 Discussion

A novel multi-scale phase-field fracture framework is proposed in this thesis, that allows for different homogenisation choices within a variationally consistent scheme. Assuming the existence of the smooth solution fields $(\overline{\mathbf{u}}, \overline{\varphi})$ leads to a coupled momentum balance and phase evolution equation both at the macro-scale as well as on the RVE-level. It is important to note that $\overline{\varphi}$ is the volume-average of φ in the RVE. Consequently, its value is not indicative of failure/crack. This has been demonstrated in Paper C, with the help of a multi-scale FE^2 problem in Section 5. In this problem, although a certain RVE has lost integrity, $\overline{\varphi} \approx 0.1415$. Thus, the loss of integrity at a macro-scale integration point is assessed by the stress, whereas $\overline{\varphi}$ is treated as an auxiliary solution field. Nevertheless, the presence of $\overline{\varphi}$ leads to the existence of a macro-scale phase-field evolution equation, eventually resulting in a non-local effect on the macro-scale. This can be observed from Figure 15(b) in Paper C.

Alternatively, the 'selective homogenisation-based' multi-scale phase-field model that assumes the phase-field to live only on the RVE level is computationally cheaper. This is because it eliminates the need to solve a phase-field evolution equation on the macro-scale (fewer DOFs). However, the macro-scale behaviour is local as observed from Figure 15(a) in the Paper C. Similar behaviour is observed for softening type dissipative material laws [108]. Therefore, the RVE response can be thought of as similar to a local continuum damage model.

CHAPTER 4

Summary of included papers

This chapter provides the summary of the included papers.

4.1 Paper A

Ritukesh Bharali, Fredrik Larsson, Ralf Jänicke
A micromorphic phase-field model for fracture
Manuscript to be submitted for publication .

In this manuscript, a novel phase-field model for fracture is proposed, based on the micromorphic extension of the energy functional. This approach transforms the phase-field solution field into a local variable, while introducing a micromorphic variable that regularises the fracture problem. The pertinent Euler-Lagrange equations are presented along with an explicit expression for updating the local phase-field variable for the AT2 brittle fracture model. Thereafter, numerical experiments are carried out on benchmark problems (single edge notched specimen under tension and shear, three-point bending, and notched concrete specimen with hole) to investigate the effect of the penalty term on the global response (load-displacement curves) and the frac-

ture length-scale. Through a parametric study, it is shown that an optimal value of the penalty parameter exists for which the global response as well as the fracture length-scale of the micromorphic model is similar to that of the original model.

4.2 Paper B

Ritukesh Bharali, Fredrik Larsson, Ralf Jänicke
Phase-field fracture irreversibility using the slack variable approach
Manuscript to be submitted for publication .

In this manuscript, the phase-field fracture irreversibility constraint is transformed into an equality-based constraint using the slack variable approach. The equality-based fracture irreversibility constraint is then introduced in the phase-field fracture energy functional using the Method of Multipliers and the Penalisation method. Both methods are variationally consistent with conventional variational inequality phase-field fracture problem, unlike the history-variable approach. A simple analytical proof is presented for the former. Thereafter, numerical experiments are carried out on benchmark problems (single edge notched specimen under tension and shear, three-point bending and notched concrete specimen with a hole) to demonstrate the behaviour of the proposed methods.

4.3 Paper C

Ritukesh Bharali, Fredrik Larsson, Ralf Jänicke
Computational homogenisation of phase-field fracture
Published in European Journal of Mechanics - A/Solids,
vol. 88, July–August 2021.
DOI: `10.1016/j.euromechsol.2021.104247` .

In this manuscript, the computational homogenisation of phase-field fractures is addressed. To this end, a variationally consistent two-scale phase-field fracture framework is developed, which formulates the coupled momentum balance and phase-field evolution equations at the macro-scale as well as at the Representative Volume Element (RVE) scale. The phase-field variable represent fractures at the RVE scale, however, at the macro-scale, it

is treated as an auxiliary variable. The latter interpretation follows from the homogenisation of the phase-field through volume or a surface-average. For either homogenisation choices, the set of macro-scale and sub-scale equations, and the pertinent macro-homogeneity satisfying boundary conditions are established. As a special case, the concept of selective homogenisation is introduced, where the phase-field is chosen to live only in the RVE domain, thereby eliminating the macro-scale phase-field evolution equation. Numerical experiments demonstrate the local macro-scale material behaviour of the selective homogenisation based two-scale phase-field fracture model, while its non-selective counterpart yields a non-local macro-scale material behaviour.

CHAPTER 5

Concluding Remarks and Future Work

The contribution of this thesis can be broadly categorised into the development of solution strategies and multi-scale techniques for phase-field fracture problems. In the context of the former category, emphasis is laid on the treatment of fracture irreversibility. To this end, two solution strategies are proposed, the micromorphic phase-field fracture model and the slack variable method.

The micromorphic phase-field fracture model transforms the phase-field variable into a local quantity, while introducing a new micromorphic variable that regularises the fracture problem. As elucidated in Section 2.4, both AT1 and AT2 brittle fracture models can be implemented with ease, owing to a closed form expression for the local phase-field variable. However, extension towards the PFCZM quasi-brittle model maybe challenging due to the existence of multiple solutions for the local phase-field variable. However, in the context, it is important to note that multiple local solutions are easier to treat compared to multiple global solutions in a computational framework. Alternatively, quasi-brittle fracture models can be developed within the AT1 and AT2 model framework by considering a gradual release of the fracture energy, i.e., $G_c = G_c(\llbracket u \rrbracket, \kappa)$. Here, $\llbracket u \rrbracket$ and κ represent the displacement jump and

an internal variable respectively. However, the computation of the displacement jump from a smeared representation of fracture is non-trivial [55], and may require special tracking techniques [37, 109]. Nevertheless, the extension of the current micromorphic model towards quasi-brittle fracture presents an interesting future avenue.

The slack variable approach replaces the fracture irreversibility inequality constraint, $h(\varphi) \geq 0$ with an equivalent equality constraint, $h(\varphi)+\theta^2 = 0$. The latter constraint is then added to the phase-field fracture energy functional using the Method of Multipliers and the Penalisation method. Both methods are variationally consistent with the original phase-field fracture model (Problem 1 in Chapter 2), and are applicable to any phase-field fracture model. However, in Paper B, the numerical experiments are limited to AT2 brittle fracture. In the future, extension of the current work may be oriented towards quasi-brittle fractures, multiphysics applications (fracture in porous media, corrosion, etc.) and/or the further development of the method itself (for instance, preconditioning for large problems).

The second category of work performed in this thesis is the development of a multi-scale phase-field fracture framework in Paper C. Assuming the existence of an AT2 brittle fracture fully resolved model, pertinent macro-scale and RVE-scale problems were derived using the Variationally Consistent Homogenisation (VCH) technique. Several homogenisation choices were explored in the context of the phase-field variable. A volume-average based definition of the macro-scale phase-field resulted in a non-local behaviour on the macro-scale, while assuming the phase-field to live only on the RVE domain led to a local macro-scale response. Furthermore, in the context of the RVE problem, different macro-homogeneity compliant boundary conditions are explored. It is observed that Dirichlet boundary condition resulted in an artificially stiff response, since the crack could not penetrate the boundary. The Neumann boundary condition led to widening of the existing cracks on the boundary, as such it is considered unrealistic. The strongly periodic boundary condition circumvented the aforementioned issues, however, at the cost of a periodicity bias of the fracture topology.

Future studies may be directed at eliminating the RVE fracture periodicity bias. In this regard, the weak format of periodicity [110–112] offers a good starting point. Furthermore, in this thesis, the RVEs were assumed to be representative during the hardening and softening regimes of the underlying

microstructure. The existence of an RVE in the softening regime has been questioned in [103], where it is shown that upon localisation, the RVE is no longer statistically representative of the microstructure. Studies aimed at alleviating this issue include homogenisation schemes over the localised zone [113, 114]. A similar route can be followed for a multi-scale phase-field fracture model. Finally, the multi-scale phase-field fracture framework can be generalised further to include all possible phase-field fracture models.

References

[1] Hideo Kobayashi and Hisahiro Onoue. “Brittle fracture of liberty ships”. In: *Failure Knowledge Database* 100 (1943), p. 67.

[2] Anil K Chopra and P Chakrabarti. “The Koyna earthquake and the damage to Koyna dam”. In: *Bulletin of the Seismological Society of America* 63.2 (1973), pp. 381–397.

[3] Raghvendra Singh, Debasis Roy, and Sudhir K Jain. “Analysis of earth dams affected by the 2001 Bhuj Earthquake”. In: *Engineering geology* 80.3-4 (2005), pp. 282–291.

[4] KS Jagadish, S Raghunath, and KS Nanjunda Rao. “Behaviour of masonry structures during the Bhuj earthquake of January 2001”. In: *Journal of Earth System Science* 112.3 (2003), pp. 431–440.

[5] Katsuichiro Goda et al. “The 2015 Gorkha Nepal earthquake: insights from earthquake damage survey”. In: *Frontiers in Built Environment* 1 (2015), p. 8.

[6] M Di Ludovico et al. “Remarks on damage and response of school buildings after the Central Italy earthquake sequence”. In: *Bulletin of earthquake engineering* 17.10 (2019), pp. 5679–5700.

[7] Olgierd Cecil Zienkiewicz et al. *The finite element method*. Vol. 3. McGraw-hill London, 1977.

[8] Thomas JR Hughes. *The finite element method: linear static and dynamic finite element analysis*. Courier Corporation, 2012.

[9] D.S. Dugdale. "Yielding of steel sheets containing slits". In: *Journal of the Mechanics and Physics of Solids* 8.2 (1960), pp. 100–104. ISSN: 0022-5096. DOI: https://doi.org/10.1016/0022-5096(60)90013-2.

[10] G.I. Barenblatt. "The Mathematical Theory of Equilibrium Cracks in Brittle Fracture". In: ed. by H.L. Dryden et al. Vol. 7. Advances in Applied Mechanics. Elsevier, 1962, pp. 55–129. DOI: https://doi.org/10.1016/S0065-2156(08)70121-2.

[11] MGGV Elices et al. "The cohesive zone model: advantages, limitations and challenges". In: *Engineering fracture mechanics* 69.2 (2002), pp. 137–163. DOI: https://doi.org/10.1016/S0013-7944(01)00083-2.

[12] Natarajan Sukumar et al. "Extended finite element method for three-dimensional crack modelling". In: *International journal for numerical methods in engineering* 48.11 (2000), pp. 1549–1570. DOI: https://doi.org/10.1002/1097-0207(20000820)48:11<1549::AID-NME955>3.0.CO;2-A.

[13] Nicolas Moës and Ted Belytschko. "Extended finite element method for cohesive crack growth". In: *Engineering fracture mechanics* 69.7 (2002), pp. 813–833. DOI: https://doi.org/10.1016/S0013-7944(01)00128-X.

[14] Amir R Khoei. *Extended finite element method: theory and applications*. John Wiley & Sons, 2014.

[15] Christian Linder and Francisco Armero. "Finite elements with embedded strong discontinuities for the modeling of failure in solids". In: *International Journal for Numerical Methods in Engineering* 72.12 (2007), pp. 1391–1433. DOI: https://doi.org/10.1002/nme.2042.

[16] José M Sancho et al. "An embedded crack model for finite element analysis of concrete fracture". In: *Engineering fracture mechanics* 74.1-2 (2007), pp. 75–86. DOI: https://doi.org/10.1016/j.engfracmech.2006.01.015.

[17] Rene de Borst et al. "Discrete vs smeared crack models for concrete fracture: bridging the gap". In: *International journal for numerical and analytical methods in geomechanics* 28.7-8 (2004), pp. 583–607. DOI: https://doi.org/10.1002/nag.374.

[18] R. H. J. Peerlings et al. “Gradient enhanced damage for quasi-brittle materials”. In: *International Journal for Numerical Methods in Engineering* 39.19 (1996), pp. 3391–3403. DOI: https://doi.org/10.1002/(SICI)1097-0207(19961015)39:19<3391::AID-NME7>3.0.CO;2-D.

[19] M.G.D. Geers et al. “Strain-based transient-gradient damage model for failure analyses”. In: *Computer Methods in Applied Mechanics and Engineering* 160.1 (1998), pp. 133–153. ISSN: 0045-7825. DOI: https://doi.org/10.1016/S0045-7825(98)80011-X.

[20] Stewart A Silling. “Reformulation of elasticity theory for discontinuities and long-range forces”. In: *Journal of the Mechanics and Physics of Solids* 48.1 (2000), pp. 175–209. DOI: https://doi.org/10.1016/S0022-5096(99)00029-0.

[21] Stewart A Silling and Ebrahim Askari. “A meshfree method based on the peridynamic model of solid mechanics”. In: *Computers & structures* 83.17-18 (2005), pp. 1526–1535. DOI: https://doi.org/10.1016/j.compstruc.2004.11.026.

[22] Pablo Seleson et al. “Peridynamics as an upscaling of molecular dynamics”. In: *Multiscale Modeling & Simulation* 8.1 (2009), pp. 204–227.

[23] G.A. Francfort and J.-J. Marigo. “Revisiting brittle fracture as an energy minimization problem”. In: *Journal of the Mechanics and Physics of Solids* 46.8 (Aug. 1998), pp. 1319–1342. ISSN: 00225096. DOI: 10.1016/S0022-5096(98)00034-9.

[24] B. Bourdin, G.A. Francfort, and J-J. Marigo. “Numerical experiments in revisited brittle fracture”. In: *Journal of the Mechanics and Physics of Solids* 48.4 (2000), pp. 797–826. ISSN: 0022-5096. DOI: https://doi.org/10.1016/S0022-5096(99)00028-9.

[25] B. Bourdin. “Numerical implementation of the variational formulation for quasi-static brittle fracture”. In: *Interfaces and Free Boundaries* 9 (2007), pp. 411–430. DOI: 10.4171/IFB/171.

[26] David Bryant Mumford and Jayant Shah. “Optimal approximations by piecewise smooth functions and associated variational problems”. In: *Communications on pure and applied mathematics* (1989). DOI: https://doi.org/10.1002/cpa.3160420503.

[27] Christian Miehe, Fabian Welschinger, and Martina Hofacker. "Thermodynamically consistent phase-field models of fracture: Variational principles and multi-field FE implementations". In: *International journal for numerical methods in engineering* 83.10 (2010), pp. 1273–1311. DOI: https://doi.org/10.1002/nme.2861.

[28] Christian Miehe, Lisa-Marie Schänzel, and Heike Ulmer. "Phase field modeling of fracture in multi-physics problems. Part I. Balance of crack surface and failure criteria for brittle crack propagation in thermo-elastic solids". In: *Computer Methods in Applied Mechanics and Engineering* 294 (2015), pp. 449–485. ISSN: 0045-7825. DOI: https://doi.org/10.1016/j.cma.2014.11.016.

[29] M. Ambati, T. Gerasimov, and L. De Lorenzis. "Phase-field modeling of ductile fracture". In: *Computational Mechanics* 55.5 (May 2015), pp. 1017–1040. ISSN: 1432-0924. DOI: 10.1007/s00466-015-1151-4.

[30] Roberto Alessi, Jean-Jacques Marigo, and Stefano Vidoli. "Gradient damage models coupled with plasticity: Variational formulation and main properties". In: *Mechanics of Materials* 80 (2015). Materials and Interfaces, pp. 351–367. ISSN: 0167-6636. DOI: https://doi.org/10.1016/j.mechmat.2013.12.005.

[31] C. Miehe et al. "Phase field modeling of fracture in multi-physics problems. Part II. Coupled brittle-to-ductile failure criteria and crack propagation in thermo-elastic–plastic solids". In: *Computer Methods in Applied Mechanics and Engineering* 294 (2015), pp. 486–522. ISSN: 0045-7825. DOI: https://doi.org/10.1016/j.cma.2014.11.017.

[32] Christian Miehe, Fadi Aldakheel, and Arun Raina. "Phase field modeling of ductile fracture at finite strains: A variational gradient-extended plasticity-damage theory". In: *International Journal of Plasticity* 84 (2016), pp. 1–32. ISSN: 0749-6419. DOI: https://doi.org/10.1016/j.ijplas.2016.04.011.

[33] S. Teichtmeister et al. "Phase field modeling of fracture in anisotropic brittle solids". In: *International Journal of Non-Linear Mechanics* 97 (2017), pp. 1–21. ISSN: 0020-7462. DOI: https://doi.org/10.1016/j.ijnonlinmec.2017.06.018.

[34] Jeremy Bleyer and Roberto Alessi. "Phase-field modeling of anisotropic brittle fracture including several damage mechanisms". In: *Computer Methods in Applied Mechanics and Engineering* 336 (2018), pp. 213–236. ISSN: 0045-7825. DOI: https://doi.org/10.1016/j.cma.2018.03.012.

[35] Zachary A. Wilson and Chad M. Landis. "Phase-field modeling of hydraulic fracture". In: *Journal of the Mechanics and Physics of Solids* 96 (2016), pp. 264–290. ISSN: 0022-5096. DOI: https://doi.org/10.1016/j.jmps.2016.07.019.

[36] Y. Heider and B. Markert. "A phase-field modeling approach of hydraulic fracture in saturated porous media". In: *Mechanics Research Communications* 80 (2017). Multi-Physics of Solids at Fracture, pp. 38–46. ISSN: 0093-6413. DOI: https://doi.org/10.1016/j.mechrescom.2016.07.002.

[37] Chukwudi Chukwudozie, Blaise Bourdin, and Keita Yoshioka. "A variational phase-field model for hydraulic fracturing in porous media". In: *Computer Methods in Applied Mechanics and Engineering* 347 (2019), pp. 957–982. DOI: https://doi.org/10.1016/j.cma.2018.12.037.

[38] Tuanny Cajuhi, Lorenzo Sanavia, and Laura De Lorenzis. "Phase-field modeling of fracture in variably saturated porous media". In: *Computational Mechanics* 61.3 (2018), pp. 299–318. DOI: https://doi.org/10.1007/s00466-017-1459-3.

[39] Yousef Heider and WaiChing Sun. "A phase field framework for capillary-induced fracture in unsaturated porous media: Drying-induced vs. hydraulic cracking". In: *Computer Methods in Applied Mechanics and Engineering* 359 (2020), p. 112647. ISSN: 0045-7825. DOI: https://doi.org/10.1016/j.cma.2019.112647.

[40] Tianchen Hu, Johann Guilleminot, and John E. Dolbow. "A phase-field model of fracture with frictionless contact and random fracture properties: Application to thin-film fracture and soil desiccation". In: *Computer Methods in Applied Mechanics and Engineering* 368 (2020), p. 113106. ISSN: 0045-7825. DOI: https://doi.org/10.1016/j.cma.2020.113106.

[41] Emilio Martínez-Pañeda, Alireza Golahmar, and Christian F. Niordson. "A phase field formulation for hydrogen assisted cracking". In: *Computer Methods in Applied Mechanics and Engineering* 342 (2018), pp. 742–761. ISSN: 0045-7825. DOI: https://doi.org/10.1016/j.cma.2018.07.021.

[42] Philip K. Kristensen, Christian F. Niordson, and Emilio Martínez-Pañeda. "A phase field model for elastic-gradient-plastic solids undergoing hydrogen embrittlement". In: *Journal of the Mechanics and Physics of Solids* 143 (2020), p. 104093. ISSN: 0022-5096. DOI: https://doi.org/10.1016/j.jmps.2020.104093.

[43] Jian-Ying Wu. "A unified phase-field theory for the mechanics of damage and quasi-brittle failure". In: *Journal of the Mechanics and Physics of Solids* 103 (2017), pp. 72–99. DOI: https://doi.org/10.1016/j.jmps.2017.03.015.

[44] RU Patil, BK Mishra, and IV Singh. "An adaptive multiscale phase field method for brittle fracture". In: *Computer Methods in Applied Mechanics and Engineering* 329 (2018), pp. 254–288. DOI: https://doi.org/10.1016/j.cma.2017.09.021.

[45] RU Patil et al. "A new multiscale phase field method to simulate failure in composites". In: *Advances in Engineering Software* 126 (2018), pp. 9–33. DOI: https://doi.org/10.1016/j.advengsoft.2018.08.010.

[46] Lam H Nguyen and Dominik Schillinger. "The multiscale finite element method for nonlinear continuum localization problems at full fine-scale fidelity, illustrated through phase-field fracture and plasticity". In: *Journal of Computational Physics* 396 (2019), pp. 129–160. DOI: https://doi.org/10.1016/j.jcp.2019.06.058.

[47] Savvas P Triantafyllou and Emmanouil G Kakouris. "A generalized phase field multiscale finite element method for brittle fracture". In: *International Journal for Numerical Methods in Engineering* 121.9 (2020), pp. 1915–1945. DOI: https://doi.org/10.1002/nme.6293.

[48] Tymofiy Gerasimov et al. "A non-intrusive global/local approach applied to phase-field modeling of brittle fracture". In: *Advanced modeling and simulation in engineering sciences* 5.1 (2018), pp. 1–30. DOI: https://doi.org/10.1186/s40323-018-0105-8.

[49] Nima Noii et al. “An adaptive global–local approach for phase-field modeling of anisotropic brittle fracture”. In: *Computer Methods in Applied Mechanics and Engineering* 361 (2020), p. 112744. DOI: https://doi.org/10.1016/j.cma.2019.112744.

[50] Mickaël Duval et al. “Non-intrusive coupling: recent advances and scalable nonlinear domain decomposition”. In: *Archives of Computational Methods in Engineering* 23.1 (2016), pp. 17–38. DOI: https://doi.org/10.1007/s11831-014-9132-x.

[51] Francesca Fantoni et al. “A phase field approach for damage propagation in periodic microstructured materials”. In: *International Journal of Fracture* 223.1 (2020), pp. 53–76. DOI: https://doi.org/10.1007/s10704-019-00400-x.

[52] Bang He, Louis Schuler, and Pania Newell. “A numerical-homogenization based phase-field fracture modeling of linear elastic heterogeneous porous media”. In: *Computational Materials Science* 176 (2020), p. 109519. DOI: https://doi.org/10.1016/j.commatsci.2020.109519.

[53] T. Gerasimov and L. De Lorenzis. “A line search assisted monolithic approach for phase-field computing of brittle fracture”. In: *Computer Methods in Applied Mechanics and Engineering* 312 (Dec. 2016), pp. 276–303. ISSN: 00457825. DOI: 10.1016/j.cma.2015.12.017.

[54] Timo Heister, Mary F. Wheeler, and Thomas Wick. “A primal-dual active set method and predictor-corrector mesh adaptivity for computing fracture propagation using a phase-field approach”. In: *Computer Methods in Applied Mechanics and Engineering* (2015). ISSN: 00457825. DOI: 10.1016/j.cma.2015.03.009.

[55] Julien Vignollet et al. “Phase-field models for brittle and cohesive fracture”. In: *Meccanica* 49.11 (2014), pp. 2587–2601. DOI: https://doi.org/10.1007/s11012-013-9862-0.

[56] Stefan May, Julien Vignollet, and Rene De Borst. “A numerical assessment of phase-field models for brittle and cohesive fracture: Γ-convergence and stress oscillations”. In: *European Journal of Mechanics-A/Solids* 52 (2015), pp. 72–84. DOI: https://doi.org/10.1016/j.euromechsol.2015.02.002.

[57] N Singh et al. "A fracture-controlled path-following technique for phase-field modeling of brittle fracture". In: *Finite Elements in Analysis and Design* 113 (2016), pp. 14–29. DOI: https://doi.org/10.1016/j.finel.2015.12.005.

[58] Thomas Wick. "Modified Newton methods for solving fully monolithic phase-field quasi-static brittle fracture propagation". In: *Computer Methods in Applied Mechanics and Engineering* 325 (2017), pp. 577–611. ISSN: 0045-7825. DOI: https://doi.org/10.1016/j.cma.2017.07.026.

[59] Thomas Wick. "An Error-Oriented Newton/Inexact Augmented Lagrangian Approach for Fully Monolithic Phase-Field Fracture Propagation". In: *SIAM Journal on Scientific Computing* 39.4 (2017), B589–B617. ISSN: 1064-8275. DOI: 10.1137/16m1063873.

[60] Alena Kopaničáková and Rolf Krause. "A recursive multilevel trust region method with application to fully monolithic phase-field models of brittle fracture". In: *Computer Methods in Applied Mechanics and Engineering* 360 (2020), p. 112720. DOI: https://doi.org/10.1016/j.cma.2019.112720.

[61] Christian Miehe, Martina Hofacker, and Fabian Welschinger. "A phase field model for rate-independent crack propagation: Robust algorithmic implementation based on operator splits". In: *Computer Methods in Applied Mechanics and Engineering* 199.45-48 (2010), pp. 2765–2778. ISSN: 00457825. DOI: 10.1016/j.cma.2010.04.011.

[62] Tymofiy Gerasimov and Laura De Lorenzis. "On penalization in variational phase-field models of brittle fracture". In: *Computer Methods in Applied Mechanics and Engineering* 354 (2019), pp. 990–1026. DOI: https://doi.org/10.1016/j.cma.2019.05.038.

[63] Somdatta Goswami, Cosmin Anitescu, and Timon Rabczuk. "Adaptive fourth-order phase field analysis for brittle fracture". In: *Computer Methods in Applied Mechanics and Engineering* 361 (2020), p. 112808. DOI: https://doi.org/10.1016/j.cma.2019.112808.

[64] Chintan Jansari et al. "Adaptive phase field method for quasi-static brittle fracture using a recovery based error indicator and quadtree decomposition". In: *Engineering Fracture Mechanics* 220 (2019), p. 106599. DOI: https://doi.org/10.1016/j.engfracmech.2019.106599.

[65] Thomas Wick. "Goal functional evaluations for phase-field fracture using PU-based DWR mesh adaptivity". In: *Computational Mechanics* 57.6 (2016), pp. 1017–1035. DOI: https://doi.org/10.1007/s00466-016-1275-1.

[66] Markus Klinsmann et al. "An assessment of the phase field formulation for crack growth". In: *Computer Methods in Applied Mechanics and Engineering* 294 (2015), pp. 313–330. DOI: https://doi.org/10.1016/j.cma.2015.06.009.

[67] Sindhu Nagaraja et al. "Phase-field modeling of brittle fracture with multi-level hp-FEM and the finite cell method". In: *Computational mechanics* 63.6 (2019), pp. 1283–1300. DOI: https://doi.org/10.1007/s00466-018-1649-7.

[68] Somdatta Goswami, Cosmin Anitescu, and Timon Rabczuk. "Adaptive phase field analysis with dual hierarchical meshes for brittle fracture". In: *Engineering Fracture Mechanics* 218 (2019), p. 106608. DOI: https://doi.org/10.1016/j.engfracmech.2019.106608.

[69] V.G. Kouznetsova, M.G.D. Geers, and W.A.M. Brekelmans. "Multi-scale second-order computational homogenization of multi-phase materials: a nested finite element solution strategy". In: *Computer Methods in Applied Mechanics and Engineering* 193.48 (2004). Advances in Computational Plasticity, pp. 5525–5550. ISSN: 0045-7825. DOI: https://doi.org/10.1016/j.cma.2003.12.073.

[70] Ritukesh Bharali. *rbharali/openFE2: First beta release of multi- scale code*. Version v.1.0-beta. Jan. 2021. DOI: 10.5281/zenodo.4463345.

[71] COMSOL Multiphysics. "LiveLink for MATLAB User's Guide VERSION 5.5". In: *COMSOL AB Stockholm* (2019).

[72] Ritukesh Bharali, Fredrik Larsson, and Ralf Jänicke. "Computational homogenisation of phase-field fracture". In: *European Journal of Mechanics - A/Solids* 88 (2021), p. 104247. ISSN: 0997-7538. DOI: https://doi.org/10.1016/j.euromechsol.2021.104247.

[73] Kim Pham et al. "Gradient damage models and their use to approximate brittle fracture". In: *International Journal of Damage Mechanics* 20.4 (2011), pp. 618–652. DOI: https://doi.org/10.1177/1056789510386852.

[74] MGD Geers et al. "Strain-based transient-gradient damage model for failure analyses". In: *Computer methods in applied mechanics and engineering* 160.1-2 (1998), pp. 133–153. DOI: https://doi.org/10.1016/S0045-7825(98)80011-X.

[75] Eric Lorentz and V Godard. "Gradient damage models: Toward full-scale computations". In: *Computer Methods in Applied Mechanics and Engineering* 200.21-22 (2011), pp. 1927–1944. DOI: https://doi.org/10.1016/j.cma.2010.06.025.

[76] Michael J Borden et al. "A phase-field formulation for fracture in ductile materials: Finite deformation balance law derivation, plastic degradation, and stress triaxiality effects". In: *Computer Methods in Applied Mechanics and Engineering* 312 (2016), pp. 130–166. DOI: https://doi.org/10.1016/j.cma.2016.09.005.

[77] Luigi Ambrosio and Vincenzo Maria Tortorelli. "Approximation of functional depending on jumps by elliptic functional via t-convergence". In: *Communications on Pure and Applied Mathematics* 43.8 (1990), pp. 999–1036. DOI: https://doi.org/10.1002/cpa.3160430805.

[78] Laura De Lorenzis and Corrado Maurini. "Nucleation under multi-axial loading in variational phase-field models of brittle fracture". In: *International Journal of Fracture* (June 2021). ISSN: 1573-2673. DOI: 10.1007/s10704-021-00555-6.

[79] Giovanni Lancioni and Gianni Royer-Carfagni. "The variational approach to fracture mechanics. A practical application to the French Panthéon in Paris". In: *Journal of elasticity* 95.1-2 (2009), pp. 1–30. DOI: https://doi.org/10.1007/s10659-009-9189-1.

[80] Hanen Amor, Jean-Jacques Marigo, and Corrado Maurini. "Regularized formulation of the variational brittle fracture with unilateral contact: Numerical experiments". In: *Journal of the Mechanics and Physics of Solids* 57.8 (2009), pp. 1209–1229. DOI: https://doi.org/10.1016/j.jmps.2009.04.011.

[81] Tianyi Li. "Gradient-Damage Modeling of Dynamic Brittle F racture: Variational Principles and Numerical Simulations". PhD thesis. Université Paris-Saclay, Oct. 2016.

[82] Susanne C Brenner, L Ridgway Scott, and L Ridgway Scott. *The mathematical theory of finite element methods*. Vol. 3. Springer, 2008.

[83] Siobhan Burke, Christoph Ortner, and Endre Süli. "An adaptive finite element approximation of a variational model of brittle fracture". In: *SIAM Journal on Numerical Analysis* 48.3 (2010), pp. 980–1012.

[84] J. Wambacq et al. "Interior-point methods for the phase-field approach to brittle and ductile fracture". In: *Computer Methods in Applied Mechanics and Engineering* 375 (2021), p. 113612. ISSN: 0045-7825. DOI: https://doi.org/10.1016/j.cma.2020.113612.

[85] Samuel Forest. "Micromorphic approach for gradient elasticity, viscoplasticity, and damage". In: *Journal of Engineering Mechanics* 135.3 (2009), pp. 117–131. DOI: https://doi.org/10.1061/(ASCE)0733-9399(2009)135:3(117).

[86] FA Valentine. "The problem of Lagrange with differentiable inequality as added side conditions. 407–448". In: *Contributions to the Calculus of Variations* 37 (1933).

[87] D P Bertsekas. "Nonlinear Programming". In: *Journal of the Operational Research Society* 48.3 (1997), pp. 334–334. DOI: 10.1057/palgrave.jors.2600425.

[88] R. A. Tapia. "A stable approach to Newton's method for general mathematical programming problems inRn". In: *Journal of Optimization Theory and Applications* 14.5 (Nov. 1974), pp. 453–476. ISSN: 1573-2878. DOI: 10.1007/BF00932842.

[89] C Miehe, S Teichtmeister, and F Aldakheel. "Phase-field modelling of ductile fracture: a variational gradient-extended plasticity-damage theory and its micromorphic regularization". In: *Philosophical Transactions of the Royal Society A: Mathematical, Physical and Engineering Sciences* 374.2066 (2016), p. 20150170. DOI: https://doi.org/10.1098/rsta.2015.0170.

[90] Fredrik Larsson, Kenneth Runesson, and Fang Su. "Variationally consistent computational homogenization of transient heat flow". In: *International Journal for Numerical Methods in Engineering* 81.13 (2010), pp. 1659–1686. DOI: https://doi.org/10.1002/nme.2747.

[91] Thomas J.R. Hughes. "Multiscale phenomena: Green's functions, the Dirichlet-to-Neumann formulation, subgrid scale models, bubbles and the origins of stabilized methods". In: *Computer Methods in Applied Mechanics and Engineering* 127.1 (1995), pp. 387–401. ISSN: 0045-7825. DOI: https://doi.org/10.1016/0045-7825(95)00844-9.

[92] Thomas J.R. Hughes et al. "The variational multiscale method—a paradigm for computational mechanics". In: *Computer Methods in Applied Mechanics and Engineering* 166.1 (1998). Advances in Stabilized Methods in Computational Mechanics, pp. 3–24. ISSN: 0045-7825. DOI: https://doi.org/10.1016/S0045-7825(98)00079-6.

[93] P-A Guidault and Ted Belytschko. "On the L2 and the H1 couplings for an overlapping domain decomposition method using Lagrange multipliers". In: *International journal for numerical methods in engineering* 70.3 (2007), pp. 322–350. DOI: https://doi.org/10.1002/nme.1882.

[94] Andrea Hund and Ekkehard Ramm. "Locality constraints within multiscale model for non-linear material behaviour". In: *International journal for numerical methods in engineering* 70.13 (2007), pp. 1613–1632. DOI: https://doi.org/10.1002/nme.1953.

[95] Stefan Eckardt and Carsten Könke. "Adaptive damage simulation of concrete using heterogeneous multiscale models". In: *Journal of Algorithms & Computational Technology* 2.2 (2008), pp. 275–298. DOI: https://doi.org/10.1260/174830108784646661.

[96] Thomas Hettich, Andrea Hund, and Ekkehard Ramm. "Modeling of failure in composites by X-FEM and level sets within a multiscale framework". In: *Computer Methods in Applied Mechanics and Engineering* 197.5 (2008), pp. 414–424. DOI: https://doi.org/10.1016/j.cma.2007.07.017.

[97] J Mergheim. "A variational multiscale method to model crack propagation at finite strains". In: *International journal for numerical methods in engineering* 80.3 (2009), pp. 269–289. DOI: https://doi.org/10.1002/nme.2602.

[98] PM Suquet. "Local and global aspects in the mathematical theory of plasticity". In: *Plasticity today* (1985), pp. 279–309.

[99] JoséMiranda Guedes and Noboru Kikuchi. "Preprocessing and post-processing for materials based on the homogenization method with adaptive finite element methods". In: *Computer methods in applied mechanics and engineering* 83.2 (1990), pp. 143–198. DOI: https://doi.org/10.1016/0045-7825(90)90148-F.

[100] Kenjiro Terada and Noboru Kikuchi. "Nonlinear homogenization method for practical applications". In: *American Society of Mechanical Engineers, Applied Mechanics Division, AMD* 212 (1995), pp. 1–16.

[101] Frédéric Feyel and Jean-Louis Chaboche. "FE2 multiscale approach for modelling the elastoviscoplastic behaviour of long fibre SiC/Ti composite materials". In: *Computer methods in applied mechanics and engineering* 183.3-4 (2000), pp. 309–330. DOI: https://doi.org/10.1016/S0045-7825(99)00224-8.

[102] Martin Ostoja-Starzewski. "Material spatial randomness: From statistical to representative volume element". In: *Probabilistic engineering mechanics* 21.2 (2006), pp. 112–132. DOI: https://doi.org/10.1016/j.probengmech.2005.07.007.

[103] IM Gitman, Harm Askes, and LJ Sluys. "Representative volume: Existence and size determination". In: *Engineering fracture mechanics* 74.16 (2007), pp. 2518–2534. DOI: https://doi.org/10.1016/j.engfracmech.2006.12.021.

[104] Rodney Hill. "Elastic properties of reinforced solids: some theoretical principles". In: *Journal of the Mechanics and Physics of Solids* 11.5 (1963), pp. 357–372.

[105] R Hill. "On macroscopic effects of heterogeneity in elastoplastic media at finite strain". In: *Mathematical proceedings of the Cambridge philosophical society*. Vol. 95. 3. Cambridge University Press. 1984, pp. 481–494.

[106] Sia Nemat-Nasser. "Averaging theorems in finite deformation plasticity". In: *Mechanics of Materials* 31.8 (1999), pp. 493–523.

[107] Tarek I Zohdi and Peter Wriggers. *An introduction to computational micromechanics*. Springer Science & Business Media, 2008.

[108] R De Borst et al. "Fundamental issues in finite element analyses of localization of deformation". In: *Engineering computations* (1993).

[109] Sanghyun Lee, Mary F Wheeler, and Thomas Wick. "Iterative coupling of flow, geomechanics and adaptive phase-field fracture including level-set crack width approaches". In: *Journal of Computational and Applied Mathematics* 314 (2017), pp. 40–60. DOI: https://doi.org/10.1016/j.cam.2016.10.022.

[110] Fredrik Larsson et al. "Computational homogenization based on a weak format of micro-periodicity for RVE-problems". In: *Computer Methods in Applied Mechanics and Engineering* 200.1-4 (2011), pp. 11–26. DOI: https://doi.org/10.1016/j.cma.2010.06.023.

[111] Erik Svenning, Martin Fagerström, and Fredrik Larsson. "Computational homogenization of microfractured continua using weakly periodic boundary conditions". In: *Computer Methods in Applied Mechanics and Engineering* 299 (2016), pp. 1–21. DOI: https://doi.org/10.1016/j.cma.2015.10.014.

[112] Ritukesh Bharali, Fredrik Larsson, and Ralf Jänicke. "Computational aspects of the weak micro-periodicity saddle point problem". In: *PAMM* 20.1 (2021), e202000259. DOI: 10.1002/pamm.202000259.

[113] Vinh Phu Nguyen et al. "On the existence of representative volumes for softening quasi-brittle materials–a failure zone averaging scheme". In: *Computer Methods in Applied Mechanics and Engineering* 199.45-48 (2010), pp. 3028–3038. DOI: https://doi.org/10.1016/j.cma.2010.06.018.

[114] Clemens V Verhoosel et al. "Computational homogenization for adhesive and cohesive failure in quasi-brittle solids". In: *International Journal for Numerical Methods in Engineering* 83.8-9 (2010), pp. 1155–1179. DOI: https://doi.org/10.1002/nme.2854.

Part II

Papers

PAPER A

A micromorphic phase-field model for fracture

Ritukesh Bharali, Fredrik Larsson, Ralf Jänicke

Manuscript to be submitted for publication

A MICROMORPHIC PHASE-FIELD MODEL FOR FRACTURE

A PREPRINT

Ritukesh Bharali
Department of Industrial and Materials Science
Chalmers University of Technology
Gothenburg, 412 56, Sweden
ritukesh.bharali@chalmers.se

Fredrik Larsson
Department of Industrial and Materials Science
Chalmers University of Technology
Gothenburg, 412 56, Sweden
fredrik.larsson@chalmers.se

Ralf Jänicke
Institute of Applied Mechanics
Technische Universität Braunschweig
Braunschweig, 38106, Germany
r.janicke@tu-braunschweig.de

September 5, 2021

ABSTRACT

In this manuscript, a novel phase-field model for fracture is proposed, based on the micromorphic extension of the energy functional. This approach transforms the phase-field solution field into a local variable, while introducing a micromorphic variable that regularises the fracture problem. The pertinent Euler-Lagrange equations are presented along with an explicit expression for updating the local phase-field variable for the AT2 brittle fracture model. Thereafter, numerical experiments are carried out on benchmark problems (single edge notched specimen under tension and shear, three-point bending, and notched concrete specimen with hole) to investigate the effect of the penalty term on the global response (load-displacement curves) and the fracture length-scale. Through a parametric study, it is shown that an optimal value of the penalty parameter exists for which the global response as well as the fracture length-scale of the micromorphic model is similar to that of the original model.

***K*eywords** phase-field fracture · micromorphic · irreversibility · fully coupled · monolithic

1 Introduction

The phase-field model for fracture belongs to the smeared (continuous) representation of fracture in computational mechanics. It enables a straightforward handling of topologically complex (branching, kinking and merging of cracks) fractures, and is capable of operating on a fixed mesh, thereby eliminating tedious re-meshing process associated with the discrete fracture models like XFEM [1, 2], Cohesive Zone Models [3]. Due to the aforementioned reason, the phase-field model for fracture has grown in popularity and offers a promising alternative to discrete fracture models. For a comprehensive comparison of discrete and phase-field fracture models, the reader is referred to [4], and references therein.

The variational treatment of the Griffith fracture criterion [5] and its numerical implementation in [6] pioneered the phase-field approach to fracture modelling. The model introduces an auxiliary variable, the phase-field, which interpolates between intact and fully broken material states. The phase-field model for fracture was cast into a thermodynamically consistent framework in [7], which led to further extensions towards ductile fracture [8, 9], anisotropic fracture [10, 11], hydraulic fracture [12–14], desiccation cracking [15–17], corrosion [18, 19], fracture in thin films [20], to cite a few single-scale applications. The phase-field fracture model has also been extended towards concurrent multi-scale modelling in [21–24] and hierarchical multi-scale modelling in [25, 26].

The popularity of the phase-field model for fracture comes at the cost of minimising a non-convex energy functional. It is well-established in mathematical literature that the conventional Newton-Raphson (NR) method performs poorly in such cases. In order to circumvent this issue, [27] proposed the use of a novel line search technique that also included a negative search direction, while [28] proposed a convexification approach based on extrapolation of the phase-field in time. Other approaches within the monolithic framework include modified Newton methods [29], error-oriented Newton methods [30], arc-length solvers [31], and trust region methods [32]. Alternatively, [33] proposed the use of alternate minimisation (staggered) solution techniques, exploiting the convex nature of the energy functional w.r.t. displacement and phase-field individually. In this manuscript, the NR method is adopted, aware of the fact that convergence issues may arise.

Another computational challenge associated with the phase-field model for fracture is the variational inequality problem arising due to the fracture irreversibility constraint. In this context, [27, 34] opted for a simple penalisation technique, [28] proposed a primal-dual active set method, while [29, 30] adopted an Augmented Lagrangian formulation based on the Moreau-Yoshida indicator function. In an alternative approach, [33] introduced an implicit history-variable as the fracture driving energy in order to ensure fracture irreversibility. However, the variational consistency of the history-variable approach to the original phase-field fracture problem is still not proven. For a comprehensive discussion on the computational challenges associated with the phase-field model for fracture, the reader is referred to the review works [35–37].

The focus of this manuscript lies in developing a method that is able to treat the phase-field fracture irreversibility locally (i.e., only at Gauss points). To this end, a micromorphic extension of the phase-field fracture energy functional is carried out in the spirit of [38, 39]. As shown later in this manuscript, this results in a local phase-field variable and introduces a micromorphic solution field for regularisation. As a consequence, the update of the phase-field variable can be carried out via local Karush-Kuhn-Tucker (KKT) conditions along with enforcement of the bounds. In this manuscript, a strategy for choosing an optimal penalty term is devised. Thereafter, its influence on the fracture length-scale and the global response (for instance, load-displacement curves) is discussed.

This manuscript is structured as follows: Section 2 introduces the reader to the phase-field model for fracture, its underlying energy functional and pertinent Euler-Lagrange equations. Subsequently, in Section 3, the micromorphic approach for phase-field fracture is introduced. The numerical benchmark problems are addressed in Section 4, followed by concluding remarks in Section 5.

2 Phase-field fracture model

Figure 1a and 1b illustrates a discrete and a phase-field regularised fracture respectively, in a continuum. The fracture embedded continuum is assumed to occupy a domain $\Omega \in \mathbb{R}^{\text{dim}}$ ($\text{dim} = 2$ in this case). The external boundary Γ comprises of the Dirichlet and Neumann boundaries, represented by Γ^u_D and Γ^u_N respectively. Note that $\Gamma = \Gamma^u_D \cup \Gamma^u_N$ and $\Gamma^u_D \cap \Gamma^u_N = \emptyset$.

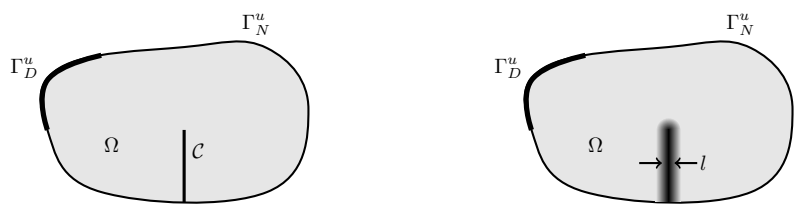

(a) sharp crack

(b) diffused (smeared) crack

Figure 1: A solid $\Omega \in \mathbb{R}^2$ embedded with (a). sharp crack $\mathcal{C}$ and (b). diffused (smeared) crack, with Dirichlet and Neumann boundaries indicated as Γ^u_D and Γ^u_N respectively. Figure adopted from [26]
.

The energy functional pertaining to the phase-field model for fracture [27, 34] is given by,

$$E(\mathbf{u}, \varphi) = \int_\Omega g(\varphi)\Psi^+(\boldsymbol{\epsilon}[\mathbf{u}])\,\mathrm{d}\Omega + \int_\Omega \Psi^-(\boldsymbol{\epsilon}[\mathbf{u}])\,\mathrm{d}\Omega - \int_{\Gamma^u_N} \mathbf{t}^u_p \cdot \mathbf{u}\,\mathrm{d}\Gamma + \int_\Omega G_c \left(\frac{1}{2l}\varphi^2 + \frac{l}{2}|\boldsymbol{\nabla}\varphi|^2\right)\,\mathrm{d}\Omega, \quad (1)$$

where $\Psi^+(\boldsymbol{\epsilon}[\mathbf{u}])$ and $\Psi^-(\boldsymbol{\epsilon}[\mathbf{u}])$ represent the fracture driving and residual strain energy densities respectively. They are functions of the strain $\boldsymbol{\epsilon}[\mathbf{u}]$, defined as the symmetric gradient of the displacement $\mathbf{u}$,

$$\boldsymbol{\epsilon}[\mathbf{u}] = (\mathbf{u} \otimes \boldsymbol{\nabla})^{\text{sym}}. \tag{2}$$

Assuming that fracture is driven by tensile strain energy [7], in this manuscript, $\Psi^+(\boldsymbol{\epsilon}[\mathbf{u}])$ and $\Psi^-(\boldsymbol{\epsilon}[\mathbf{u}])$ represent the tensile and compressive strain energy densities. They are computed as,

$$\Psi^{\pm}(\boldsymbol{\epsilon}[\mathbf{u}]) = \frac{1}{2}\lambda\langle(\mathbf{I}\colon \boldsymbol{\epsilon}[\mathbf{u}])\rangle_{\pm}^2 + \mu\boldsymbol{\epsilon}^{\pm}[\mathbf{u}]\colon \boldsymbol{\epsilon}^{\pm}[\mathbf{u}], \tag{3}$$

where λ and μ are the Lamé constants, $\mathbf{I}$ is a second-order identity tensor, with $\boldsymbol{\epsilon}^{\pm}[\mathbf{u}]$ defined as,

$$\boldsymbol{\epsilon}^{\pm}[\mathbf{u}] = \sum_{i=1}^{\dim}\langle\epsilon_i\rangle_{\pm}\mathbf{p}_i \otimes \mathbf{p}_i. \tag{4}$$

In Equations (3) and (4), $\langle\bullet\rangle_{\pm}$ indicates the positive/negative Macaulay brackets. Moreover, ϵ_i is the i^{th} principal (eigen) strain, while $\mathbf{p}_i$ is its corresponding normalised eigenvector. The degradation function, $g(\varphi)$ is a strictly decreasing monotone with properties $g(0) = 1$, $g(1) = 0$, and $g'(1) = 0$. The first two properties ensure intact and fully broken material states, while the last property results in a zero fracture driving energy for fully broken material. In this manuscript, the degradation function is chosen as $g(\varphi) = (1-\varphi)^2$. Furthermore, the surface traction on the Neumann boundary Γ_N^u is denoted by $\mathbf{t}_p^u$, and the last integral corresponds to Ambrosio-Tortorelli (AT2) phase-field regularised fracture energy term [6], with the Griffith energy denoted by G_c.

The subsequent part of this manuscript uses the tensile and compressive stresses, obtained via derivative of the tensile and compressive strain energy densities. They are given by,

$$\boldsymbol{\sigma}^{\pm} = \frac{\partial\Psi^{\pm}}{\partial\boldsymbol{\epsilon}} = \lambda\langle(\mathbf{I}\colon \boldsymbol{\epsilon}[\mathbf{u}])\rangle_{\pm}\mathbf{I} + 2\mu\boldsymbol{\epsilon}^{\pm}[\mathbf{u}]. \tag{5}$$

The numerical simulation of fracture initiation and propagation in a continuum domain Ω requires the minimisation of the energy functional (1) w.r.t. its solution variables $\mathbf{u}$ and φ. Along with appropriately defined test and trial spaces, the problem takes the form:

Problem 1 *Find ($\mathbf{u}$, φ) $\in \mathbb{U} \times \mathbb{P}$ with*

$$\int_\Omega \left((1-\varphi)^2 + \kappa\right)\boldsymbol{\sigma}^+\colon \boldsymbol{\epsilon}[\delta\mathbf{u}]\,\mathrm{d}\Omega + \int_\Omega \boldsymbol{\sigma}^-\colon \boldsymbol{\epsilon}[\delta\mathbf{u}]\,\mathrm{d}\Omega \tag{6a}$$

$$- \int_{\Gamma_N^{\mathbf{u}}} \mathbf{t}_p^u\,\delta\mathbf{u}\,\mathrm{d}\Gamma = 0 \qquad \forall\,\delta\mathbf{u} \in \mathbb{U}^0, \tag{6b}$$

$$\int_\Omega G_c\left(\frac{1}{l}\varphi\,(\hat{\varphi}-\varphi) + l\,\boldsymbol{\nabla}\varphi\cdot\boldsymbol{\nabla}(\hat{\varphi}-\varphi)\right)\mathrm{d}\Omega - \int_\Omega 2(1-\varphi)\Psi^+(\hat{\varphi}-\varphi)\,\mathrm{d}\Omega \geq 0 \qquad \forall\,\hat{\varphi} \in \mathbb{P}, \tag{6c}$$

using pertinent time-dependent Dirichlet boundary conditions $\mathbf{u}^p$ on Γ_D^u and φ^p on Γ_D^φ, and and Neumann boundary condition $\mathbf{t}_p^{\mathbf{u}}$ on $\Gamma_N^{\mathbf{u}}$. The trial and test spaces are defined as

$$\mathbb{U} = \{\mathbf{u} \in [H^1(\Omega)]^{\dim} | \mathbf{u} = \mathbf{u}^p \text{ on } \Gamma_D^u\}, \tag{7a}$$

$$\mathbb{U}^0 = \{\mathbf{u} \in [H^1(\Omega)]^{\dim} | \mathbf{u} = \mathbf{0} \text{ on } \Gamma_D^u\}, \tag{7b}$$

$$\mathbb{P} = \{\varphi \in [H^1(\Omega)]^1 | \varphi \geq {}^n\varphi | \varphi = \varphi^p \text{ on } \Gamma_D^\varphi\}. \tag{7c}$$

Note that the requirement $\varphi \geq {}^n\varphi$ in (7c) ensures fracture irreversibility, with n referring to the previous time-step. ■

From Problem 1, it is clear that the fracture irreversibility constraint manifests in the form of a variationally inequality Euler-Lagrange equation (6c) with restrictive trial and test set (7c) for the phase-field. As mentioned in Section 1, several researchers have proposed different methods to treat the variational inequality problem. In the next section, a micromorphic phase-field fracture model is proposed, where the phase-field variable becomes local, while a micromorphic variable ensures regularisation of the problem. This enables a simpler treatment of the fracture irreversibility constraint.

3 Micromorphic phase-field fracture model

3.1 Energy functional and Euler-Lagrange equations

A micromorphic extension of the phase-field fracture energy functional (1) in the spirit of [38] results in,

$$\tilde{E}(\mathbf{u},\varphi,d) = \int_\Omega (1-\varphi)^2\Psi^+(\boldsymbol{\epsilon}[\mathbf{u}])\,\mathrm{d}\Omega + \int_\Omega \Psi^-(\boldsymbol{\epsilon}[\mathbf{u}])\,\mathrm{d}\Omega - \int_{\Gamma_N^u} \mathbf{t}_p^u\cdot\mathbf{u}\,\mathrm{d}\Gamma + \int_\Omega G_c\left(\frac{1}{2l}\varphi^2 + \frac{l}{2}|\boldsymbol{\nabla} d|^2\right)\mathrm{d}\Omega + \int_\Omega \frac{\alpha}{2}(\varphi-d)^2\,\mathrm{d}\Omega, \tag{8}$$

where a '*new*' micromorphic variable d is introduced along with a user-defined constant penalty parameter α. From the fracture energy integral, it is observed that only the micromorphic phase-field variable d contributes to the gradient/non-local effect. Consequently, the regularity requirements on the phase-field in terms of the existence of derivatives is circumvented. Moreover, the micromorphic approach also introduces an *additional energy* term associated with the difference between the phase-field and the micromorphic variable. Theoretically, in the limit, $\alpha \to \infty$, the original energy functional (1) is recovered.

Similar to Section 2, the set of Euler-Lagrange equations for the micromorphic phase-field fracture model is obtained upon minimising the energy functional (8) w.r.t. its solution variables $\mathbf{u}$, φ and d. Along with appropriately defined test and trial spaces, the complete problem is given by:

Problem 2 *Find (*$\mathbf{u}$*,* φ*,* d*)* $\in \mathbb{U}\times\mathbb{P}\times\mathbb{D}$ *with*

$$\int_\Omega (1-\varphi)^2\boldsymbol{\sigma}^+ \colon \boldsymbol{\epsilon}[\delta\mathbf{u}]\,\mathrm{d}\Omega + \int_\Omega \boldsymbol{\sigma}^- \colon \boldsymbol{\epsilon}[\delta\mathbf{u}]\,\mathrm{d}\Omega - \int_{\Gamma_N^{\mathbf{u}}} \mathbf{t}_p^u\,\delta\mathbf{u}\,\mathrm{d}\Gamma = 0 \qquad \forall\,\delta\mathbf{u}\in\mathbb{U}^0, \tag{9a}$$

$$\int_\Omega -2(1-\varphi)\Psi^+(\hat{\varphi}-\varphi)\,\mathrm{d}\Omega + \int_\Omega \frac{G_c}{l}\varphi(\hat{\varphi}-\varphi)\,\mathrm{d}\Omega + \int_\Omega \alpha(\varphi-d)(\hat{\varphi}-\varphi)\,\mathrm{d}\Omega \geq 0 \qquad \forall\,\hat{\varphi}\in\mathbb{P}, \tag{9b}$$

$$\int_\Omega G_c l\,\boldsymbol{\nabla} d\cdot\boldsymbol{\nabla}\delta d\,\mathrm{d}\Omega - \int_\Omega \alpha(\varphi-d)\delta d\,\mathrm{d}\Omega = 0 \qquad \forall\,\delta d\in\mathbb{D}, \tag{9c}$$

using pertinent time-dependent Dirichlet and Neumann boundary conditions, $\mathbf{u}^p$ *on* Γ_D^u*, and* $\mathbf{t}_p^{\mathbf{u}}$ *on* $\Gamma_N^{\mathbf{u}}$ *respectively. The trial and test spaces are given by*

$$\mathbb{U} = \{\mathbf{u}\in[H^1(\Omega)]^{\mathrm{dim}} | \mathbf{u} = \mathbf{u}^p \text{ on } \Gamma_D^u\}, \tag{10a}$$

$$\mathbb{U}^0 = \{\mathbf{u}\in[H^1(\Omega)]^{\mathrm{dim}} | \mathbf{u} = \mathbf{0} \text{ on } \Gamma_D^u\}, \tag{10b}$$

$$\mathbb{D} = \{d\in[H^1(\Omega)]^1]\}, \tag{10c}$$

$$\mathbb{P} = \{\varphi\in[L^2(\Omega)] | \varphi \geq {}^n\varphi\}. \tag{10d}$$

■

From Problem 2, it is observed that the phase-field evolution equation (9b) is local. Upon enforcing the bound ${}^n\varphi < \varphi \leq 1$, an expression for the phase-field is obtained as,

$$\varphi\{\Psi^+, d\} = min\left(max\Big(\frac{2\Psi^+ + \alpha d}{2\Psi^+ + \alpha + \frac{G_c}{l}}, {}^n\varphi\Big), 1\right). \tag{11}$$

Note that the curly braces in the above expression indicate the implicit dependence of the phase-field on the fracture driving strain energy density Ψ^+ and the micromorphic variable d. Moreover, the bound ${}^n\varphi < \varphi \leq 1.0$ fulfill the fracture irreversibility constraint on the phase-field variable. Armed with an expression for the phase-field variable, Problem 2 reduces to a (globally) two-field problem, given by:

Problem 3 *Find* $(\mathbf{u},\, d) \in \mathbb{U} \times \mathbb{D}$ *with*

$$\int_\Omega (1-\varphi\{\Psi^+, d\})^2 \boldsymbol{\sigma}^+ \colon \boldsymbol{\epsilon}[\delta\mathbf{u}]\,\mathrm{d}\Omega + \int_\Omega \boldsymbol{\sigma}^- \colon \boldsymbol{\epsilon}[\delta\mathbf{u}]\,\mathrm{d}\Omega - \int_{\Gamma^{\mathbf{u}}_N} \mathbf{t}^u_p\, \delta\mathbf{u}\,\mathrm{d}\Gamma = 0 \qquad \forall\, \delta\mathbf{u} \in \mathbb{U}^0, \tag{12a}$$

$$\int_\Omega G_c \boldsymbol{\nabla} d \cdot \boldsymbol{\nabla}\delta d\,\mathrm{d}\Omega - \int_\Omega \alpha(\varphi\{\Psi^+, d\} - d)\delta\varphi\,\mathrm{d}\Omega = 0 \qquad \forall\, \delta d \in \mathbb{D}, \tag{12b}$$

using (11), and pertinent time-dependent Dirichlet boundary conditions $\mathbf{u}^p$ *on* Γ^u_D *and Neumann boundary condition* $\mathbf{t}^{\mathbf{u}}_p$ *on* $\Gamma^{\mathbf{u}}_N$*. The trial and test spaces are defined as*

$$\mathbb{U} = \{\mathbf{u} \in [H^1(\Omega)]^{\mathrm{dim}} | \mathbf{u} = \mathbf{u}^p \text{ on } \Gamma^u_D\}, \tag{13a}$$

$$\mathbb{U}^0 = \{\mathbf{u} \in [H^1(\Omega)]^{\mathrm{dim}} | \mathbf{u} = \mathbf{0} \text{ on } \Gamma^u_D\}, \tag{13b}$$

$$\mathbb{D} = \{d \in [H^1(\Omega)]^1\}, \tag{13c}$$

■

Remark 1 *Note that the local treatment of the fracture irreversibility in Problem 3 circumvents the need for restrictive trial and test spaces for the phase-field observed in Problem 1.*

Furthermore, denoting (12a) and (12b) as residuals $R^{\mathbf{u}}(\delta\mathbf{u})$ and $R^d(\delta d)$, the tangent form of the micromorphic phase-field fracture model is stated as,

$$\begin{aligned}\int_\Omega \boldsymbol{\epsilon}[\delta\mathbf{u}] \colon \left(g(\varphi)\frac{\partial \boldsymbol{\sigma}^+}{\partial \boldsymbol{\epsilon}} + \frac{\partial \boldsymbol{\sigma}^-}{\partial \boldsymbol{\epsilon}} - g'(\varphi)\boldsymbol{\sigma}^+\,\varphi'_{\boldsymbol{\epsilon}}\right) \colon \boldsymbol{\epsilon}[\mathrm{d}\mathbf{u}]\,\mathrm{d}\Omega \\ + \int_\Omega \boldsymbol{\epsilon}[\delta\mathbf{u}] \colon \left(g'(\varphi)\Psi^+\,\varphi'_d\right)\mathrm{d}d\,\mathrm{d}\Omega = -R^{\mathbf{u}}(\delta\mathbf{u}) \qquad \forall\, \delta\mathbf{u} \in \mathbb{U}^0,\end{aligned} \tag{14a}$$

$$\begin{aligned}\int_\Omega \delta d(-\alpha\,\varphi'_{\boldsymbol{\epsilon}}) \colon \boldsymbol{\epsilon}[\mathrm{d}\mathbf{u}]\,\mathrm{d}\Omega + \int_\Omega \delta d\left(\frac{G_c}{l} + \alpha - \alpha\,\varphi'_d\right)\mathrm{d}d\,\mathrm{d}\Omega \\ + \int_\Omega G_c \boldsymbol{\nabla}\delta d \cdot \boldsymbol{\nabla}\mathrm{d}d\,\mathrm{d}\Omega = -R^d(\delta d) \qquad \forall\, \delta\varphi \in \mathbb{D}^0,\end{aligned} \tag{14b}$$

with

$$\varphi'_{\boldsymbol{\epsilon}} = \begin{cases} \dfrac{\alpha(1-d) + G_c/l}{(2\Psi^+ + \alpha + G_c/l)^2}\, 2\boldsymbol{\sigma}^+, & \text{if } {}^n\varphi < \dfrac{2\Psi^+ + \alpha d}{2\Psi^+ + \alpha + G_c/l} < 1, \\ 0 & \text{otherwise,} \end{cases} \tag{14c}$$

and

$$\varphi'_d = \begin{cases} \dfrac{\alpha}{2\Psi^+ + \alpha + G_c/l}, & \text{if } {}^n\varphi < \dfrac{2\Psi^+ + \alpha d}{2\Psi^+ + \alpha + G_c/l} < 1, \\ 0 & \text{otherwise.} \end{cases} \tag{14d}$$

In this manuscript, the tangent form (14a)-(14d) is discretised using Q1 elements in the commercial finite element software package COMSOL Multiphysics 5.6.

4 Numerical Study

In this section, the micromorphic phase-field fracture model is used to perform numerical experiments on benchmark problems. These include the single edge notched specimen under tension and shear loading, three-point bending, and a notched concrete specimen with a hole. The geometry and material properties, as well as the loading conditions are

presented in the corresponding sub-sections. The phase-field fracture topology and the load-displacement curves are presented therein.

Furthermore, a solution-based convergence criterion, where the weighted Euclidean norm of the solution update,

$$err := \sqrt{\frac{1}{M}}\sqrt{\sum_{j=1}^{M}\frac{1}{N_j}\sum_{i=1}^{N}\left(\frac{|E_{i,j}|}{W_{i,j}}\right)^2} \tag{15}$$

is used to terminate the iterations of the Newton-Raphson method. Here, M indicates the number of fields, j is the number of degree of freedom for each field $j = 1, 2, ..M$, E represents the absolute update (say, $\varphi^{(m)}$-$\varphi^{(m-1)}$ for phase-field, m being the iteration count), and $W_{i,j} = max(|\mathbf{U}_{i,j}|, S_j)$. The entire solution vector is represented with $\mathbf{U}$ and S_j refers to scaling of solution variables[1]. The iterations in each step are terminated when $err < 1e-4$. Finally, the penalty parameter α is parametrised as,

$$\alpha = \beta\frac{G_c}{l}. \tag{16}$$

4.1 Single Edge Notched (SEN) tension test

The SEN specimen is a unit square (in mm) with a horizontal notch, as shown in Figure 2. The notch has been introduced in a discrete fashion in the finite element mesh. The loading is applied at the top boundary in the form of displacement increments $\Delta u = 1e-5$ [mm] for the first 450 steps, following which it is changed to $1e-6$ [mm]. The bottom boundary remains fixed. Furthermore, the material properties are presented in Table 1.

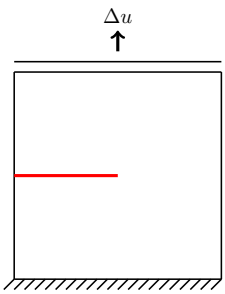

Figure 2: SEN tension test

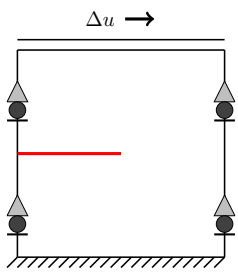

Figure 3: SEN shear test

Property	Value
λ	121.154 [GPa]
μ	80.769 [GPa]
G_c	2700 [N/m]
l	1.5e-2 [mm]
h_{max}	$l/2$

Table 1: SEN material properties

Figure 4a presents the load-displacement curves obtained using the micromorphic phase-field model for fracture, along with those from the literature [7,40]. It is observed that the curves are within close range, with similar pre-peak response, while the post-peak response varies with β. The latter response is due to the local update of the phase-field via (11), which in turn is dependent on β through the parametrisation (16). The parameter β may be thought of, either as a penalty parameter in the regularisation or as a material parameter. In the latter case, the micromorphic phase-field fracture model becomes as alternative fracture model with β computed from calibration of experimental data. In this manuscript, β is chosen as a penalty parameter in the regularisation of the fracture problem.

Having chosen β as a penalty parameter, its influence on the fracture length-scale is investigated. To that end, the phase-field fracture profile is plotted at $x = 0.75$ [mm] for varying β values, along with a reference solution obtained using a slack variable approach [41] in Figure 5a. It is observed that β has minimal impact on the fracture length-scale, and does not scale inversely to β as reported in [39].

Next, an optimal[2] value of β is sought, such that the global response (load-displacement curves) from the micromorphic model is similar that from the original phase-field fracture model (in Problem 1). To that end, the ratio of the micromorphic energy to the fracture energy at the final step of the analysis is plotted in Figure 5b for different β values. For a detailed plot depicting the evolution of the elastic, fracture, and micromorphic energies, the reader is referred to

[1] Scaling of solution variables improves the conditioning of the stiffness matrix.

[2] Optimal w.r.t the finite data points chosen in this manuscript.

Appendix A. Mathematically, the least energy ratio would indicate a micromorphic energy functional (8) converging towards the original phase-field fracture energy functional (1). The corresponding β value is then regarded as the optimal penalty parameter, in this case, 10^2. It is expected that $\beta = 10^2$ would result in a load-displacement response close to that observed in the literature. For the single edge notched specimen, it is observed that $\beta = 10^2$ yields a load-displacement response close that [7, 40]. Also, the phase-field fracture topology at the final step of the analysis, shown in Figure 4b, is similar to the aforementioned literature.

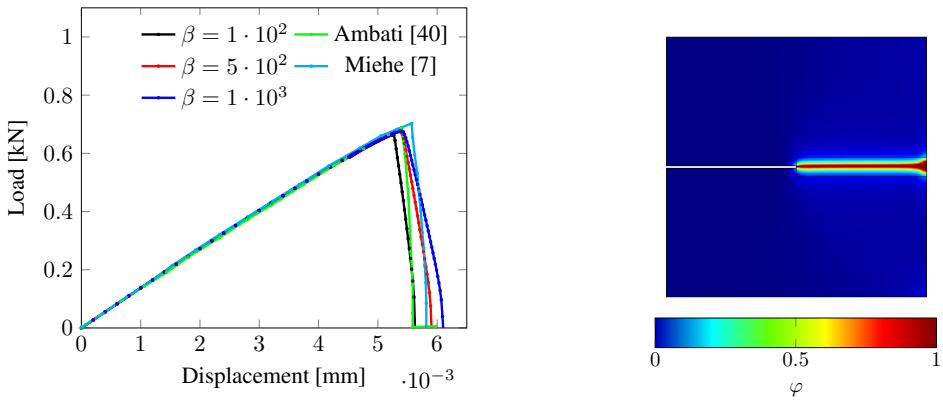

(a) (b)

Figure 4: Figure (a) presents the load-displacement curves obtaining using micromorphic phase-field fracture model with varying β, and [7, 40] for the SEN tension test. Figure (b) shows the distribution of the phase-field variable at the final step of the analysis for $\beta = 1 \cdot 10^2$.

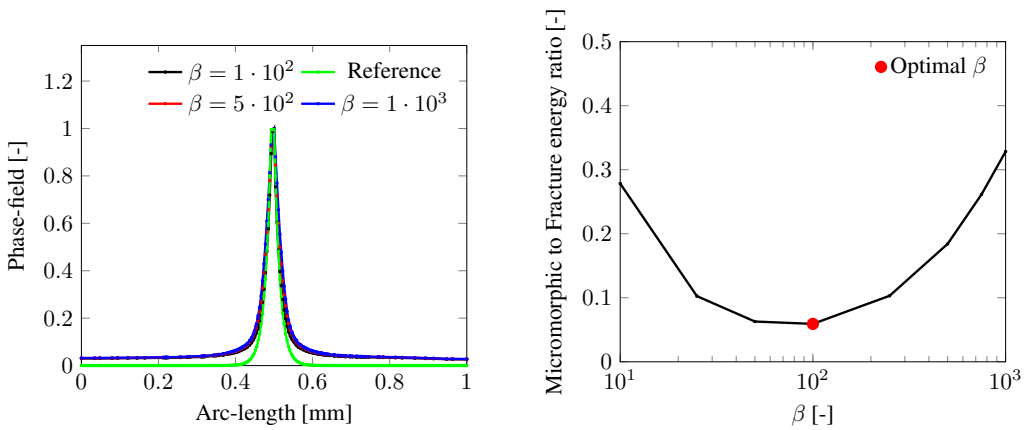

(a) (b)

Figure 5: Figure (a) presents the phase-field fracture profile across $x = 0.75$, with the specimen centered at (0.5,0.5). The reference solution is obtained using the slack variable approach [41]. Figure (b) shows the ratio of the micromorphic energy to the fracture energy at the final step of the analysis for varying β. The optimal β value is indicated with a red marker.

4.2 Single Edge Notched (SEN) shear test

In order to conduct a shear test on the SEN specimen, the loading at the top boundary is set along the horizontal direction, as shown in Figure 3. Moreover, vertical displacements along the left and right boundaries of the specimen is restricted though roller supports. The material properties remain same as presented in Table 1.

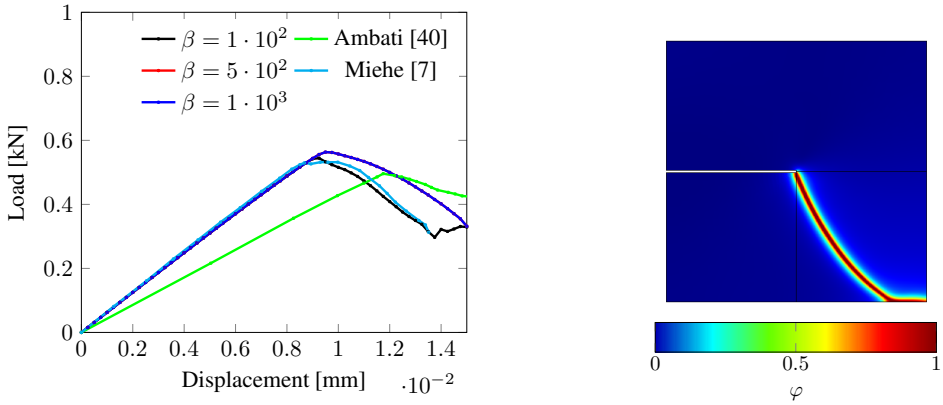

(a) (b)

Figure 6: Figure (a) presents the load-displacement curves obtaining using micromorphic phase-field fracture model with varying β, and [7, 40] for the SEN shear test. Figure (b) shows the distribution of the phase-field variable at the final step of the analysis for $\beta = 1 \cdot 10^2$.

Figure 6a presents the load-displacement curves obtained using the micromorphic phase-field fracture model, along with those from the literature [7, 40]. Similar to the observations made in the case of SEN tension test, the pre-peak behaviour in the load-displacement curves remain similar for different values of β. The post-peak behaviour obtained using $\beta = 10^2$ is close to [7], other choices result in a deviation, albeit in an acceptable range. Moreover, the phase-field fracture topology in the final step of the analysis remains identical to those observed in the phase-field fracture literature.

4.3 Three point bending test

A simply supported beam 8×2 [mm^2] with a triangular notched, as shown in Figure 7, is considered in this study. The notch has a width 0.2 [mm] and height 0.4 [mm]. The loading is applied in the form of displacement increment $\Delta u = 1e-3$ [mm] for the first 35 steps, following which it is changed to 1e-5 [mm], at the midpoint of the top edge. The material properties are presented in Table 2.

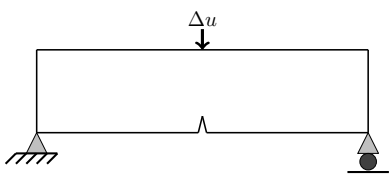

Figure 7: Three point bending test

Property	Value
λ	12 [kN/mm^2]
μ	8 [kN/mm^2]
G_c	1e-3 [kN/mm]
l	3e-2 [mm]
h_{max}	$l/4$

Table 2: Three point bending test material properties

Figure 8a presents the load-displacement curves obtained using the micromorphic phase-field fracture model, along with those from the literature [7, 40]. It is observed that $\beta = 10^2$ yields a response that lies in between the curves from the aforementioned literature. The peak load estimated with the micromorphic phase-field fracture model is similar to that obtained in [7]. Moreover, from Figure 8b, it is observed that the phase-field fracture topology at the final step of the analysis is identical to those reported in the literature.

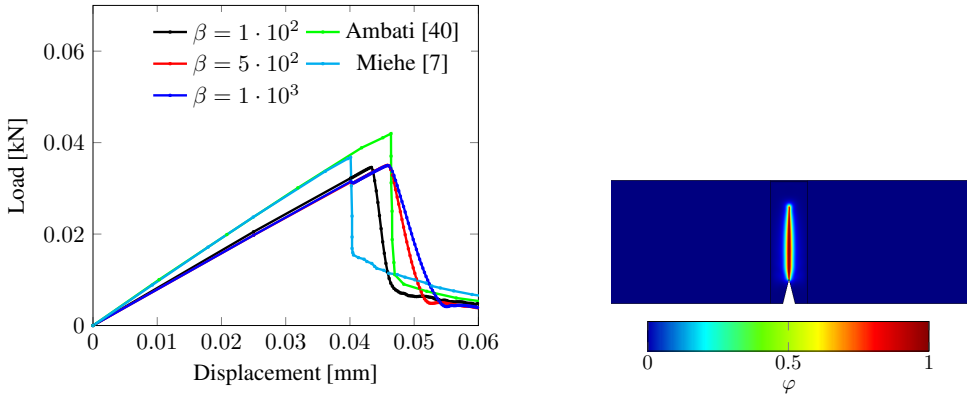

(a) (b)

Figure 8: Figure (a) presents the load-displacement curves obtained using micromorphic phase-field fracture model with varying β, and [7, 40]. Figure (b) shows the distribution of the phase-field fracture variable at the final step of the analysis in a section of the beam for $\beta = 1 \cdot 10^2$.

4.4 Notched specimen with hole

The numerical experiment on the notched specimen with a hole has been adopted from [40], where both experimental and numerical studies were carried out. The specimen is a rectangular plate 65 x 120 [mm^2], embedded with a 10 [mm] notch, 65 [mm] from the bottom edge, and a hole 20 [mm] is diameter at located at (36.5 [mm], 51[mm]). Figure 9 provides a schematic along with the loading conditions. The loading is applied in the form of displacement increment $\Delta u = 1e-3$ [mm] on the upper pin (in grey), while the bottom pin (in grey) is kept fixed. Moreover, the material properties are presented in Table 3.

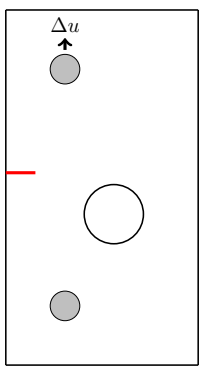

Figure 9: Notched specimen with hole

Figure 10: Experimental results [40]

Property	Value
λ	1.94 [kN/mm^2]
μ	2.45 [kN/mm^2]
G_c	2.28e-3 [kN/mm]
l	0.25 [mm]
h_{max}	$l/2$

Table 3: Material properties for notched specimen with hole

Figure 11a presents the load-displacement curves obtained using the micromorphic phase-field fracture model, along with those from the literature [40, 42]. A similar peak load compared to the literature is obtained for all β values. However, the load-displacement curve using $\beta = 10^2$ is close only with that obtained in [42], and not [40]. This behaviour is attributed to the difference in the fracture length scales adopted for the studies. While [40] opted for $l = 0.1$ [mm], in this study and in [42], $l = 0.25$ [mm]. Finally, the phase-field fracture topology in the final step of the analysis, presented in Figure 11 is found to be similar to that observed in the experimental studies of [40] (see Figure 10).

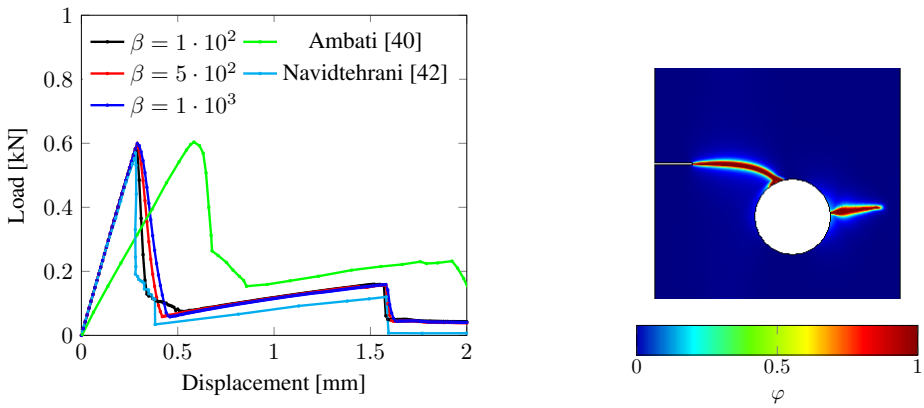

(a) (b)

Figure 11: Figure (a) presents the load-displacement curves obtained using micromorphic phase-field fracture model with varying β, and [40, 42] for the notched specimen with hole test. Figure (b) shows the distribution of the phase-field variable at the final step of the analysis in a section of the specimen for $\beta = 1 \cdot 10^2$.

5 Concluding Remarks

A novel fracture model is proposed in this manuscript, based on the micromorphic extension of the phase-field fracture energy functional. In this model, the phase-field variable is local, and a *new* micromorphic variable is introduced for regularisation. The local nature of the phase-field variable results in a simplified enforcement of fracture irreversibility through local KKT conditions. As demonstrated in this manuscript, the KKT conditions as well as the bounds maybe encapsulated into a single expression. Furthermore, the local phase-field variable also circumvents the need for rather restrictive test and trial spaces associated with the original phase-field fracture model (see Problem 1). This clearly seems to be the benefit of the micromorphic approach.

Furthermore, comparing the micromorphic phase-field fracture energy functional to that of the original phase-field model, it is observed that the latter is recovered as the ratio of the micromorphic energy to fracture energy tends to zero. Therefore, a parametric study is carried out with varying α values to obtain an optimal α that corresponds to the least ratio. Based on the study on the single edge notched specimen under tension, the optimal α is found to be $10^2 G_c/l$. On using this optimal value, the load-displacement curves and the fracture topology at the final step of the analysis for all benchmark problems were found to be similar to that obtained in the literature.

Another aspect investigated in this manuscript is the effect of the penalty parameter α on the fracture length-scale. From the numerical experiments conducted in this manuscript, it is observed that the fracture length-scale remains similar to that from the original phase-field fracture model, for the α values chosen. This behaviour is in contrast with the findings of [39], that the fracture length-scale scales inversely to the square root of the penalty parameter ($l \propto \frac{l}{\sqrt{\beta}}$ if $\alpha = \beta G_c/l$).

For future studies, a simple and straight-forward extension would be towards AT1 brittle fracture model. Other studies may include quasi-brittle fracture with the Griffith fracture energy G_c given by $G_c(\llbracket \mathbf{u} \rrbracket, \kappa)$, $\llbracket \mathbf{u} \rrbracket$ and κ being the displacement jump and an internal variable respectively.

6 Software Implementation and Data

The numerical study in Section 4 is carried out using the equation-based modelling approach in the software package COMSOL Multiphysics 5.6. The source files and data are available in the corresponding author's Github repository (`https://github.com/rbharali`).

A Energies profiles for the SEN specimen under tension

Figure 12, 13 and 14 illustrates the evolution of the elastic energy, fracture energy and the additional micromorphic energy for the Single Edge Notch (SEN) specimen under tension, for varying β values. Note that the penalty-type term α is parametrised as $\alpha = \beta G_c/l$. In all the aforementioned plots, it is observed that the curves are dependent on β. However, it is postulated that an optimal β would result in the least micromorphic energy compared to the fracture energy. It is observed that the blue curve ($\beta = 10^2$) in Figure 14 yields in the least ratio of the micromorphic energy to the fracture energy. Assuming $\beta = 10^2$ as the optimal value, Figure 15 compares the elastic, fracture and micromorphic energy evolution. It is observed that the micromorphic energy remains bounded through the entire evolution, with its ratio to the fracture energy approximately 0.05.

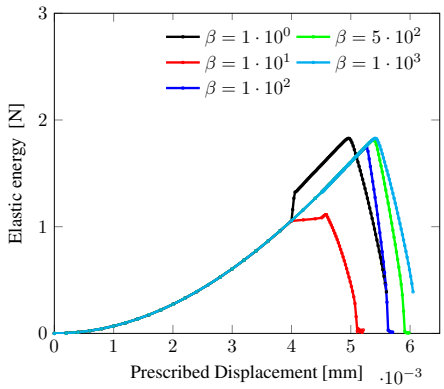

Figure 12: Figure shows the evolution of elastic energy per unit thickness for varying β.

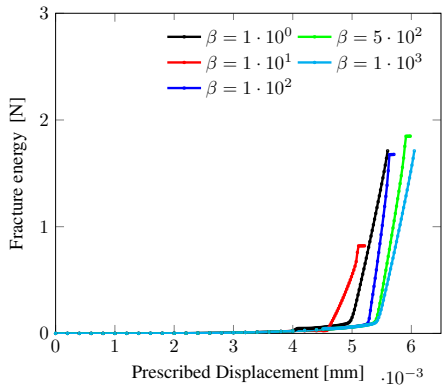

Figure 13: Figure shows the evolution of fracture energy per unit thickness for varying β.

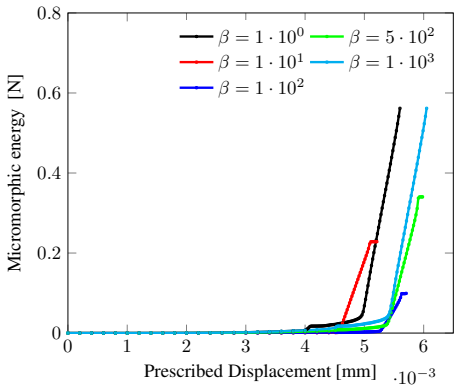

Figure 14: Figure shows the evolution of the micromorphic energy per unit thickness for varying β.

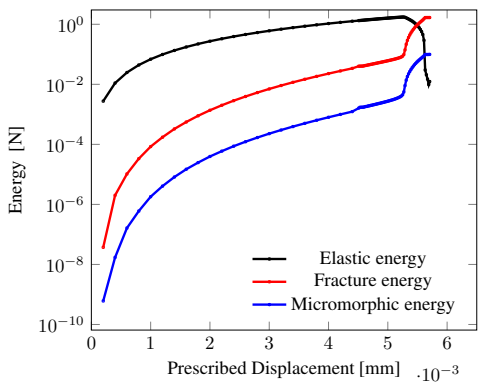

Figure 15: Figure shows the energy profiles per unit thickness versus the timestep for $\beta = 10^2$.

References

[1] Natarajan Sukumar, Nicolas Moës, Brian Moran, and Ted Belytschko. Extended finite element method for three-dimensional crack modelling. *International journal for numerical methods in engineering*, 48(11):1549–1570, 2000.

[2] Nicolas Moës and Ted Belytschko. Extended finite element method for cohesive crack growth. *Engineering fracture mechanics*, 69(7):813–833, 2002.

[3] MGGV Elices, GV Guinea, J Gomez, and J Planas. The cohesive zone model: advantages, limitations and challenges. *Engineering fracture mechanics*, 69(2):137–163, 2002.

[4] Adrian Egger, Udit Pillai, Konstantinos Agathos, Emmanouil Kakouris, Eleni Chatzi, Ian A. Aschroft, and Savvas P. Triantafyllou. Discrete and phase field methods for linear elastic fracture mechanics: A comparative study and state-of-the-art review. *Applied Sciences*, 9(12), 2019.

[5] G.A. Francfort and J.-J. Marigo. Revisiting brittle fracture as an energy minimization problem. *Journal of the Mechanics and Physics of Solids*, 46(8):1319–1342, aug 1998.

[6] B. Bourdin, G.A. Francfort, and J-J. Marigo. Numerical experiments in revisited brittle fracture. *Journal of the Mechanics and Physics of Solids*, 48(4):797 – 826, 2000.

[7] C. Miehe, F. Welschinger, and M. Hofacker. Thermodynamically consistent phase-field models of fracture: Variational principles and multi-field fe implementations. *International Journal for Numerical Methods in Engineering*, 83(10):1273–1311, 2010.

[8] C. Miehe, M. Hofacker, L. M. Schänzel, and F. Aldakheel. Phase field modeling of fracture in multi-physics problems. Part II. Coupled brittle-to-ductile failure criteria and crack propagation in thermo-elastic-plastic solids. *Computer Methods in Applied Mechanics and Engineering*, 294:486–522, 2015.

[9] M. Ambati, T. Gerasimov, and L. De Lorenzis. Phase-field modeling of ductile fracture. *Computational Mechanics*, 55(5):1017–1040, 2015.

[10] S. Teichtmeister, D. Kienle, F. Aldakheel, and M.-A. Keip. Phase field modeling of fracture in anisotropic brittle solids. *International Journal of Non-Linear Mechanics*, 97:1–21, 2017.

[11] Jeremy Bleyer and Roberto Alessi. Phase-field modeling of anisotropic brittle fracture including several damage mechanisms. *Computer Methods in Applied Mechanics and Engineering*, 336:213–236, 2018.

[12] Zachary A. Wilson and Chad M. Landis. Phase-field modeling of hydraulic fracture. *Journal of the Mechanics and Physics of Solids*, 96:264–290, 2016.

[13] Y. Heider and B. Markert. A phase-field modeling approach of hydraulic fracture in saturated porous media. *Mechanics Research Communications*, 80:38–46, 2017. Multi-Physics of Solids at Fracture.

[14] Chukwudi Chukwudozie, Blaise Bourdin, and Keita Yoshioka. A variational phase-field model for hydraulic fracturing in porous media. *Computer Methods in Applied Mechanics and Engineering*, 347:957–982, 2019.

[15] T. Cajuhi, L. Sanavia, and L. De Lorenzis. Phase-field modeling of fracture in variably saturated porous media. *Computational Mechanics*, 61(3):299–318, 2018.

[16] Yousef Heider and WaiChing Sun. A phase field framework for capillary-induced fracture in unsaturated porous media: Drying-induced vs. hydraulic cracking. *Computer Methods in Applied Mechanics and Engineering*, 359:112647, 2020.

[17] Tianchen Hu, Johann Guilleminot, and John E. Dolbow. A phase-field model of fracture with frictionless contact and random fracture properties: Application to thin-film fracture and soil desiccation. *Computer Methods in Applied Mechanics and Engineering*, 368:113106, 2020.

[18] Emilio Martínez-Pañeda, Alireza Golahmar, and Christian F. Niordson. A phase field formulation for hydrogen assisted cracking. *Computer Methods in Applied Mechanics and Engineering*, 342:742–761, 2018.

[19] Philip K. Kristensen, Christian F. Niordson, and Emilio Martínez-Pañeda. A phase field model for elastic-gradient-plastic solids undergoing hydrogen embrittlement. *Journal of the Mechanics and Physics of Solids*, 143:104093, 2020.

[20] A. Mesgarnejad, B. Bourdin, and M.M. Khonsari. A variational approach to the fracture of brittle thin films subject to out-of-plane loading. *Journal of the Mechanics and Physics of Solids*, 61(11):2360 – 2379, 2013.

[21] R.U. Patil, B.K. Mishra, and I.V. Singh. An adaptive multiscale phase field method for brittle fracture. *Computer Methods in Applied Mechanics and Engineering*, 329:254–288, feb 2018.

[22] Tymofiy Gerasimov, Nima Noii, Olivier Allix, and Laura De Lorenzis. A non-intrusive global/local approach applied to phase-field modeling of brittle fracture. *Advanced modeling and simulation in engineering sciences*, 5(1):1–30, 2018.

[23] Lam H Nguyen and Dominik Schillinger. The multiscale finite element method for nonlinear continuum localization problems at full fine-scale fidelity, illustrated through phase-field fracture and plasticity. *Journal of Computational Physics*, 396:129–160, 2019.

[24] Savvas P Triantafyllou and Emmanouil G Kakouris. A generalized phase field multiscale finite element method for brittle fracture. *International Journal for Numerical Methods in Engineering*, 121(9):1915–1945, 2020.

[25] Bang He, Louis Schuler, and Pania Newell. A numerical-homogenization based phase-field fracture modeling of linear elastic heterogeneous porous media. *Computational Materials Science*, 176:109519, 2020.

[26] Ritukesh Bharali, Fredrik Larsson, and Ralf Jänicke. Computational homogenisation of phase-field fracture. *European Journal of Mechanics - A/Solids*, 88:104247, 2021.

[27] T. Gerasimov and L. De Lorenzis. A line search assisted monolithic approach for phase-field computing of brittle fracture. *Computer Methods in Applied Mechanics and Engineering*, 312:276–303, dec 2016.

[28] Timo Heister, Mary F. Wheeler, and Thomas Wick. A primal-dual active set method and predictor-corrector mesh adaptivity for computing fracture propagation using a phase-field approach. *Computer Methods in Applied Mechanics and Engineering*, 2015.

[29] Thomas Wick. Modified Newton methods for solving fully monolithic phase-field quasi-static brittle fracture propagation. *Computer Methods in Applied Mechanics and Engineering*, 2017.

[30] Thomas Wick. An Error-Oriented Newton/Inexact Augmented Lagrangian Approach for Fully Monolithic Phase-Field Fracture Propagation. *SIAM Journal on Scientific Computing*, 39(4):B589–B617, 2017.

[31] Stefan May, Julien Vignollet, and René de Borst. A numerical assessment of phase-field models for brittle and cohesive fracture: $gamma$-convergence and stress oscillations. *European Journal of Mechanics - A/Solids*, 52:72 – 84, 2015.

[32] Alena Kopaničáková and Rolf Krause. A recursive multilevel trust region method with application to fully monolithic phase-field models of brittle fracture. *Computer Methods in Applied Mechanics and Engineering*, 360:112720, 2020.

[33] Christian Miehe, Martina Hofacker, and Fabian Welschinger. A phase field model for rate-independent crack propagation: Robust algorithmic implementation based on operator splits. *Computer Methods in Applied Mechanics and Engineering*, 199(45-48):2765–2778, 2010.

[34] T. Gerasimov and L. De Lorenzis. On penalization in variational phase-field models of brittle fracture. *Computer Methods in Applied Mechanics and Engineering*, 354:990 – 1026, 2019.

[35] Jian-Ying Wu, Vinh Phu Nguyen, Chi Thanh Nguyen, Danas Sutula, Sina Sinaie, and Stéphane P.A. Bordas. *Chapter One - Phase-field modeling of fracture*, volume 53 of *Advances in Applied Mechanics*. Elsevier, 2020.

[36] Thomas Wick. *Multiphysics Phase-Field Fracture: Modeling, Adaptive Discretizations, and Solvers*, volume 28. Walter de Gruyter GmbH & Co KG, 2020.

[37] Laura De Lorenzis and Tymofiy Gerasimov. Numerical implementation of phase-field models of brittle fracture. In *Modeling in Engineering Using Innovative Numerical Methods for Solids and Fluids*, pages 75–101. Springer, 2020.

[38] Samuel Forest. Micromorphic approach for gradient elasticity, viscoplasticity, and damage. *Journal of Engineering Mechanics*, 135(3):117–131, 2009.

[39] C. Miehe, S. Teichtmeister, and F. Aldakheel. Phase-field modelling of ductile fracture: a variational gradient-extended plasticity-damage theory and its micromorphic regularization. *Philosophical Transactions of the Royal Society A: Mathematical, Physical and Engineering Sciences*, 374(2066):20150170, 2016.

[40] Marreddy Ambati, Tymofiy Gerasimov, and Laura De Lorenzis. A review on phase-field models of brittle fracture and a new fast hybrid formulation. *Computational Mechanics*, 55(2):383–405, 2014.

[41] R.Bharali, F.Larsson, and R. Jänicke. Monolithic solution schemes for phase-field fracture using squared slack variable. Manuscript in preparation.

[42] Yousef Navidtehrani, Covadonga Betegón, and Emilio Martínez-Pañeda. A unified abaqus implementation of the phase field fracture method using only a user material subroutine. *Materials*, 14(8), 2021.

PAPER B

Phase-field fracture irreversibility using the slack variable approach

Ritukesh Bharali, Fredrik Larsson, Ralf Jänicke

Manuscript to be submitted for publication

PHASE-FIELD FRACTURE IRREVERSIBILITY USING THE SLACK VARIABLE APPROACH

A PREPRINT

Ritukesh Bharali
Department of Industrial and Materials Science
Chalmers University of Technology
Gothenburg, 412 56, Sweden
ritukesh.bharali@chalmers.se

Fredrik Larsson
Department of Industrial and Materials Science
Chalmers University of Technology
Gothenburg, 412 56, Sweden
fredrik.larsson@chalmers.se

Ralf Jänicke
Institute of Applied Mechanics
Technische Universität Braunschweig
Braunschweig, 38106, Germany
r.janicke@tu-braunschweig.de

September 5, 2021

ABSTRACT

In this manuscript, the phase-field fracture irreversibility constraint is transformed into an equality-based constraint using the slack variable approach. The equality-based fracture irreversibility constraint is then introduced in the phase-field fracture energy functional using the Method of Multipliers and the Penalisation method. Both methods are variationally consistent with conventional variational inequality phase-field fracture problem, unlike the history-variable approach. A simple analytical proof is presented for the former. Thereafter, numerical experiments are carried out on benchmark problems (single edge notched specimen under tension and shear, three-point bending and notched concrete specimen with a hole) to demonstrate the behaviour of the proposed methods.

***K*eywords** phase-field fracture · fully coupled · monolithic solver · Lagrange multiplier · Penalisation · COMSOL

1 Introduction

The phase-field model for fracture emerged from the *seminal work* of [1], wherein the Griffith fracture criterion was cast into a variational setting. Later, a numerical implementation of the same was proposed in [2], using the Ambrosio–Tortorelli regularisation of the Mumford-Shah potential [3]. In this implementation, the fracture is represented by an auxiliary variable, that interpolates between the intact and broken material states. Such a formulation allows the automatic tracking of fractures on a fixed mesh, thereby eliminating the need for the tedious tracking and remeshing processes, observed with discrete methods. Furthermore, the phase-field model for fracture is also able to handle topologically complex (branching, kinking and merging) fractures, and is able to demonstrate fracture initiation without introducing any singularity [4]. Owing to these advantages, the phase-field model for fracture has gained popularity in the computational mechanics community in the past decade.

A thermodynamically consistent formulation of the phase-field fracture model was proposed by [5], adopting an energetic cracking driving force definition. Since then, over the past decade, researchers have extended the work to thermo-mechanical problems at large strain [6], ductile failure [7, 8], fracture in thin films [9], anisotropic fracture [10], fracture in fully/partially saturated porous media [11–13], hydrogen assisted cracking [14], dissolution-driven stress corrosion cracking [15], fracture and fatigue in shape-memory alloys [16], brittle failure of Reisner-Mindlin plates [17] to cite a few. Finally, the phase-field model for fracture has also been used for multi-scale finite element method

[18–20], asymptotic homogenisation [21], and variationally consistent homogenisation [22]. For a detailed overview on the phase-field fracture model, the reader is referred to the comprehensive review works [23–25].

Despite its growing popularity, the phase-field model for fracture poses several challenges when it comes to robust and computationally efficient solution techniques [25]. These include,

(A) the poor performance of the monolithic Newton-Raphson (NR) method due to non-convex energy functional,

(B) variational inequality arising from fracture irreversibility, and

(C) extremely fine meshes are required in the fracture zone.

In order to alleviate the problem concerning the poor-performance of the NR method (A), [26] utilised a *linear extrapolation in time*[1] for the phase-field variable in the momentum balance equation. In [27], a novel line search technique was developed, while in [28] and [29] Augmented Lagrangian and modified NR approaches were proposed. More recently, [30] adopted a recursive multilevel trust region method, that resulted in improved convergence of the NR method. The development of robust, monolithic solution technique is still an active area in phase-field fracture research, and this manuscript is contribution towards this aspect.

The next issue pertains to the variational inequality problem arising out of the fracture irreversibility condition (B). This aspect has been treated in different ways in the phase-field fracture literature. They include crack set irreversibility [2, 31, 32], penalisation [4, 28, 29], and the implicit History variable based method proposed by [33]. The lattermost method remains popular despite its non-variational nature, over-estimation of the fracture surface energy, and the necessity for computationally expensive alternate minimisation (staggered) solution procedure [4]. In a novel approach, this manuscript adopts the slack variable method [34, 35], that constructs an equivalent variational equality problem, while maintaining the variational structure of the original problem.

Another issue pertaining to the phase-field fracture model is the requirement of extremely fine meshes in the smeared fracture zone (C). In this context, [2] and [9] advocates the use of uniformly refined meshes together with parallel computing while [36–38] opted for error-controlled adaptive mesh refinement. Some other approaches include pre-refined meshes when the fracture path is known [4, 23, 27], adaptive mesh refinement in [26] based on a phase-field threshold or Kelly error estimates [39], and multi-level hp-FEM in [40]. In this manuscript, uniform and pre-refined meshes are used.

The novelty of this manuscript lies in the alternative treatment of the fracture irreversibility inequality constraint, using the slack variable approach. The inequality constraint is replaced by an equivalent equality-based fracture irreversibility constraint. The constraint is then augmented to the phase-field fracture energy functional using the Method of Multipliers and the Penalisation method. These methods are variationally consistent, unlike the history-variable approach proposed in [33].

The manuscript is organised as follows: Section 2 introduces the phase-field model for fracture, its underlying energy functional and the Karush-Kuhn-Tucker (KKT) optimality conditions. Thereafter, in Section 3, the Method of Multipliers is adopted to augment the energy functional a slack variable-based fracture irreversibility criterion. The equivalence of the new formulation with the original problem in Section 2 is established in terms of KKT conditions. Furthermore, the Euler-Lagrange equations are presented. In Section 4, the slack variable-based fracture irreversibility constraint is introduced in the energy functional using the Penalisation method, followed by the derivation of the pertinent Euler-Lagrange equations. The numerical experiments on benchmark problems are presented in Section 5, and Section 6 lays down the concluding remarks of this manuscript.

Notation

The following notations are strictly adhered to in this manuscript:

- *Zero-order tensors are represented using small italicized letters, e.g., a. Bold symbols are used for first and second-order tensors, for instance, stress $\boldsymbol{\sigma}$ and strain $\boldsymbol{\epsilon}$.*
- *A function f with its arguments x, y is written in the form $f(x, y)$, whereas a variable g with operational dependencies p, q is written as $g[p, q]$.*
- *The Macaulay operator on a variable x is defined as $\langle x \rangle_{\pm} = \frac{1}{2}(x \pm |x|)$.*

[1] The linear extrapolation of the phase-field variable in time is a questionable assumption although it results in a robust solution method.

2 Phase-field fracture model

2.1 Energy functional

Let $\Omega \in \mathbb{R}^{\text{dim}}$ (dim $= 2, 3$) be the domain occupied by the fracturing solid, shown in Figure 1. Its boundary Γ is decomposed into a Dirichlet boundary Γ_D^u and a Neumann boundary Γ_N^u, such that $\Gamma = \Gamma_D^u \cup \Gamma_N^u$ and $\Gamma_D^u \cap \Gamma_N^u = \emptyset$. Furthermore, the fracture is represented by an auxiliary variable (phase-field) $\varphi \in [0, 1]$ within a diffusive (smeared) zone of width $l > 0$.

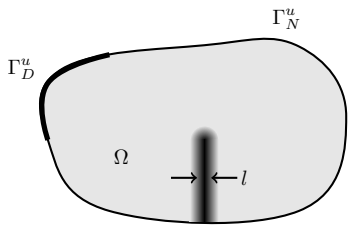

Figure 1: A solid $\Omega \in \mathbb{R}^2$ embedded with a diffused (smeared) crack. Dirichlet and Neumann boundaries are indicated with Γ_D^u and Γ_N^u respectively. Figure adopted from [22].

The energy functional of the phase-field fracture model [4, 27] is given by

$$E(\mathbf{u}, \varphi) = \int_\Omega (g(\varphi) + \kappa)\, \Psi^+(\boldsymbol{\epsilon}[\mathbf{u}])\, \mathrm{d}\Omega + \int_\Omega \Psi^-(\boldsymbol{\epsilon}[\mathbf{u}])\, \mathrm{d}\Omega - \int_{\Gamma_N^u} \mathbf{t}_p^u \cdot \mathbf{u}\, \mathrm{d}\Gamma + \int_\Omega G_c \left(\frac{1}{2l}\varphi^2 + \frac{l}{2}|\boldsymbol{\nabla}\varphi|^2 \right) \mathrm{d}\Omega, \quad (1)$$

where $\Psi^+(\boldsymbol{\epsilon}[\mathbf{u}])$ and $\Psi^-(\boldsymbol{\epsilon}[\mathbf{u}])$ represent the tensile and compressive strain energy densities, which are functions of the symmetric strain energy tensor $\boldsymbol{\epsilon}[\mathbf{u}]$, Moreover,

$$\boldsymbol{\epsilon}[\mathbf{u}] = (\mathbf{u} \otimes \boldsymbol{\nabla})^{\text{sym}}. \quad (2)$$

Following [5],

$$\Psi^\pm(\boldsymbol{\epsilon}[\mathbf{u}]) = \frac{1}{2}\lambda \langle (\mathbf{I} \colon \boldsymbol{\epsilon}[\mathbf{u}]) \rangle_\pm^2 + \mu \boldsymbol{\epsilon}^\pm[\mathbf{u}] \colon \boldsymbol{\epsilon}^\pm[\mathbf{u}], \quad (3)$$

where λ and μ are the Lamé constants, $\mathbf{I}$ is a second-order identity tensor, $\mathbf{u}$ is the displacement, and $\boldsymbol{\epsilon}^\pm[\mathbf{u}]$ is defined as

$$\boldsymbol{\epsilon}^\pm[\mathbf{u}] = \sum_{i=1}^{\text{dim}} \langle \epsilon_i \rangle_\pm \mathbf{p}_i \otimes \mathbf{p}_i \quad (4)$$

where ϵ_i represents the i^{th} eigenvalue of the strain, and $\mathbf{p}_i$ is its corresponding normalised eigenvector. Furthermore, a monotonically decreasing degradation function $g(\varphi) + \kappa$ is attached to $\Psi^+(\boldsymbol{\epsilon}[\mathbf{u}])$ since fracture is expected to occur only under tensile loading. In this manuscript, $g(\varphi) = (1 - \varphi)^2$ and $\kappa = 1e - 10$ (a small term that prevents numerical singularity for partly fractured domains). Next, the surface traction on the Neumann boundary Γ_N^u is denoted by $\mathbf{t}_p^u$, and the last integral corresponds to phase-field regularised fracture energy term [2], where G_c is the Griffith fracture energy.

In the subsequent sections of this manuscript, the tensile and compressive stress are used in the Euler-Lagrange equations. They are defined as

$$\boldsymbol{\sigma}^\pm = \frac{\partial \Psi^\pm}{\partial \boldsymbol{\epsilon}} = \lambda \langle (\mathbf{I} \colon \boldsymbol{\epsilon}[\mathbf{u}]) \rangle_\pm \mathbf{I} + 2\mu \boldsymbol{\epsilon}^\pm[\mathbf{u}]. \quad (5)$$

The prediction of fracture initiation and propagation in the solid occupying the domain Ω requires solving the constrained minimisation problem:

Problem 1 *Find* $\mathbf{u}$ *and* φ *for all times* $t \in [0, T]$ *such that,*

$$min_{\mathbf{u}(t),\varphi(t)} E \quad \textit{and} \quad h(\varphi) \geq 0, \tag{6}$$

where $h(\varphi) = \varphi - {}^{n}\varphi$*, and the left superscript* n *denotes the previous time-step. Moreover, the problem is augmented with (pseudo) time-dependent Dirichlet boundary conditions* $\mathbf{u}^p$ *on* Γ_D^u *and* φ^p *on* Γ_D^φ*, and/or Neumann boundary conditions* $\mathbf{t}_p^u$ *on* Γ_N^u *and* $\mathbf{t}_p^\varphi$ *on* Γ_N^φ*. Furthermore, the boundary* Γ *is split as* $\Gamma = \Gamma_D^u \cup \Gamma_N^u$*,* $\Gamma_D^u \cap \Gamma_N^u = \emptyset$ *and* $\Gamma = \Gamma_D^\varphi \cup \Gamma_N^\varphi$*,* $\Gamma_D^\varphi \cap \Gamma_N^\varphi = \emptyset$ *respectively.* ■

2.2 Karush-Kuhn-Tucker conditions

The KKT triple $(\mathbf{u}, \varphi, \Lambda)$ in appropriate spaces for the Problem 1 requires

$$E'(\mathbf{u}, \varphi, \theta, \Lambda; \mathbf{u}) = 0, \tag{7a}$$
$$E'(\mathbf{u}, \varphi, \theta, \Lambda; \varphi) = 0, \tag{7b}$$
$$h(\varphi) \geq 0, \tag{7c}$$
$$\Lambda \geq 0, \tag{7d}$$
$$\Lambda h(\varphi) = 0 \tag{7e}$$

to hold. Equations (7a) and (7b) represent the Euler-Lagrange equations pertaining to the stationary condition, while equations (7c-7e) are the primal and dual feasibility conditions, and the complementary slackness. Formally, the latter set of equations enforces fracture irreversbility. To the same end, alternative, but equivalent formulations have been adopted in the phase-field fracture literature. For instance, [26] adopted the primal-dual active set strategy proposed by [41], [28] utilised an Augmented Lagrangian penalisation approach with the Moreau-Yoshida indicator function, and [4] opted for a simple penalisation approach. The authors would like to emphasise that the rather popular history-variable approach in [5] is not variationally consistent.

3 Method of Multipliers (MM)

3.1 Fracture irreversibility and modified energy functional

In order to enforce fracture irreversibility $h(\varphi) = \varphi - {}^{n}\varphi \geq 0$, a slack variable is defined as

$$\theta^2 = h(\varphi) = \varphi - {}^{n}\varphi. \tag{8}$$

It is observed that θ^2 admits value greater than or equal to zero, thereby fulfilling the fracture irreversibility criterion. Next, the constrained minimisation Problem 1 is reformulated as:

Problem 2 *Find* $\mathbf{u}$*,* φ *and* θ *for all times* $t \in [0, T]$ *such that,*

$$\begin{aligned} &min_{\mathbf{u}(t),\varphi(t),\theta(t)} \ E \\ &\textit{subjected to} \ \ h(\varphi) - \theta^2 = 0. \end{aligned} \tag{9}$$

with suitable (pseudo) time-dependent Dirichlet and/or Neumann boundary conditions, as mentioned in Problem 1. ■

Augmenting the equality constraint (9) in (1) via the Lagrange multiplier Λ results in the modified energy functional,

$$\tilde{E}(\mathbf{u}, \varphi, \theta, \Lambda) = E(\mathbf{u}, \varphi) + \Lambda\big(h(\varphi) - \theta^2\big). \tag{10}$$

3.2 Stationary conditions

The stationary conditions for the Problem 2 are given by

$$\tilde{E}'(\mathbf{u}, \varphi, \theta, \Lambda; \delta\mathbf{u}) = 0, \tag{11a}$$
$$\tilde{E}'(\mathbf{u}, \varphi, \theta, \Lambda; \delta\varphi) = 0, \tag{11b}$$
$$\tilde{E}'(\mathbf{u}, \varphi, \theta, \Lambda; \delta\theta) = 0, \tag{11c}$$
$$\tilde{E}'(\mathbf{u}, \varphi, \theta, \Lambda; \delta\Lambda) = 0. \tag{11d}$$

The equivalence of these conditions with those presented for Problem 1 can be proved trivially. For instance, (7c) implies that there exists a θ such that (11d) holds. Next, (11c) is proven using (7e) and (11d) with minor algebraic manipulations. More specifically, if $(\mathbf{u}^*, \varphi^*, \theta^*)$ is a global (local) optimal solution of Problem 2, then $(\mathbf{u}^*, \varphi^*)$ is the global (local) optimal solution of Problem 1. Conversely, if $(\mathbf{u}^*, \varphi^*)$ is the global (local) optimal solution of Problem 1, then there exists a certain θ^* such that $(\mathbf{u}^*, \varphi^*, \theta^*)$ is a global (local) optimal solution of Problem 2. For more details on this aspect, refer to Proposition 3.1 in [42].

3.3 Euler-Lagrange equations

The Euler-Lagrange equations for Problem 2 are (11a)-(11d), obtained upon taking the first variation of the energy functional (10) w.r.t its solution variables $\mathbf{u}$, φ, θ and Λ. This results in,

Problem 3 *Find* $(\mathbf{u}, \varphi, \theta, \Lambda) \in \mathbb{U} \times \mathbb{V} \times \mathbb{W} \times \mathbb{A}$ *with*

$$R^{\mathbf{u}} = \int_\Omega \big((g(\varphi) + \kappa)\boldsymbol{\sigma}^+[\mathbf{u}] + \boldsymbol{\sigma}^-[\mathbf{u}]\big) : \boldsymbol{\epsilon}[\delta\mathbf{u}] \, \mathrm{d}\Omega = 0 \qquad \forall\, \delta\mathbf{u} \in \mathbb{U}^0 \tag{12a}$$
$$R^{\varphi} = \int_\Omega \left(\frac{G_c}{l}\varphi + g'(\varphi)\Psi^+(\boldsymbol{\epsilon}[\mathbf{u}]) + \Lambda\right)\delta\varphi \, \mathrm{d}\Omega + \int_\Omega G_c l \boldsymbol{\nabla}\varphi \cdot \boldsymbol{\nabla}\delta\varphi \, \mathrm{d}\Omega = 0 \qquad \forall\, \delta\varphi \in \mathbb{V}^0 \tag{12b}$$
$$R^{\theta} = \int_\Omega -2\Lambda\theta\delta\theta \, \mathrm{d}\Omega = 0 \qquad \forall\, \delta\theta \in \mathbb{W} \tag{12c}$$
$$R^{\Lambda} = \int_\Omega \big(h(\varphi) - \theta^2\big)\delta\Lambda \, \mathrm{d}\Omega = 0 \qquad \forall\, \delta\Lambda \in \mathbb{A}. \tag{12d}$$

with trial function spaces

$$\mathbb{U} := \{\mathbf{u} \in [H^1(\Omega)]^{\dim} | \mathbf{u} = \mathbf{u}^{\mathrm{p}} \text{ on } \Gamma_D^u\}, \tag{13a}$$
$$\mathbb{V} := \{\varphi \in [H^1(\Omega)]^1 | \varphi = \varphi^{\mathrm{p}} \text{ on } \Gamma_D^\varphi\}, \tag{13b}$$
$$\mathbb{W} := \{\theta \in [L_2(\Omega)]\}, \tag{13c}$$
$$\mathbb{A} := \{\Lambda \in [L_2(\Omega)]\}, \tag{13d}$$

and test function spaces

$$\mathbb{U}^0 := \{\mathbf{u} \in [H^1(\Omega)]^{\dim} | \mathbf{u} = 0 \text{ on } \Gamma_D^u\}, \tag{14a}$$
$$\mathbb{V}^0 := \{\varphi \in [H^1(\Omega)]^1 | \varphi = 0 \text{ on } \Gamma_D^\varphi\}, \tag{14b}$$

and pertinent (pseudo) time-dependent Neumann condition

$$\mathbf{t} := \big((1-\varphi)^2\boldsymbol{\sigma}^+ + \boldsymbol{\sigma}^-\big) \cdot \mathbf{n} = \mathbf{t}_p^u \text{ on } \Gamma_N^u. \tag{15}$$

■

Remark 1 *In the event Λ and θ are zero, their stiffness contribution is zero and the stiffness matrix is singular. In order to avoid this situation a fictitious stiffness is introduced to guarantee solvability.*

4 Penalisation (Pen.) method

4.1 The energy functional

In an alternative approach, the squared slack variable equation (8) is introduced in the energy functional (1) as a quadratic term via penalisation. This results in the modified energy functional,

$$\overline{E}(\mathbf{u},\varphi,\theta) = E(\mathbf{u},\varphi) + \frac{\eta}{2}||h(\varphi)-\theta^2||^2, \tag{16}$$

where η is the penalty parameter.

4.2 Euler-Lagrange equations

The Euler-Lagrange equations are obtained upon taking the first variation of the energy functional (16) w.r.t its solution variables $\mathbf{u}$, φ and θ. This results in:

Problem 4 *Find ($\mathbf{u}$, φ, θ) $\in \mathbb{U} \times \mathbb{V} \times \mathbb{W}$ with*

$$R^{\mathbf{u}} = \int_\Omega \left((g(\varphi)+\kappa)\boldsymbol{\sigma}^+[\mathbf{u}] + \boldsymbol{\sigma}^-[\mathbf{u}]\right) : \boldsymbol{\epsilon}[\delta\mathbf{u}]\,\mathrm{d}\Omega = 0 \qquad \forall\,\delta\mathbf{u} \in \mathbb{U}^0 \tag{17a}$$

$$R^{\varphi} = \int_\Omega \left(\frac{G_c}{l}\varphi + g'(\varphi)\Psi^+(\boldsymbol{\epsilon}[\mathbf{u}]) + \eta(h(\varphi)-\theta^2)\right)\delta\varphi\,\mathrm{d}\Omega + \int_\Omega G_c l \boldsymbol{\nabla}\varphi\cdot\boldsymbol{\nabla}\delta\varphi\,\mathrm{d}\Omega = 0 \qquad \forall\,\delta\varphi \in \mathbb{V}^0 \tag{17b}$$

$$R^{\theta} = \int_\Omega -2\eta\theta(h(\varphi)-\theta^2)\delta\theta\,\mathrm{d}\Omega = 0 \qquad \forall\,\delta\theta \in \mathbb{W} \tag{17c}$$

with trial function spaces

$$\mathbb{U} := \{\mathbf{u} \in [H^1(\Omega)]^{\dim} | \mathbf{u} = \mathbf{u}^{\mathrm{p}} \text{ on } \Gamma_D^u\}, \tag{18a}$$

$$\mathbb{V} := \{\varphi \in [H^1(\Omega)]^1 | \varphi = \varphi^{\mathrm{p}} \text{ on } \Gamma_D^\varphi\}, \tag{18b}$$

$$\mathbb{W} := \{\theta \in [L_2(\Omega)]|\}, \tag{18c}$$

and test function spaces

$$\mathbb{U}^0 := \{\mathbf{u} \in [H^1(\Omega)]^{\dim} | \mathbf{u} = 0 \text{ on } \Gamma_D^u\}, \tag{19a}$$

$$\mathbb{V}^0 := \{\varphi \in [H^1(\Omega)]^1 | \varphi = 0 \text{ on } \Gamma_D^\varphi\}, \tag{19b}$$

and pertinent (pseudo) time-dependent Neumann condition

$$\mathbf{t} := \left((1-\varphi)^2\boldsymbol{\sigma}^+ + \boldsymbol{\sigma}^-\right)\cdot\mathbf{n} = \mathbf{t}_p^u \text{ on } \Gamma_N^u. \tag{20}$$

■

Remark 2 *In the event $h(\varphi)-\theta^2$ and θ are zero, their stiffness contribution is zero and the stiffness matrix is singular. In order to avoid this situation a fictitious stiffness is introduced to guarantee solvability.*

5 Numerical Study

The numerical experiments on benchmark problems are presented in this section. They include the Single Edge Notched (SEN) specimen under tension and shear, three-point bending test, a notched specimen with a hole. For each test, the geometry, material properties, and loading conditions are presented in the corresponding sub-sections. The load-displacement curves and the phase-field fracture topology at failure are also presented therein. For the penalisation approach, the penalty parameter η is set to 1 [N/m^2] through the study. This choice is validated through a sensitivity study using different values of η for the SEN specimen under shear, presented in the final sub-section.

Furthermore, the convergence of the NR solver is based on an error measure defined as the weighted Euclidean norm of the solution update,

$$err := \sqrt{\frac{1}{M}} \sqrt{\sum_{j=1}^{M} \frac{1}{N_j} \sum_{i=1}^{N} \left(\frac{|E_{i,j}|}{W_{i,j}} \right)^2}, \tag{21}$$

where M indicates the number of fields, j is the number of degree of freedom for each field $j = 1, 2, ..M$, E represents the absolute update (say, $\mathbf{u}^{(m)}$-$\mathbf{u}^{(m-1)}$ for displacement, m being the iteration count), and $W_{i,j} = max(|\mathbf{U}_{i,j}|, S_j)$. The entire solution vector is represented with $\mathbf{U}$ and S_j refers to scaling of solution variables[2]. The iterations in each (pseudo) time-step are terminated if the solution update err is less than $1e-4$.

The performance of the Newton-Raphson method in conjunction with the Method of Multipliers and the Penalisation method is presented in the sub-section 5.5. Therein, the measure for memory requirements is the the number of DOFs, and the ease of convergence is measured in terms of average iterations required for the simulation, and the maximum iterations required in any step to achieve convergence.

5.1 Single Edge Notched (SEN) tension test

A unit square (in mm) embedded with a horizontal notch, midway along the height is considered, as shown in Figure 2. The length of the notch is equal to half of the edge length of the plate (shown in red). The notch is modelled explicitly in the finite element mesh. A quasi-static loading is applied at the top boundary in the form of prescribed displacement increment $\Delta u = 1e-5$[mm] for the first 450 steps, following which it is changed to $1e-6$[mm]. Furthermore, the bottom boundary remains fixed. The material properties are presented in Table 1.

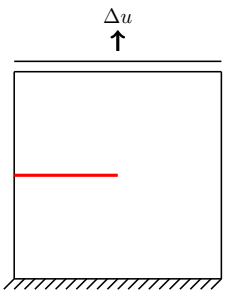

Figure 2: SEN tension test

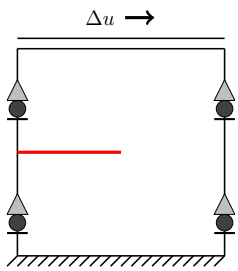

Figure 3: SEN shear test

Property	Value
λ	121.154 [GPa]
μ	80.769 [GPa]
G_c	2700 [N/m]
l	1.5e-2 [mm]
h_{max}	$l/2$

Table 1: SEN material properties

Figure 4a presents the load-displacement curves obtained using the Method of Multipliers (MM) and Penalisation (Pen.) method, along with those from the literature [5, 23]. Both methods yield a similar behaviour compared to [5], in terms of the peak load and the post-peak behaviour. Moreover, the phase-field fracture topology at failure in Figure 4b is also identical to those reported in the aforementioned literature.

5.2 Single Edge Notched (SEN) shear test

In order to perform a shear test, the SEN specimen is loaded horizontally along the top edge as shown in Figure 3. The material properties remain same as presented in Table 1. A quasi-static loading is applied to the top boundary in the form of prescribed displacement increment $\Delta u = 1e-4$[mm] for the first 90 steps, following which it is changed to $1e-5$[mm]. Furthermore, the bottom boundary remains fixed, and roller support is implemented in left and right edges thereby restricting the vertical displacement.

Figure 5a presents the load-displacement curves obtained using the Method of Multipliers and the Penalisation approach, along with those from the literature [5, 23]. The former schemes results in 9% higher peak load estimation as compared to [5] and [23]. However, the phase-field fracture topology in the final step of the analysis is consistent with those reported in the aforementioned literature.

[2]Scaling of solution variables prevents possible ill-conditioning of the stiffness matrix.

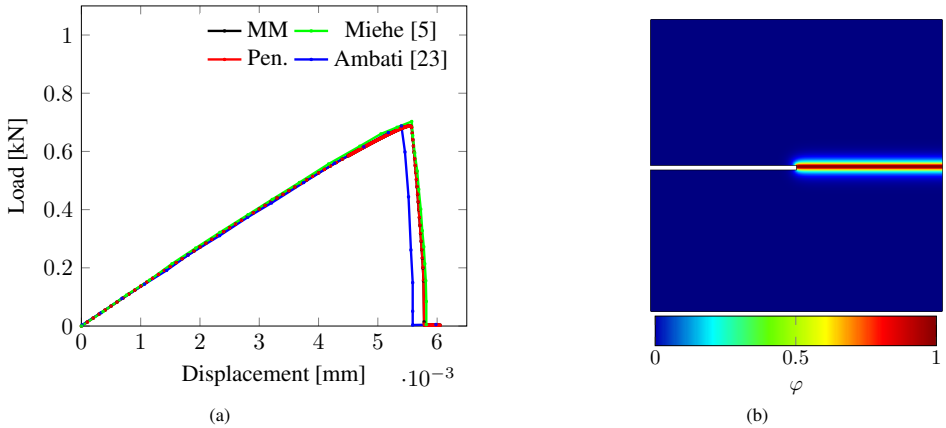

(a) (b)

Figure 4: Figure (a) presents the load-displacement curves for the single edge notched specimen under tension. Here, MM and Pen. refer to the Method of Multipliers and the Penalisation method respectively. Figure (b) shows the distribution of the phase-field variable at the final step of the analysis.

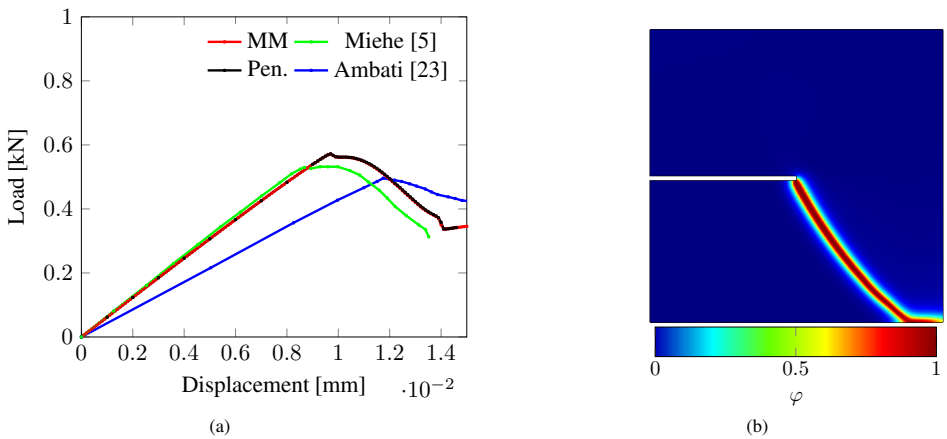

(a) (b)

Figure 5: Figure (a) presents the load-displacement curves for the single edge notched specimen under shear. Here, MM and Pen. refer to the Method of Multipliers and the Penalisation method respectively. Figure (b) shows the distribution of the phase-field variable at the final step of the analysis.

5.3 Three point bending test

A simply supported beam, 8 mm $\times$ 2 mm, with a notch is considered for a three point bending test. The width of the notch is 0.2 mm, the height being 0.4 mm. A schematic of the beam including the boundary conditions is shown in Figure 6. The load increment $\Delta u = 1e-3$ [mm] for the first 35 steps, following which it is set to $1e-5$ [mm]. The material properties of the beam is presented in Table 2.

Figure 7a presents the load-displacement curves obtained using the Method of Multipliers and the Penalisation method, along with those obtained from the literature [5, 23]. These curves lie in between the curves from the literature [5, 23], with the peak load similar to that observed in [5]. Furthermore, the phase-field fracture topology at failure in Figure 7b is identical to those reported in the aforementioned literature.

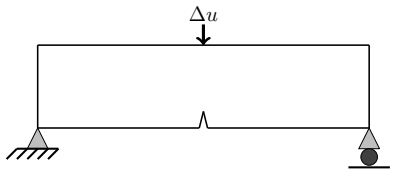

Figure 6: Three point bending test

Symbol	Value
λ	12 [kN/mm^2]
μ	8 [kN/mm^2]
G_c	1e-3 [kN/mm]
l	3e-2 [mm]
h_{max}	$l/4$

Table 2: Material properties for three point bending test

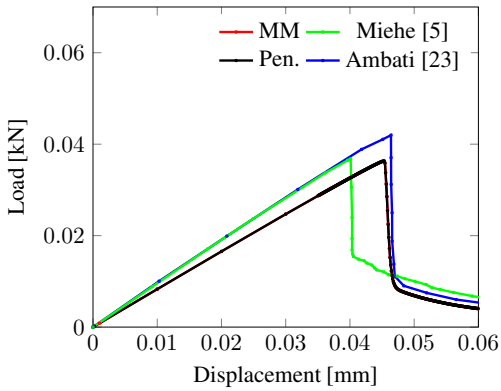

(a) Load-displacement plot

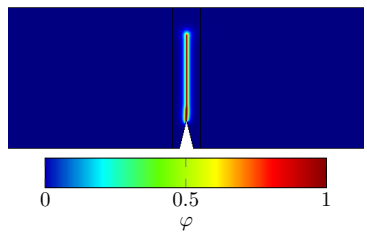

(b)

Figure 7: Figure (a) presents the load-displacement curves for the three-point bending test. Here, MM and Pen. refer to the Method of Multipliers and the Penalisation method respectively. Figure (b) shows the distribution of the phase-field variable at the final step of the analysis in a section of the beam.

5.4 Notched specimen with hole

A notched concrete specimen with a hole, shown in Figure 8 is considered in this study. The experimental and numerical analysis of the same has been carried out in [23]. The specimen has dimensions 65 x 120 [mm^2], the hole being 20 [mm] in diameter located at (36.5 [mm], 51[mm]). Moreover, a notch, 10 [mm] in length is located 65 [mm] from the bottom of the plate. The material properties used in the simulation is presented in Table 3, while the experimentally observed fracture pattern is shown in Figure 9. As shown in Figure 8, the plate is loaded via the upper pin (in grey) with displacement increment $\Delta u = 1e-3$ mm, while the lower pin (in grey) is remains fixed.

Figure 10a presents the load-displacement curves obtained using the Method of Multipliers and the Penalisation method, along with those from the literature [23, 43]. The curves corresponding to the Method of Multipliers and the Penalisation method coincide, and predict peak loads close to those obtained in [23] and [43]. However, the load-displacement curves are significantly different from [23]. The reason for this behaviour is the different fracture length-scales adopted in the studies. While [23] opted for $l = 0.1$ [mm], in this manuscript as well as in [43], $l = 0.25$ [mm]. Finally, from Figure 10b, it observed that the final phase-field fracture topology does match the experimentally observed fracture patterns in Figure 9.

5.5 Performance assessment of the solution schemes

In this sub-section, the performance of the Method of Multipliers and the Penalisation method are compared in terms of memory requirements and ease of convergence. To this end, the number of elements/degrees of freedom, average number of iterations, and maximum iterations required by the Newton-Raphson method to achieved convergence in a single step is presented in Table 4. For each test, the number of elements in the model remains the same. However, due to the Lagrange multiplier field Λ in the Method of Multipliers, more degrees of freedom are required. This conclusively points towards a higher memory usage for the Method of Multipliers, compared to the Penalisation method. In terms of ease of convergence, the Method of Multipliers performs better requiring lesser iterations on an average for the entire

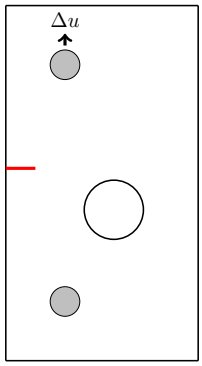

Figure 8: Geometry and constraints

Figure 9: Experimental results [23]

Symbol	Value
λ	1.94 [kN/mm^2]
μ	2.45 [kN/mm^2]
G_c	2.28e-3 [kN/mm]
l	0.25 [mm]
h_{max}	$l/2$

Table 3: Material properties [43]

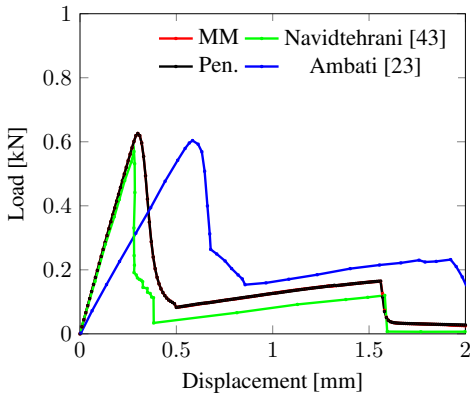

(a)

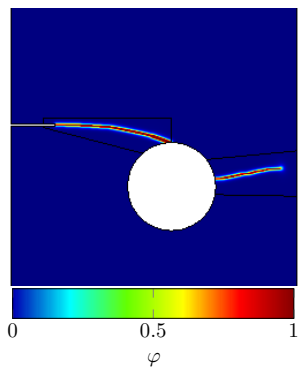

(b)

Figure 10: Figure (a) presents the load-displacement curves for the notched specimen with hole test, obtained from the current implementation, [23], and [43]. Figure (b) shows the distribution of the phase-field variable at the final step of the analysis in a section of the specimen.

simulation. However, when it comes maximum iterations recorded in a single step mixed results are obtained depending on the complexity of the problem.

Test	Elements/DOFs		Avg. Iterations		Max. Iterations	
	MM	Pen.	MM	Pen.	MM	Pen.
SEN Tension	17822/90790	17822/72632	1.1745	2	2	2
SEN Shear	17822/90790	17822/72632	1.5771	2	2	2
Three point bending	38119/106330	38119/85034	1.9640	2.005	15	6
Notched specimen with hole	27998/141236	27998/112990	2.1890	2.2615	14	30

Table 4: Performance assessment of the Method of Multipliers (MM) and Penalisation (Pen.) method. SEN and DOFs are abbreviations for Single Edge Notch and Degrees of Freedom respectively.

5.6 Sensitivity of the numerical solution w.r.t. the penalty parameter η

In this sub-section, the sensitivity of the numerical solution (load-displacement curves) w.r.t the penalty parameter η is assessed. To this end, the SEN specimen under shear is considered. The reader is referred to Section 5.2 for modelling details (geometry, material properties and loading conditions). Figure 11 shows the load-displacement curves obtained using different values of the penalty parameter η (in N/m^2), and the Method of Multipliers. It is observed that, $\eta = 1e+0, 1e+3$ and $1e+6$ produces similar results compared to the Method of Multipliers, while $\eta = 1e+9$ results in a deviation. This implies that $\eta = 1e+0$ [N/m^2] used in the previous studies in Section 5.1-5.4 is reasonable. This is also evident from the load-displacement figures in the aforementioned sub-sections, where the Method of Multipliers and Penalisation method yield similar load-displacement curves.

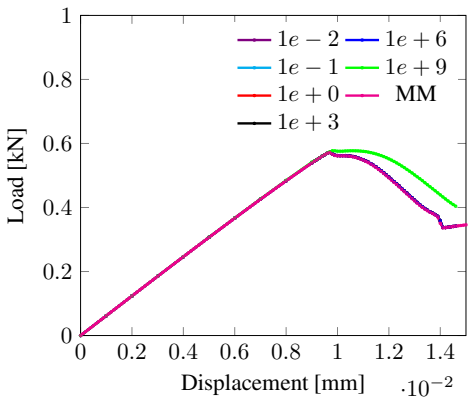

Figure 11: Figure presents the load-displacement curves for the SEN shear test using the Penalisation method and the Method of Multipliers. The penalty parameter η has a unit [N/m^2].

6 Concluding Remarks

An alternative treatment of the phase-field fracture irreversibility is presented in this manuscript, using the slack variable approach. This results in an equivalent equality-based fracture irreversibility constraint. The constraint can then be introduced via the Method of Multipliers or the Penalisation method. The slack variable approach preserves the variational nature of the phase-field fracture problem, unlike the history variable approach in [33]. Numerical experiments are conducted on benchmark AT2 brittle fracture problems to demonstrate the efficacy of the proposed methods. Adopting a solution-based iteration terminating criterion for the Newton-Raphson method, it is observed that a maximum of 30 iterations were required in single step for the notched concrete specimen with a hole. The other benchmark problems required less iterations.

Future studies may involve other phase-field models (AT1, Phase-field regularised Cohesive Zone model [24]), complex multiphysics problems, or simply larger problems with more DOFs. In the lattermost case, block algebraic multigrid preconditioner similar to that adopted in [26] could be designed. Another extension of the current work could be towards accelerating the rate of convergence. In this regard, Andersson's acceleration [44] and the incremental LArge Time INcremental (LATIN) method [45, 46] offers a good starting point. While the Andersson's acceleration requires storing the previous iterates, the incremental LATIN method only requires a symmetric positive definite stiffness matrix. This can be achieved upon eliminating the off-diagonal components of the stiffness matrix in the phase-field fracture problem.

7 Software Implementation and Data Availability

The numerical study in Section 5 is carried out using the equation-based modelling approach in the software package COMSOL Multiphysics 5.6. The source files are available in Github repository of the corresponding author (`https://github.com/rbharali`).

Acknowledgements

The authors would like to acknowledge the financial support from the Swedish Research Council for Sustainable Development (FORMAS) under Grant 2018-01249 and the Swedish Research Council (VR) under Grant 2017-05192.

References

[1] G.A. Francfort and J.-J. Marigo. "Revisiting brittle fracture as an energy minimization problem". In: *Journal of the Mechanics and Physics of Solids* 46.8 (Aug. 1998), pp. 1319–1342. ISSN: 00225096. DOI: 10.1016/S0022-5096(98)00034-9.

[2] B. Bourdin, G.A. Francfort, and J-J. Marigo. "Numerical experiments in revisited brittle fracture". In: *Journal of the Mechanics and Physics of Solids* 48.4 (2000), pp. 797–826. ISSN: 0022-5096. DOI: https://doi.org/10.1016/S0022-5096(99)00028-9.

[3] David Mumford and Jayant Shah. "Optimal approximations by piecewise smooth functions and associated variational problems". In: *Communications on Pure and Applied Mathematics* 42.5 (1989), pp. 577–685. DOI: 10.1002/cpa.3160420503.

[4] T. Gerasimov and L. De Lorenzis. "On penalization in variational phase-field models of brittle fracture". In: *Computer Methods in Applied Mechanics and Engineering* 354 (2019), pp. 990–1026. ISSN: 0045-7825. DOI: https://doi.org/10.1016/j.cma.2019.05.038.

[5] C. Miehe, F. Welschinger, and M. Hofacker. "Thermodynamically consistent phase-field models of fracture: Variational principles and multi-field FE implementations". In: *International Journal for Numerical Methods in Engineering* 83.10 (2010), pp. 1273–1311. DOI: 10.1002/nme.2861.

[6] Christian Miehe, Lisa Marie Schänzel, and Heike Ulmer. "Phase field modeling of fracture in multi-physics problems. Part I. Balance of crack surface and failure criteria for brittle crack propagation in thermo-elastic solids". In: *Computer Methods in Applied Mechanics and Engineering* 294 (2015), pp. 449–485. ISSN: 00457825. DOI: 10.1016/j.cma.2014.11.016.

[7] C. Miehe et al. "Phase field modeling of fracture in multi-physics problems. Part II. Coupled brittle-to-ductile failure criteria and crack propagation in thermo-elastic-plastic solids". In: *Computer Methods in Applied Mechanics and Engineering* 294 (2015), pp. 486–522. ISSN: 00457825. DOI: 10.1016/j.cma.2014.11.017.

[8] M. Ambati, T. Gerasimov, and L. De Lorenzis. "Phase-field modeling of ductile fracture". In: *Computational Mechanics* 55.5 (2015), pp. 1017–1040. ISSN: 1432-0924. DOI: 10.1007/s00466-015-1151-4.

[9] A. Mesgarnejad, B. Bourdin, and M.M. Khonsari. "A variational approach to the fracture of brittle thin films subject to out-of-plane loading". In: *Journal of the Mechanics and Physics of Solids* 61.11 (2013), pp. 2360–2379. ISSN: 0022-5096. DOI: https://doi.org/10.1016/j.jmps.2013.05.001.

[10] Thanh Tung Nguyen, Julien Réthoré, and Marie-Christine Baietto. "Phase field modelling of anisotropic crack propagation". In: *European Journal of Mechanics - A/Solids* 65 (2017), pp. 279–288. ISSN: 0997-7538. DOI: https://doi.org/10.1016/j.euromechsol.2017.05.002.

[11] Christian Miehe and Steffen Mauthe. "Phase field modeling of fracture in multi-physics problems. Part III. Crack driving forces in hydro-poro-elasticity and hydraulic fracturing of fluid-saturated porous media". In: *Computer Methods in Applied Mechanics and Engineering* 304 (2016), pp. 619–655. ISSN: 00457825. DOI: 10.1016/j.cma.2015.09.021.

[12] T. Cajuhi, L. Sanavia, and L. De Lorenzis. "Phase-field modeling of fracture in variably saturated porous media". In: *Computational Mechanics* 61.3 (2018), pp. 299–318. ISSN: 01787675. DOI: 10.1007/s00466-017-1459-3.

[13] A. Mikelić, M. F. Wheeler, and T. Wick. *Phase-field modeling through iterative splitting of hydraulic fractures in a poroelastic medium*. Vol. 10. Springer International Publishing, 2019. ISBN: 0123456789. DOI: 10.1007/s13137-019-0113-y.

[14] Emilio Martínez-Pañeda, Alireza Golahmar, and Christian F. Niordson. "A phase field formulation for hydrogen assisted cracking". In: *Computer Methods in Applied Mechanics and Engineering* 342 (2018), pp. 742–761. ISSN: 00457825. DOI: 10.1016/j.cma.2018.07.021.

[15] Chuanjie Cui, Rujin Ma, and Emilio Martínez-Pañeda. "A phase field formulation for dissolution-driven stress corrosion cracking". In: *Journal of the Mechanics and Physics of Solids* 147 (2021), p. 104254. ISSN: 0022-5096. DOI: https://doi.org/10.1016/j.jmps.2020.104254.

[16] Marlini Simoes and Emilio Martínez-Pañeda. "Phase field modelling of fracture and fatigue in Shape Memory Alloys". In: *Computer Methods in Applied Mechanics and Engineering* 373 (2021), p. 113504. ISSN: 0045-7825. DOI: https://doi.org/10.1016/j.cma.2020.113504. URL: https://www.sciencedirect.com/science/article/pii/S0045782520306897.

[17] G. Kikis et al. "Phase-field model of brittle fracture in Reissner–Mindlin plates and shells". In: *Computer Methods in Applied Mechanics and Engineering* 373 (2021), p. 113490. ISSN: 0045-7825. DOI: https://doi.org/10.1016/j.cma.2020.113490. URL: https://www.sciencedirect.com/science/article/pii/S0045782520306757.

[18] R.U. Patil, B.K. Mishra, and I.V. Singh. "An adaptive multiscale phase field method for brittle fracture". In: *Computer Methods in Applied Mechanics and Engineering* 329 (Feb. 2018), pp. 254–288. ISSN: 00457825. DOI: 10.1016/j.cma.2017.09.021.

[19] R.U. Patil et al. "A new multiscale phase field method to simulate failure in composites". In: *Advances in Engineering Software* 126 (2018), pp. 9–33. ISSN: 0965-9978. DOI: https://doi.org/10.1016/j.advengsoft.2018.08.010.

[20] R.U. Patil, B.K. Mishra, and I.V. Singh. "A multiscale framework based on phase field method and XFEM to simulate fracture in highly heterogeneous materials". In: *Theoretical and Applied Fracture Mechanics* 100 (2019), pp. 390–415. ISSN: 0167-8442. DOI: https://doi.org/10.1016/j.tafmec.2019.02.002.

[21] F. Fantoni et al. "A phase field approach for damage propagation in periodic microstructured materials". In: *International Journal of Fracture* (2019). ISSN: 1573-2673. DOI: 10.1007/s10704-019-00400-x.

[22] Ritukesh Bharali, Fredrik Larsson, and Ralf Jänicke. "Computational homogenisation of phase-field fracture". In: *European Journal of Mechanics - A/Solids* 88 (2021), p. 104247. ISSN: 0997-7538. DOI: https://doi.org/10.1016/j.euromechsol.2021.104247.

[23] Marreddy Ambati, Tymofiy Gerasimov, and Laura De Lorenzis. "A review on phase-field models of brittle fracture and a new fast hybrid formulation". In: *Computational Mechanics* 55.2 (2014), pp. 383–405. ISSN: 01787675. DOI: 10.1007/s00466-014-1109-y.

[24] Jian-Ying Wu et al. "Chapter One - Phase-field modeling of fracture". In: ed. by Stéphane P.A. Bordas and Daniel S. Balint. Vol. 53. Advances in Applied Mechanics. Elsevier, 2020, pp. 1–183. DOI: https://doi.org/10.1016/bs.aams.2019.08.001. URL: https://www.sciencedirect.com/science/article/pii/S0065215619300134.

[25] Laura De Lorenzis and Tymofiy Gerasimov. "Numerical implementation of phase-field models of brittle fracture". In: *Modeling in Engineering Using Innovative Numerical Methods for Solids and Fluids*. Springer, 2020, pp. 75–101.

[26] Timo Heister, Mary F. Wheeler, and Thomas Wick. "A primal-dual active set method and predictor-corrector mesh adaptivity for computing fracture propagation using a phase-field approach". In: *Computer Methods in Applied Mechanics and Engineering* (2015). ISSN: 00457825. DOI: 10.1016/j.cma.2015.03.009.

[27] T. Gerasimov and L. De Lorenzis. "A line search assisted monolithic approach for phase-field computing of brittle fracture". In: *Computer Methods in Applied Mechanics and Engineering* 312 (Dec. 2016), pp. 276–303. ISSN: 00457825. DOI: 10.1016/j.cma.2015.12.017.

[28] Thomas Wick. "An Error-Oriented Newton/Inexact Augmented Lagrangian Approach for Fully Monolithic Phase-Field Fracture Propagation". In: *SIAM Journal on Scientific Computing* 39.4 (2017), B589–B617. ISSN: 1064-8275. DOI: 10.1137/16m1063873.

[29] Thomas Wick. "Modified Newton methods for solving fully monolithic phase-field quasi-static brittle fracture propagation". In: *Computer Methods in Applied Mechanics and Engineering* (2017). ISSN: 00457825. DOI: 10.1016/j.cma.2017.07.026.

[30] Alena Kopaničáková and Rolf Krause. "A recursive multilevel trust region method with application to fully monolithic phase-field models of brittle fracture". In: *Computer Methods in Applied Mechanics and Engineering* 360 (2020), p. 112720. ISSN: 0045-7825. DOI: https://doi.org/10.1016/j.cma.2019.112720. URL: https://www.sciencedirect.com/science/article/pii/S0045782519306085.

[31] B. Bourdin. "Numerical implementation of the variational formulation for quasi-static brittle fracture". In: *Interfaces and Free Boundaries* 9 (2007), pp. 411–430. DOI: 10.4171/IFB/171.

[32] Siobhan Burke, Christoph Ortner, and Endre Süli. "An Adaptive Finite Element Approximation of a Variational Model of Brittle Fracture". In: *SIAM Journal on Numerical Analysis* 48.3 (2010), pp. 980–1012. DOI: 10.1137/080741033.

[33] Christian Miehe, Martina Hofacker, and Fabian Welschinger. "A phase field model for rate-independent crack propagation: Robust algorithmic implementation based on operator splits". In: *Computer Methods in Applied Mechanics and Engineering* 199.45-48 (2010), pp. 2765–2778. ISSN: 00457825. DOI: 10.1016/j.cma.2010.04.011. URL: http://dx.doi.org/10.1016/j.cma.2010.04.011.

[34] FA Valentine. "The problem of Lagrange with differentiable inequality as added side conditions. 407–448". In: *Contributions to the Calculus of Variations* 37 (1933).

[35] D P Bertsekas. “Nonlinear Programming”. In: *Journal of the Operational Research Society* 48.3 (1997), pp. 334–334. DOI: 10.1057/palgrave.jors.2600425.

[36] Siobhan Burke, Christoph Ortner, and Endre Süli. “An adaptive finite element approximation of a variational model of brittle fracture”. In: *SIAM Journal on Numerical Analysis* 48.3 (2010), pp. 980–1012.

[37] Marco Artina et al. “Anisotropic mesh adaptation for crack detection in brittle materials”. In: *SIAM Journal on Scientific Computing* 37.4 (2015), B633–B659.

[38] Thomas Wick. “Goal functional evaluations for phase-field fracture using PU-based DWR mesh adaptivity”. In: *Computational Mechanics* 57.6 (2016), pp. 1017–1035.

[39] D. W. Kelly et al. “A posteriori error analysis and adaptive processes in the finite element method: Part I—error analysis”. In: *International Journal for Numerical Methods in Engineering* 19.11 (1983), pp. 1593–1619. DOI: https://doi.org/10.1002/nme.1620191103.

[40] S. Nagaraja et al. “Phase-field modeling of brittle fracture with multi-level hp-FEM and the finite cell method”. In: *Computational Mechanics* 63.6 (June 2019), pp. 1283–1300. ISSN: 1432-0924. DOI: 10.1007/s00466-018-1649-7.

[41] M. Hintermüller, K. Ito, and K. Kunisch. “The Primal-Dual Active Set Strategy as a Semismooth Newton Method”. In: *SIAM Journal on Optimization* 13.3 (2002), pp. 865–888. DOI: 10.1137/S1052623401383558.

[42] R. A. Tapia. “A stable approach to Newton’s method for general mathematical programming problems inRn”. In: *Journal of Optimization Theory and Applications* 14.5 (Nov. 1974), pp. 453–476. ISSN: 1573-2878. DOI: 10.1007/BF00932842. URL: https://doi.org/10.1007/BF00932842.

[43] Yousef Navidtehrani, Covadonga Betegón, and Emilio Martínez-Pañeda. “A Unified Abaqus Implementation of the Phase Field Fracture Method Using Only a User Material Subroutine”. In: *Materials* 14.8 (2021). ISSN: 1996-1944. DOI: 10.3390/ma14081913. URL: https://www.mdpi.com/1996-1944/14/8/1913.

[44] Donald G Anderson. “Iterative procedures for nonlinear integral equations”. In: *Journal of the ACM (JACM)* 12.4 (1965), pp. 547–560.

[45] Dan Givoli, Ritukesh Bharali, and Lambertus J Sluys. “LATIN: A new view and an extension to wave propagation in nonlinear media”. In: *International Journal for Numerical Methods in Engineering* 112.2 (2017), pp. 125–156.

[46] Ritukesh Bharali. “An Adaptive Generic Incremental LATIN method”. MA thesis. Building 23, Stevinweg 1, 2628 CN, Delft, The Netherlands: Technische Universiteit Delft, 2017.

PAPER C

Computational homogenisation of phase-field fracture

Ritukesh Bharali, Fredrik Larsson, Ralf Jänicke

Published in European Journal of Mechanics - A/Solids,
vol. 88, July–August 2021.
DOI: 10.1016/j.euromechsol.2021.104247

European Journal of Mechanics / A Solids 88 (2021) 104247

Contents lists available at ScienceDirect

European Journal of Mechanics / A Solids

journal homepage: www.elsevier.com/locate/ejmsol

Computational homogenisation of phase-field fracture

Ritukesh Bharali [a,*], Fredrik Larsson [a], Ralf Jänicke [b]

[a] Chalmers University of Technology, 412 96, Gothenburg, Sweden
[b] Technische Universität Braunschweig, 38106, Braunschweig, Germany

ARTICLE INFO

Keywords:
Phase-field fracture
Homogenisation
Macro-homogeneity
Multi-scale

ABSTRACT

In this manuscript, the computational homogenisation of phase-field fractures is addressed. To this end, a variationally consistent two-scale phase-field fracture framework is developed, which formulates the coupled momentum balance and phase-field evolution equations at the macro-scale as well as at the Representative Volume Element (RVE[1]) scale. The phase-field variable represent fractures at the RVE scale, however, at the macro-scale, it is treated as an auxiliary variable. The latter interpretation follows from the homogenisation of the phase-field through volume or a surface-average. For either homogenisation choices, the set of macro-scale and sub-scale equations, and the pertinent macro-homogeneity satisfying boundary conditions are established. As a special case, the concept of selective homogenisation is introduced, where the phase-field is chosen to live only in the RVE domain, thereby eliminating the macro-scale phase-field evolution equation. Numerical experiments demonstrate the local macro-scale material behaviour of the selective homogenisation based two-scale phase-field fracture model, while its non-selective counterpart yields a non-local macro-scale material behaviour.

1. Introduction

An in-depth understanding of fracture (initiation and propagation) processes in materials is essential for the prediction of fracture-induced failure in engineering structures. To that end, the past century has seen a thrust towards developing theoretical approaches to help gain a deeper understanding of fracture processes. The earliest theoretical approach, developed by Griffith and Taylor (1921) reasoned that fracture propagation occurs if the energy release rate reaches a critical value. Much later, in an alternate approach Irwin (1957) postulated a fracture propagation criterion based on stress-intensity factors. However, both theories were unable to predict the initiation of fracture and explain topologically complex (branching, merging, kinking and curvilinear) fractures. However, these limitations were eliminated with a variational model based on energy minimisation of the fractured continuum (Francfort and Marigo, 1998). The numerical implementation of the same was proposed in Bourdin et al. (2000), motivated by the Ambrosio–Tortorelli regularisation of the Mumford–Shah potential (Mumford and Shah, 1989). An auxiliary variable, the phase-field was introduced that interpolates between the intact and the broken material states. This lends the name phase-field fracture model (PFFM).

In the past decade, there has been an increased interest in PFFM, primarily due to its ability to predict fracture initiation and handle topologically complex fractures. In Miehe et al. (2010b), a thermodynamically consistent phase-field model for brittle fracture was developed adopting an energetic crack driving force definition. The work was later extended to include generalised stress-based crack driving criteria and applied to thermo-mechanical problem at large strains (Miehe et al., 2015b). Subsequent studies included ductile failure (Miehe et al., 2015a, 2016; Ambati et al., 2015; Alessi et al., 2015), fracture due to bending in thin films (Mesgarnejad et al., 2013), anisotropic fracture (Nguyen et al., 2017), fracture in fully/partially saturated porous media (Wilson and Landis, 2016; Miehe and Mauthe, 2016; Lee et al., 2017; Zhou et al., 2018; Cajuhi et al., 2018; Mikelić et al., 2019), hydrogen assisted cracking (Martínez-Pañeda et al., 2018), to cite a few.

Additionally, there have been studies directed at formulating robust and efficient numerical solution techniques for the PFFM. This is because the underlying energy functional is non-convex, thereby leading to the poor performance of the fully monolithic Newton solver. In order to improve the performance of the monolithic Newton solver, Gerasimov and De Lorenzis (2016) developed a novel line-search technique that included a negative search direction. An alternative robust formulation was proposed in Heister et al. (2015), aided with a linear extrapolation of the phase-field in (pseudo) time and the semi-smooth Newton method (Hintermüller et al., 2002) for crack irreversibility.

* Corresponding author.
E-mail addresses: ritukesh.bharali@chalmers.se (R. Bharali), fredrik.larsson@chalmers.se (F. Larsson), r.janicke@tu-braunschweig.de (R. Jänicke).

[1] The term 'RVE' is used interchangeably with sub-scale domain or microstructure, in this manuscript.

https://doi.org/10.1016/j.euromechsol.2021.104247
Received 17 June 2020; Received in revised form 29 December 2020; Accepted 7 February 2021
Available online 16 February 2021

Some other numerical techniques adopted for the PFFM include the use of the dissipation-based arc-length method (May et al., 2015), modified Newton method (Wick, 2017b) and error-oriented Newton method (Wick, 2017a) . While most studies are focused on quasi-static analyses, Borden et al. (2012) adopted a monolithic Newton solver for dynamic (brittle) fracture simulations. Therein, it was reported that the physically limited crack tip velocity prevents full fracture within a single timestep if the timestep sizes are chosen adequately. As an alternative to monolithic solvers, a staggered (alternate minimisation) solver was suggested in Bourdin (2007) in conjunction with 'crack-set' irreversibility. Later, in Miehe et al. (2010a), the 'crack-set' based irreversibility was replaced by an implicit 'history variable' based irreversibility. Although the staggered solver is numerically robust owing to the convexity of the energy functional w.r.t displacement and phase-field separately, it is computationally expensive compared to monolithic solvers (Gerasimov and De Lorenzis, 2016). Yet another aspect connected to computational efficiency is the adaptive refinement of the mesh. In particular, the phase-field fracture model requires extremely fine meshes in the phase-field transition zone. In this regard, fixed uniform meshes could be used when the fracture path is not known in advance. However, if it is known, certain sub-domains of the mesh could be pre-refined. More elegant ways in the form of error-oriented mesh refinement (Burke et al., 2010; Wick, 2016), refinement based on the phase-field reaching a certain threshold (Heister et al., 2015) and local increase of the tensile energy (Klinsmann et al., 2015), and multi-level *hp* refinement using the finite cell method (Nagaraja et al., 2019) exists in the phase-field fracture literature. Despite these advancements, the development of robust and computationally efficient solution and meshing techniques are still topics of active research.

So far, the studies pertaining to the PFFM are limited to a single scale. In the context of multi-scale approach, the PFFM has been used in conjunction with the Multi-scale Finite Element Method (MsFEM) to simulate brittle fracture (Patil et al., 2018a), failure in composites (Patil et al., 2018b) and fractures in highly heterogeneous materials (matrix with voids and/or inclusions) (Patil et al., 2019). The MsFEM assumes a fine-scale domain embedded within a coarse macro-element. The fine-scale features (voids, cracks and other heterogeneities) are then captured using multi-scale basis functions, computed numerically on-the-fly. However, these fine-scale features if several magnitudes lower in size than the domain itself renders the fine-scale problem expensive. A cheaper alternative can be formulated on assuming separation of scales which allows a comparatively smaller fine-scale (referred to as sub-scale in this manuscript) domain in a computational homogenisation framework. The separation of scales was assumed in a study involving porous media (He et al., 2020), using the Finite Element-Heterogeneous Multi-scale Method (FE-HMM). However, only the elastic tensor was 'homogenised' owing to the presence of microstructural pores, and the phase-field evolution equation was not solved at the micro-structural level. This indicates that the microstructural fractures/cracks were not accounted for. In yet another study (Fantoni et al., 2019), asymptotic homogenisation of the microstructures were performed offline for varying phase-field values. The homogenised constitutive tensor was then obtained using a closed-form expression based on two-scale asymptotic homogenisation and interpolation of the phase-field variable. Such a method, however, requires that the offline computations include all possible failure topologies of the microstructure. This could be a challenging task in the case of topologically complex microstructural features. An elegant alternative would be to introduce a framework, wherein the coupled momentum balance and phase-field evolution equations are established the macro-scale as well as at the microstructural (RVE) scale, along with adequate computational homogenisation technique. However, to the best of the authors' knowledge, such a framework has not been developed yet.

In this manuscript, a two-scale phase-field fracture framework is developed using the Variationally Consistent homogenisation (VCH) framework (Larsson et al., 2010b) and the relevant computational homogenisation aspects are discussed. The VCH framework provides an elegant procedure to derive pertinent scales for a hierarchical multi-scale problem, from its fully resolved fine-scale problem[2]. The critical ingredient of the method lies in the conjunction of the Variational MultiScale method (Hughes et al., 1998) and the separation of scales adopted through classical (first-order) homogenisation. The Hill–Mandel macro-homogeneity conditions (Hill, 1963, 1984; Nemat-Nasser, 1999) are fulfilled through equivalent Variationally Consistent Macro-homogeneity Conditions. The advantages of the VCH framework lies in its applicability in the homogenisation for a general class of problems, and in establishing scale-bridging strategies. The VCH framework has been used to derive multi-scale models in porous media (Larsson et al., 2010a; Sandstrom and Larsson, 2013; Ohman et al., 2013; Jänicke et al., 2020), gradient-enhanced visco-plastic dissipative materials (Runesson et al., 2017), and computational homogenisation of micro-fractured continua using the eXtended Finite Element Method (XFEM) (Svenning et al., 2016b, 2017), to cite a few. However, the VCH framework has not been explored yet in the context of smeared-type fracture or damage models.

In the view of existing literature on the phase-field fracture model and the VCH framework, discussed in the preceding paragraphs, a two-scale phase-field fracture framework addresses the two-fold research gap, viz., (i.) the lack of a multi-scale framework wherein the coupled momentum balance and phase-field are formulated at the macro-scale and RVE scale, and (ii.) extending the VCH framework to smeared-type (phase-field) fracture model. Moreover, the two-scale phase-field fracture framework is generic in the sense that it allows different choices pertaining to computational homogenisation of the microstructural quantities. This aspect is explored at length in this manuscript, with (i.) volume and surface-average based homogenisation measures, and (ii.) selective homogenisation in the context of the phase-field variable. In particular, the novel contribution of this manuscript are:

- the formulation of a variationally consistent two-scale phase-field fracture framework, that allows different models based on computational homogenisation choices;
- establishing the space-variational (Euler–Lagrange) equations and pertinent homogenised dual quantities for three different two-scale phase-field fracture models, derived adopting volume-average, surface-average and selection homogenisation measures.

The focus of this manuscript lies in the computational homogenisation aspects of the different two-scale phase-field fracture models and not in the representativeness of real random media. Therefore, the RVEs used throughout this manuscript are artificially created and designed to demonstrate the underlying micro-structural features. However, in the case of real random media, the existence and size determination of RVEs (or Statistical Volume Elements) requires careful investigation. For more on this aspect, the reader is referred to Ostoja-Starzewski (2006) and Gitman et al. (2007).

This manuscript is organised as follows: In Section 2, the reader is introduced to the Phase-Field Fracture Model (PFFM), its underlying energy functional and the set of coupled space-variational (Euler–Lagrange) equations. The two-scale phase-field fracture framework is then developed in Section 3. Within this framework, a family of two-scale phase-field fracture models are developed, based on different homogenisation choices. Thereafter, in Section 4, a numerical investigation is carried out on the artificially created RVEs in the context of constraints (Dirichlet, Neumann and Strongly Periodic boundary conditions, and domain or surface constraints) and pertinent upscaled (homogenised) quantities for the different two-scale phase-field fracture models. A model multi-scale FE^2 problem is presented in Section 5 and results from the simulations are discussed. Finally, Section 6 lays down the concluding remarks of this manuscript.

[2] A 'fine-scale problem' resolves all microstructural features and requires Direct Numerical Simulation.

Notation

The following notations are strictly adhered to in this manuscript:

- *Zero-order tensors (scalars) are represented using italic letters, first-order and higher order tensors are represented with bold-faced letters.*
- *A function f with its arguments x, y is written in the form $f(x, y)$, whereas a variable g with operational dependencies p, q is written as $g[p, q]$.*
- *The volume and surface-average of a quantity, say p, are denoted as $\langle p\rangle_{\square}$ and $\langle\langle p\rangle\rangle_{\square}$. They are defined later in the text, in Section 3.1.*
- *The Macaulay operator on a variable p is defined as $\langle p\rangle_{\pm} = \frac{1}{2}(p \pm |p|)$.*

2. Phase field fracture model

In this section, the reader is introduced to the Phase Field Fracture Model, starting with the Francfort–Marigo energy functional (Francfort and Marigo, 1998), its phase-field regularisation and minimisation. All formulations and derivations are within the small strain continuum framework.

2.1. The energy functional

Let $\Omega \in \mathbb{R}^{\dim}$ ($\dim = 2, 3$) be the domain occupied by the fracturing solid as shown in Fig. 1a. Its boundary Γ is decomposed into a Dirichlet boundary $\Gamma_{\mathrm{D}}^{(u)}$ and a Neumann boundary $\Gamma_{\mathrm{N}}^{(u)}$, such that $\Gamma = \Gamma_{\mathrm{D}}^{(u)} \cup \Gamma_{\mathrm{N}}^{(u)}$ and $\Gamma_{\mathrm{D}}^{(u)} \cap \Gamma_{\mathrm{N}}^{(u)} = \emptyset$. Furthermore, $\mathcal{C}$ denotes the crack set (a single sharp crack in Fig. 1a) in the solid.

The energy of a fracturing elastic solid is described by the Francfort–Marigo functional in Francfort and Marigo (1998) as,

$$E = \int_{\Omega} \Psi(\boldsymbol{\epsilon}[\mathbf{u}])\,\mathrm{d}\Omega - \int_{\Gamma_{\mathrm{N}}^{(u)}} \mathbf{t}^{\mathrm{p}} \cdot \mathbf{u}\,\mathrm{d}\Gamma + \int_{\mathcal{C}} G_c\,\mathrm{d}\Gamma, \tag{1}$$

where $\Psi(\boldsymbol{\epsilon}[\mathbf{u}])$ is the elastic strain energy density function, $\mathbf{t}^{\mathrm{p}}$ denotes the tractions on $\Gamma_{\mathrm{N}}^{(u)}$, and last integral pertains to fracture energy, where G_c is the Griffith fracture toughness. The elastic strain energy density function is defined as

$$\Psi(\boldsymbol{\epsilon}[\mathbf{u}]) = \frac{1}{2}\lambda(\mathbf{I} : \boldsymbol{\epsilon}[\mathbf{u}])^2 + \mu(\boldsymbol{\epsilon} : \boldsymbol{\epsilon}), \tag{2}$$

where λ and μ are the Lame parameters, $\mathbf{I}$ is a second-order identity tensor, $\mathbf{u} : \Omega \to \mathbb{R}^n$ is the displacement, and $\boldsymbol{\epsilon}$ is the symmetric strain tensor given by,

$$\boldsymbol{\epsilon}[\mathbf{u}] = (\mathbf{u} \otimes \boldsymbol{\nabla})^{\mathrm{sym}}. \tag{3}$$

In Fig. 1b, the sharp crack topology is regularised by introducing a diffusive (smeared) fracture zone of width $l > 0$, and an additional scalar auxiliary variable φ. The fracture surface $\mathcal{C}$ is now replaced by the continuous variable $\varphi : \Omega \to [0, 1]$, where 0 corresponds to the intact state and 1 indicates a fully formed crack. Accordingly, the integrand in (1) is replaced by an elliptic Ambrosio–Tortorelli function, $G_c\left(\frac{1}{2l}\varphi^2 + \frac{l}{2}|\boldsymbol{\nabla}\varphi|^2\right)$, cf. Bourdin et al. (2000). The energy functional for the fracturing solid now attains the form

$$E = \int_{\Omega} \Psi(\boldsymbol{\epsilon}[\mathbf{u}])\,\mathrm{d}\Omega - \int_{\Gamma_{\mathrm{N}}^{(u)}} \mathbf{t}^{\mathrm{p}} \cdot \mathbf{u}\,\mathrm{d}\Gamma + \int_{\Omega} G_c\left(\frac{1}{2l}\varphi^2 + \frac{l}{2}|\boldsymbol{\nabla}\varphi|^2\right)\mathrm{d}\Omega. \tag{4}$$

In the event of a fracture occurring in a solid, the strain energy of the solid is expected to decrease. Additionally, in this manuscript, it is assumed that fractures occur only under tensile loading. Both these requirements are met upon introducing an additive split of the elastic strain energy density Ψ into a tensile part Ψ^+ and a compression part Ψ^-, such that a monotonically decreasing degradation function $g(\varphi)+\kappa$ acts only on Ψ^+ (Miehe et al., 2010a). This results in the modified energy functional

$$E = \int_{\Omega} (g(\varphi) + \kappa)\,\Psi^+(\boldsymbol{\epsilon}[\mathbf{u}])\,\mathrm{d}\Omega + \int_{\Omega} \Psi^-(\boldsymbol{\epsilon}[\mathbf{u}])\,\mathrm{d}\Omega - \int_{\Gamma_{\mathrm{N}}^{(u)}} \mathbf{t}^{\mathrm{p}} \cdot \mathbf{u}\,\mathrm{d}\Gamma + \int_{\Omega} G_c\left(\frac{1}{2l}\varphi^2 + \frac{l}{2}|\boldsymbol{\nabla}\varphi|^2\right)\mathrm{d}\Omega, \tag{5}$$

where $g(\varphi) = (1-\varphi)^2$ and $\kappa = 1e-10$ (a small term that prevents numerical singularity[3]). The tensile–compressive split of the strain energy density are given by

$$\Psi^{\pm}(\boldsymbol{\epsilon}[\mathbf{u}]) = \frac{1}{2}\lambda\langle(\mathbf{I} : \boldsymbol{\epsilon}[\mathbf{u}])\rangle_{\pm}^2 + \mu\boldsymbol{\epsilon}^{\pm}[\mathbf{u}] : \boldsymbol{\epsilon}^{\pm}[\mathbf{u}]. \tag{6}$$

In the above relation, $\boldsymbol{\epsilon}^{\pm}[\mathbf{u}]$ is defined as

$$\boldsymbol{\epsilon}^{\pm}[\mathbf{u}] = \sum_{i=1}^{\dim} \langle\epsilon_i\rangle_{\pm}\mathbf{p}_i \otimes \mathbf{p}_i \tag{7}$$

where ϵ_i represents the ith eigenvalue of the strain, and $\mathbf{p}_i$ is its corresponding normalised eigenvector.

The subsequent sections would involve the space-variational (Euler-Lagrange) equations pertaining to the energy functional in (5). In this context, the Cauchy tensile and compressive stresses are defined as

$$\boldsymbol{\sigma}^{\pm} = \frac{\partial\Psi^{\pm}}{\partial\boldsymbol{\epsilon}} = \lambda\langle(\mathbf{I} : \boldsymbol{\epsilon}[\mathbf{u}])\rangle_{\pm}\mathbf{I} + 2\mu\boldsymbol{\epsilon}^{\pm}[\mathbf{u}]. \tag{8}$$

2.2. The space-variational formulation

In order to predict the fracture path in a solid occupying the domain Ω, the energy functional in (5) should be minimised w.r.t. the solution variables, vector-valued displacement $\mathbf{u}$ and scalar-valued phase-field φ. This has to be further augmented with an additional requirement of fracture irreversibility (no healing of fractures is permitted) and pertinent Dirichlet and/or Neumann boundary conditions. This results in a constrained minimisation problem that reads:

Problem Statement 1. Find $\mathbf{u}$ and φ for all times $t \in [0, T]$ such that,

$$min_{\mathbf{u}(t),\varphi(t)}(E) \quad \text{and.} \quad \partial_t\varphi \geq 0. \tag{9}$$

Here, $[0, T]$ refers to the time interval of interest. In this manuscript, the time t refers to a loading step, instead of the *actual* time (quasi-static loading). The system in (9) is augmented by relevant time-dependent boundary conditions of Dirichlet type $\mathbf{u}^{\mathrm{p}}$ on $\Gamma_{\mathrm{D}}^{(u)}$ and φ^{p} on $\Gamma_{\mathrm{D}}^{(\varphi)}$, and/or Neumann type $\mathbf{t}^{\mathrm{p}}$ on $\Gamma_{\mathrm{N}}^{(u)}$ and q^{p} on $\Gamma_{\mathrm{N}}^{(\varphi)}$. Furthermore, the boundary Γ is decomposed as $\Gamma = \Gamma_{\mathrm{D}}^{(u)} \cup \Gamma_{\mathrm{N}}^{(u)}$, $\Gamma_{\mathrm{D}}^{(u)} \cap \Gamma_{\mathrm{N}}^{(u)} = \emptyset$ and $\Gamma = \Gamma_{\mathrm{D}}^{(\varphi)} \cup \Gamma_{\mathrm{N}}^{(\varphi)}$, $\Gamma_{\mathrm{D}}^{(\varphi)} \cap \Gamma_{\mathrm{N}}^{(\varphi)} = \emptyset$ respectively. ■

Note that incorporating the possibility to prescribe the flux q^{p} on $\Gamma_{\mathrm{N}}^{(\varphi)}$ does not lead to loss of generality of the original problem (4). The space-variational (or the Euler–Lagrange) equations are derived by taking the first variation of the energy functional w.r.t. its solution variables $\mathbf{u}$ and φ. This results in the following:

Problem Statement 2. Find $(\mathbf{u}, \varphi) \in \mathbb{U} \times \mathbb{P}$ with

$$\begin{aligned} &\int_{\Omega} \left((1-\varphi)^2 + \kappa\right)\boldsymbol{\sigma}^+ : \boldsymbol{\epsilon}[\delta\mathbf{u}]\,\mathrm{d}\Omega \\ &\qquad + \int_{\Omega} \boldsymbol{\sigma}^- : \boldsymbol{\epsilon}[\delta\mathbf{u}]\,\mathrm{d}\Omega \\ &\qquad - \int_{\Gamma_{\mathrm{N}}^{(u)}} \mathbf{t}^{\mathrm{p}} \cdot \delta\mathbf{u}\,\mathrm{d}\Gamma = 0 \qquad \forall\,\delta\mathbf{u} \in \mathbb{U}^0, \end{aligned} \tag{10a}$$

$$\begin{aligned} &\int_{\Omega} G_c\left(\frac{1}{l}\varphi\,(\hat{\varphi} - \varphi) + l\,\boldsymbol{\nabla}\varphi \cdot \boldsymbol{\nabla}(\hat{\varphi} - \varphi)\right)\mathrm{d}\Omega \\ &\qquad - \int_{\Omega} (1-\varphi)\boldsymbol{\sigma}^+ : \boldsymbol{\epsilon}[\mathbf{u}](\hat{\varphi} - \varphi)\,\mathrm{d}\Omega \end{aligned}$$

[3] The use of κ is debated in the phase-field fracture literature. For dynamic simulations, Borden et al. (2012) showed that κ could be set to zero. However, in Miehe et al. (2010b), the authors have advocated the use of κ for well-posedness of partly broken systems. This manuscript follows the latter approach.

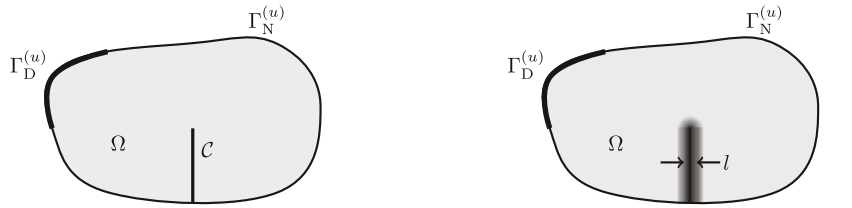

(a) sharp crack (b) diffused (smeared) crack

Fig. 1. A solid $\Omega \in \mathbb{R}^2$ embedded with (a). sharp crack $\mathcal{C}$ and (b). diffused (smeared) crack. Dirichlet and Neumann boundaries are indicated with $\Gamma_{\mathrm{D}}^{(u)}$ and $\Gamma_{\mathrm{N}}^{(u)}$ respectively.

$$-\int_{\Gamma_{\mathrm{N}}^{(\varphi)}} q^{\mathrm{p}}(\hat{\varphi}-\varphi)\,\mathrm{d}\Gamma \geq 0 \qquad \forall\, \hat{\varphi} \in \mathbb{P} \tag{10b}$$

using pertinent time-dependent Dirichlet boundary conditions $\mathbf{u}^p$ on $\Gamma_{\mathrm{D}}^{(u)}$ and φ^p on $\Gamma_{\mathrm{D}}^{(\varphi)}$, and/or Neumann boundary conditions

$$\mathbf{t} := \left((1-\varphi)^2\boldsymbol{\sigma}^+ + \boldsymbol{\sigma}^-\right)\cdot\mathbf{n} = \mathbf{t}^{\mathrm{p}} \text{ on } \Gamma_{\mathrm{N}}^{(u)}, \tag{11a}$$

$$q := G_c l \boldsymbol{\nabla}\varphi\cdot\mathbf{n} \qquad = q^{\mathrm{p}} \text{ on } \Gamma_{\mathrm{N}}^{(\varphi)}. \tag{11b}$$

The trial and test spaces are defined as

$$\mathbb{U} = \{\mathbf{u} \in [H^1(\Omega)]^{\dim} | \mathbf{u} = \mathbf{u}^{\mathrm{p}} \text{ on } \Gamma_{\mathrm{D}}^{(u)}\}, \tag{12a}$$

$$\mathbb{P} = \{\varphi \in [H^1(\Omega)]^1 | \varphi \geq {}^n\varphi | \varphi = \varphi^{\mathrm{p}} \text{ on } \Gamma_{\mathrm{D}}^{(\varphi)}\}, \tag{12b}$$

$$\mathbb{U}^0 = \{\mathbf{u} \in [H^1(\Omega)]^{\dim} | \mathbf{u} = \mathbf{0} \text{ on } \Gamma_{\mathrm{D}}^{(u)}\}. \tag{12c}$$

The left superscript n in (12b) refer to the previous step in (pseudo) time. For brevity, the superscript $(n+1)$ over the variables and solution fields in the current step in time is avoided. ■

Note that the variational inequality (10b) in Problem Statement 2 stems from the fracture irreversibility requirement $\varphi \geq \varphi^n$. The treatment of the fracture irreversibility is a widely discussed topic when it comes to developing computationally efficient and robust equality-based solution techniques. In this context, Gerasimov and De Lorenzis (2016) suggested a penalisation approach to (10b). Adopting an alternative approach, Heister et al. (2015) proposed the use of a semi-smooth Newton method developed by Hintermüller et al. (2002). Yet another alternative was suggested in Wick (2017a), where an augmented Lagrangian method was developed using the Moreau–Yoshida regularisation. Note that all of the aforementioned literature advocated the use of a monolithic solver. However, in Miehe et al. (2010a), a staggered (alternate minimisation) solution technique is proposed, where the fracture irreversibility is enforced implicitly using a 'history term' $\mathcal{H}$, defined as the maximum accumulated tensile energy over the loading history. Based on the assumption that the fracture is driven by the tensile energy, the authors in Miehe et al. (2010a) postulated that the replacing the tensile energy term $\boldsymbol{\sigma}^+ : \boldsymbol{\epsilon}[\mathbf{u}]$ in (10b) with $\mathcal{H}$ would ensure the fracture irreversibility[4]. Mathematically, $\mathcal{H}$ is given by

$$\mathcal{H} := \max_{[0,t]}\left(\boldsymbol{\sigma}^+ : \boldsymbol{\epsilon}[\mathbf{u}]\right) = \max({}^n\mathcal{H}, \boldsymbol{\sigma}^+ : \boldsymbol{\epsilon}[\mathbf{u}]). \tag{13}$$

where, ${}^n\mathcal{H}$ is the history term computed in the previous step in (pseudo) time. Note that substitution of the history term $\mathcal{H}$ in place of $\boldsymbol{\sigma}^+ : \boldsymbol{\epsilon}[\mathbf{u}]$ in (10b) changes the variational inequality formulation in the Problem Statement 2 to a variational equality formulation that reads:

[4] The enforcement of fracture irreversibility using the history variable remains a questionable assumption despite its popularity within the computational mechanics community, since it introduces a small discrepancy. Please refer to Gerasimov and De Lorenzis (2019) for more on this aspect.

Problem Statement 3. Find $(\mathbf{u}, \varphi) \in \mathbb{U}\times\mathbb{P}$ with

$$\int_\Omega \left((1-\varphi)^2+\kappa\right)\boldsymbol{\sigma}^+ : \boldsymbol{\epsilon}[\delta\mathbf{u}]\,\mathrm{d}\Omega + \int_\Omega \boldsymbol{\sigma}^- : \boldsymbol{\epsilon}[\delta\mathbf{u}]\,\mathrm{d}\Omega - \int_{\Gamma_{\mathrm{N}}^{(u)}} \mathbf{t}^{\mathrm{p}}\cdot\delta\mathbf{u}\,\mathrm{d}\Gamma = 0 \qquad \forall\,\delta\mathbf{u} \in \mathbb{U}^0, \tag{14a}$$

$$\int_\Omega G_c\left(\frac{1}{l}\varphi\,\delta\varphi + l\,\boldsymbol{\nabla}\varphi\cdot\boldsymbol{\nabla}\delta\varphi\right)\mathrm{d}\Omega - \int_\Omega (1-\varphi)\mathcal{H}\delta\varphi\,\mathrm{d}\Omega - \int_{\Gamma_{\mathrm{N}}^{(\varphi)}} q^{\mathrm{p}}\delta\varphi\,\mathrm{d}\Gamma = 0 \qquad \forall\,\delta\varphi \in \mathbb{P}^0 \tag{14b}$$

The trial and test spaces are defined as

$$\mathbb{U} = \{\mathbf{u} \in [H^1(\Omega)]^{\dim} | \mathbf{u} = \mathbf{u}^{\mathrm{p}} \text{ on } \Gamma_{\mathrm{D}}^{(u)}\}, \tag{15a}$$

$$\mathbb{P} = \{\varphi \in [H^1(\Omega)]^1 | \varphi = \varphi^{\mathrm{p}} \text{ on } \Gamma_{\mathrm{D}}^{(\varphi)}\}, \tag{15b}$$

$$\mathbb{U}^0 = \{\mathbf{u} \in [H^1(\Omega)]^{\dim} | \mathbf{u} = \mathbf{0} \text{ on } \Gamma_{\mathrm{D}}^{(u)}\}. \tag{15c}$$

$$\mathbb{P}^0 = \{\varphi \in [H^1(\Omega)]^1 | \varphi = 0 \text{ on } \Gamma_{\mathrm{D}}^{(\varphi)}\}. \tag{15d}$$

The above set of equations are solved using an alternate minimisation algorithm, wherein, (14a) is solved, followed by computation of $\mathcal{H}$ using (13) and solving (14b). This sequence is repeated iteratively until the error measure defined as

$$err = \sqrt{\frac{1}{M}}\sqrt{\sum_{j=1}^{M}\frac{1}{N_j}\sum_{i=1}^{N_j}\left(\frac{|U_{i,j,k+1}-U_{i,j,k}|}{max(|U_{i,j,0}|,1)}\right)^2}, \tag{16}$$

is less than a certain tolerance. In the above relation, U represents a degree of freedom, M is the number of fields (displacement and phase-field in this manuscript), N_j corresponds to the number of degrees of freedom of type j, and the subscript $k+1$ indicates the current iteration. Moreover, the set of equations are augmented by time-dependent Dirichlet and/or Neumann boundary conditions, stated earlier in Problem Statement 2. Also, note that the trial and test spaces for the phase-field in this equality-based formulation differ from variational inequality-based formulation in Problem Statement 2. ■

In order to have a concise representation of the space-variational Eqs. (14a) and (14b), the quantities dual to the strain $\boldsymbol{\epsilon}$, phase-field φ and its gradient $\boldsymbol{\nabla}\varphi$ are defined as,

$$\boldsymbol{\sigma} := \left((1-\varphi)^2+\kappa\right)\boldsymbol{\sigma}^+ + \boldsymbol{\sigma}^-, \tag{17a}$$

$$\boldsymbol{\Phi} := \frac{G_c}{l}\varphi - (1-\varphi)\mathcal{H}, \tag{17b}$$

$$\boldsymbol{\gamma} := G_c l\boldsymbol{\nabla}\varphi, \tag{17c}$$

respectively. This allows re-stating (14a) and (14b) in the compact form

$$\int_\Omega \boldsymbol{\sigma} : \boldsymbol{\epsilon}[\delta\mathbf{u}]\,\mathrm{d}\Omega - \int_{\Gamma_{\mathrm{N}}^{(u)}} \mathbf{t}^{\mathrm{p}}\cdot\delta\mathbf{u}\,\mathrm{d}\Gamma = 0 \qquad \forall\,\delta\mathbf{u} \in \mathbb{U}^0, \tag{18a}$$

$$\int_{\Omega} \boldsymbol{\gamma} \cdot \boldsymbol{\nabla}\delta\varphi \mathrm{d}\Omega + \int_{\Omega} \boldsymbol{\Phi}\delta\varphi \, \mathrm{d}\Omega - \int_{\Gamma_{\mathrm{N}}^{(\varphi)}} q^{\mathrm{p}}\delta\varphi \, \mathrm{d}\Gamma = 0 \qquad \forall\, \delta\varphi \in \mathbb{P}^0. \tag{18b}$$

3. Variationally consistent two-scale phase-field fracture framework

In this section, a two-scale phase-field fracture framework is developed. The framework is developed using the Variationally Consistent homogenisation (VCH) technique proposed in Larsson et al. (2010b). In brief, the VCH technique replaces a fine-scale problem with a macro-scale problem, such that every macro-scale material point is associated with an RVE. This is made possible upon introducing running average approximations of the integrand in the space-variational (Euler–Lagrange) equations, and separation of scales using first-order homogenisation. These aspects are treated in detail in the following sub-sections. Later in the text, the computational homogenisation aspects pertaining to volume or surface-average homogenisation measures as well as selective homogenisation of the phase-field variable are discussed at length. These include establishing prolongation/homogenisation rules and deriving the relevant homogenised dual quantities.

3.1. Running averages

The VCH technique allows a continuous macro-scale problem in the domain Ω, upon introducing a sub-scale RVE $\Omega_{\square}|_{\bar{\mathbf{x}}}$ at each macro-scale material point $\bar{\mathbf{x}} \in \Omega$. Any integrand on Ω is approximated as a quantity averaged over $\Omega_{\square}$. For instance, an integrand f in Ω is obtained through volume-averaging on $\Omega_{\square}$ as

$$f \to \langle f \rangle_{\square}, \tag{19a}$$

$$\langle f \rangle_{\square} := \frac{1}{|\Omega_{\square}|} \int_{\Omega_{\square}} f \, \mathrm{d}\Omega. \tag{19b}$$

Incorporating the volume-averaging definition (19a) and (19b) in (18a) and (18b) yields

$$\int_{\Omega} \langle \boldsymbol{\sigma} : \boldsymbol{\epsilon}[\delta\mathbf{u}] \rangle_{\square} \, \mathrm{d}\Omega - \int_{\Gamma_{\mathrm{N}}^{(u)}} \bar{\mathbf{t}}^{\mathrm{p}} \cdot \delta\mathbf{u} \, \mathrm{d}\Gamma = 0 \qquad \forall\, \delta\mathbf{u} \in \mathbb{U}^0, \tag{20a}$$

$$\int_{\Omega} \langle \boldsymbol{\gamma} \cdot \boldsymbol{\nabla}\delta\varphi \rangle_{\square} \, \mathrm{d}\Omega + \int_{\Omega} \langle \boldsymbol{\Phi}\delta\varphi \rangle_{\square} \, \mathrm{d}\Omega - \int_{\Gamma_{\mathrm{N}}^{(\varphi)}} \bar{q}^{\mathrm{p}}\delta\varphi \, \mathrm{d}\Gamma = 0 \qquad \forall\, \delta\varphi \in \mathbb{P}^0. \tag{20b}$$

Note that each term within the angular brackets $\langle\cdot\rangle_{\square}$ are evaluated on the RVEs, located at macro-scale material points (also referred to as Gauss/integration points in a numerical integration scheme). Furthermore, the prescribed tractions $\bar{\mathbf{t}}^{\mathrm{p}}$ and $\bar{q}^{\mathrm{p}}$ are assumed to be appropriately homogenised.

Remark 1. The VCH framework is generic in the sense that there is no restriction on the definition of the averaging that replaces an integrand. For instance, the integrand, f could also be defined through surface-average approximation over the RVE boundary $\Gamma_{\square}$ as

$$f \to \langle\langle f \rangle\rangle_{\square}, \tag{21a}$$

$$\langle\langle f \rangle\rangle_{\square} := \frac{1}{|\Gamma_{\square}|} \int_{\Gamma_{\square}} f \, \mathrm{d}\Gamma. \tag{21b}$$

Also, the volume-averaging could be carried out over a part of the RVE domain. An example of such an approach is averaging over a failure-zone (Nguyen et al., 2010) (not pursued in this manuscript).

In the next sub-section, the RVE solution fields $\mathbf{u}$, φ and the corresponding test functions $\delta\mathbf{u}$, $\delta\varphi$ would be additively decomposed into a macro-scale contribution and an RVE scale fluctuation adopting the first-order homogenisation technique.

3.2. Scale transition

Scale transition enables to define the RVE solution fields and their corresponding test functions in terms of their macro-scale counterparts (denoted with an overbar in this manuscript). To this end, first, the solution fields $\mathbf{u}$ and φ are additively decomposed into a macro-scale contribution (with a superscript M) and an RVE scale fluctuation (with a superscript s),

$$\mathbf{u} = \mathbf{u}^{\mathrm{M}} + \mathbf{u}^{\mathrm{s}} \tag{22a}$$

$$\varphi = \varphi^{\mathrm{M}} + \varphi^{\mathrm{s}}. \tag{22b}$$

Thereafter, the macro-scale contributions $\mathbf{u}^{\mathrm{M}}$ and φ^{M} are assumed to be linearly varying (first-order) Taylor series expansions about the smooth macro-scale solution fields $\bar{\mathbf{u}}$ and $\bar{\varphi}$ (an approach, consistent with the first-order homogenisation technique). This results in

$$\mathbf{u}^{\mathrm{M}} = \bar{\boldsymbol{\epsilon}} \cdot [\mathbf{x} - \bar{\mathbf{x}}] \text{ and} \tag{23a}$$

$$\varphi^{\mathrm{M}} = \bar{\varphi} + \bar{\boldsymbol{\zeta}} \cdot [\mathbf{x} - \bar{\mathbf{x}}] \qquad \forall\, \mathbf{x} \in \Omega_{\square}, \tag{23b}$$

where $\bar{\boldsymbol{\epsilon}} = \boldsymbol{\epsilon}[\bar{\mathbf{u}}]|_{\bar{\mathbf{x}}}$, $\bar{\varphi} = \bar{\varphi}|_{\bar{\mathbf{x}}}$ and $\bar{\boldsymbol{\zeta}} = \boldsymbol{\nabla}\bar{\varphi}|_{\bar{\mathbf{x}}}$. For the sake of brevity, $|_{\bar{\mathbf{x}}}$ is dropped in the subsequent text of this manuscript. Note that in (23a), the skew-symmetric part of the displacement gradient is excluded due to rigid body invariance. Consequently, the definition of the symmetric strain in (3) is adopted. Furthermore, the test functions $\delta\mathbf{u}$ and $\delta\varphi$ also follow the same additive decomposition and linearly varying macro-scale contributions using first-order Taylor series expansion about their corresponding macro-scale test functions $\delta\bar{\mathbf{u}}$ and $\delta\bar{\varphi}$. This procedure of mapping a macro-scale field to its contribution in the RVE (sub-scale) counterpart is termed as prolongation.

3.3. Macro-scale problem

The macro-scale space-variational (Euler–Lagrange) equations for the phase-field fracture problem is obtained upon testing (20a) and (20b) with $\delta\mathbf{u}^{\mathrm{M}} = \delta\bar{\boldsymbol{\epsilon}} \cdot [\mathbf{x} - \bar{\mathbf{x}}]$ and $\delta\varphi^{\mathrm{M}} = \delta\bar{\varphi} + \delta\bar{\boldsymbol{\zeta}} \cdot [\mathbf{x} - \bar{\mathbf{x}}]$ for each RVE domain $\Omega_{\square}$. Additionally, on the macro-scale Neumann boundaries ($\Gamma_N^{(u)}$ and $\Gamma_N^{(\varphi)}$), it is assumed that $\delta\mathbf{u}^{\mathrm{M}} = \delta\bar{\mathbf{u}}$ and $\delta\varphi^{\mathrm{M}} = \delta\bar{\varphi}$. This results in:

Problem Statement 4. Find $(\bar{\mathbf{u}}, \bar{\varphi}) \in \bar{\mathbb{U}} \times \bar{\mathbb{P}}$ with

$$\int_{\Omega} \bar{\boldsymbol{\sigma}} : \boldsymbol{\epsilon}[\delta\bar{\mathbf{u}}] \, \mathrm{d}\Omega - \int_{\Gamma_{\mathrm{N}}^{(u)}} \bar{\mathbf{t}}^{\mathrm{p}} \cdot \delta\bar{\mathbf{u}} \, \mathrm{d}\Gamma = 0 \qquad \forall \delta\bar{\mathbf{u}} \in \bar{\mathbb{U}}^0, \tag{24a}$$

$$\int_{\Omega} \{\bar{\boldsymbol{\gamma}} + \bar{\mathbf{Q}}\} \cdot \boldsymbol{\nabla}\delta\bar{\varphi} \, \mathrm{d}\Omega + \int_{\Omega} \bar{\boldsymbol{\Phi}} \, \delta\bar{\varphi} \, \mathrm{d}\Omega - \int_{\Gamma_{\mathrm{N}}^{(\varphi)}} \bar{q}^{\mathrm{p}} \, \delta\bar{\varphi} \, \mathrm{d}\Gamma = 0 \qquad \forall\, \delta\bar{\varphi} \in \bar{\mathbb{P}}^0, \tag{24b}$$

where

$$\bar{\boldsymbol{\sigma}} = \langle \boldsymbol{\sigma} \rangle_{\square} := \left\langle \left((1-\varphi)^2 + \kappa\right) \boldsymbol{\sigma}^{+} + \boldsymbol{\sigma}^{-} \right\rangle_{\square}, \tag{25a}$$

$$\bar{\boldsymbol{\gamma}} = \langle \boldsymbol{\gamma} \rangle_{\square} := \langle G_c l \boldsymbol{\nabla}\varphi \rangle_{\square}, \tag{25b}$$

$$\bar{\mathbf{Q}} = \langle \mathbf{Q} \rangle_{\square} := \langle \boldsymbol{\Phi}(\mathbf{x} - \bar{\mathbf{x}}) \rangle_{\square}, \tag{25c}$$

$$\bar{\boldsymbol{\Phi}} = \langle \boldsymbol{\Phi} \rangle_{\square} := \langle \frac{G_c}{l}\varphi - (1-\varphi)\mathcal{H} \rangle_{\square}, \tag{25d}$$

and the trial and test spaces are defined as

$$\bar{\mathbb{U}} := \{\bar{\mathbf{v}} \in [H^1(\Omega)]^{\dim} | \bar{\mathbf{v}} = \bar{\mathbf{u}}^{\mathrm{p}} \text{ on } \Gamma_{\mathrm{D}}^{(u)}\}, \tag{26a}$$

$$\bar{\mathbb{P}} := \{\bar{w} \in [H^1(\Omega)]^1 | \bar{w} = \bar{\varphi}^{\mathrm{p}} \text{ on } \Gamma_{\mathrm{D}}^{(\varphi)}\}, \tag{26b}$$

$$\bar{\mathbb{U}}^0 := \{\bar{\mathbf{v}} \in [H^1(\Omega)]^{\dim} | \bar{\mathbf{v}} = \mathbf{0} \text{ on } \Gamma_{\mathrm{D}}^{(u)}\}, \tag{26c}$$

$$\bar{\mathbb{P}}^0 := \{\bar{w} \in [H^1(\Omega)]^1 | \bar{w} = 0 \text{ on } \Gamma_{\mathrm{D}}^{(\varphi)}\}. \tag{26d}$$

■

Remark 2. In the above formulation, a tacit assumption is made allowing the identification of appropriately homogenised Dirichlet ($\bar{\mathbf{u}}^{\mathrm{p}}$, $\bar{\varphi}^{\mathrm{p}}$) and Neumann ($\bar{\mathbf{t}}^{\mathrm{p}}$, $\bar{q}^{\mathrm{p}}$) values, analogous to those used in Problem Statement 3.

Remark 3. Note that the macro-scale phase-field evolution equation (24b) is different from the original formulation (18b), due to the presence of the additional non-local term $\overline{\mathbf{Q}}$ in the former. This additional term stems from the higher-order term $\boldsymbol{\nabla}\delta\bar{\varphi}$ in the prolongation of $\delta\varphi^{\mathrm{M}}$ (consistent with the first order homogenisation technique).

3.4. RVE problem

The RVE space-variational (Euler–Lagrange) equations are obtained upon localising (20a) and (20b) to each RVE domain $\Omega_{\square}$. To this end, (20a) and (20b) are tested with the fluctuating test functions $\delta\mathbf{u} = \delta\mathbf{u}^{\mathrm{s}}$ and $\delta\varphi = \delta\varphi^{\mathrm{s}}$.

3.4.1. RVE weak/strong periodicity problem

The canonical form of the RVE problem, according to the weak micro-periodicity format (Larsson et al., 2011) is stated as

Problem Statement 5. Find $(\mathbf{u},\, \varphi,\, \lambda^{(u)},\, \lambda^{(\varphi)},\, \bar{\mu}^{(\varphi)}) \in \mathbb{U}_{\square} \times \mathbb{P}_{\square} \times \mathbb{T}_{\square} \times \mathbb{Q}_{\square} \times \mathbb{R}$ with

$$\langle \boldsymbol{\sigma} : \boldsymbol{\epsilon}[\delta\mathbf{u}]\rangle_{\square} - \frac{1}{|\Omega_{\square}|} \times \int_{\Gamma^{+}_{\square}} \lambda^{(u)} \cdot [\![\delta\mathbf{u}]\!]_{\square}\, \mathrm{d}\Gamma = 0 \quad \forall\, \delta\mathbf{u} \in \mathbb{U}_{\square}, \tag{27a}$$

$$\langle \boldsymbol{\gamma} \cdot \boldsymbol{\nabla}\delta\varphi\rangle_{\square} + \langle \boldsymbol{\Phi}\delta\varphi\rangle_{\square} - \bar{\mu}^{(\varphi)}\langle\delta\varphi\rangle_{\square} - \frac{1}{|\Omega_{\square}|} \times \int_{\Gamma^{+}_{\square}} \lambda^{(\varphi)} [\![\delta\varphi]\!]_{\square}\, \mathrm{d}\Gamma = 0 \quad \forall\, \delta\varphi \in \mathbb{P}_{\square}, \tag{27b}$$

$$-\frac{1}{|\Omega_{\square}|}\int_{\Gamma^{+}_{\square}} \delta\lambda^{(u)} \cdot [\![\mathbf{u}]\!]_{\square}\, \mathrm{d}\Gamma = -\frac{1}{|\Omega_{\square}|} \times \int_{\Gamma^{+}_{\square}} \delta\lambda^{(u)} \otimes [\![\mathbf{x}]\!]_{\square}\, \mathrm{d}\Gamma : \bar{\boldsymbol{\epsilon}} \quad \forall\, \delta\lambda^{(u)} \in \mathbb{T}_{\square}, \tag{27c}$$

$$-\frac{1}{|\Omega_{\square}|}\int_{\Gamma^{+}_{\square}} \delta\lambda^{(\varphi)} [\![\varphi]\!]_{\square}\, \mathrm{d}\Gamma = -\frac{1}{|\Omega_{\square}|} \times \int_{\Gamma^{+}_{\square}} \delta\lambda^{(\varphi)} [\![\mathbf{x}]\!]_{\square}\, \mathrm{d}\Gamma \cdot \bar{\boldsymbol{\zeta}} \quad \forall\, \delta\lambda^{(\varphi)} \in \mathbb{Q}_{\square}, \tag{27d}$$

$$-\delta\bar{\mu}^{(\varphi)}\langle\varphi\rangle_{\square} = -\delta\bar{\mu}^{(\varphi)}\bar{\varphi} \quad \forall\, \delta\bar{\mu}^{(\varphi)} \in \mathbb{R}, \tag{27e}$$

with pertinent spaces

$$\mathbb{U}_{\square} := \left\{ \mathbf{u} \in [H^1(\Omega)]^{\dim} \,\middle|\, \int_{\Omega_{\square}} \mathbf{u}\, \mathrm{d}\Omega = 0 \text{ in } \Omega_{\square} \right\}, \tag{28a}$$

$$\mathbb{P}_{\square} := \left\{ \varphi \in [H^1(\Omega)]^{1} \right\}, \tag{28b}$$

$$\mathbb{T}_{\square} := \left\{ \lambda^{(u)} \in [L_2(\Gamma^{+}_{\square})]^{\dim} \right\}, \tag{28c}$$

$$\mathbb{Q}_{\square} := \left\{ \lambda^{(\varphi)} \in [L_2(\Gamma^{+}_{\square})] \right\}. \tag{28d}$$

Note that the RVE phase-field bounds $\varphi \in [0, 1]$ are self-regulated by the weak form equations and need not be incorporated in the space (28b). Moreover, the Lagrange multipliers $\lambda^{(u)}$, $\lambda^{(\varphi)}$ and $\bar{\mu}^{(\varphi)}$ are related to the macro-scale quantities defined in Problem Statement 4 as

$$\bar{\boldsymbol{\sigma}} = \frac{1}{|\Omega_{\square}|}\int_{\Gamma^{+}_{\square}} \lambda^{(u)} \otimes [\![\mathbf{x}]\!]_{\square}\, \mathrm{d}\Gamma, \tag{29a}$$

$$\overline{\mathbf{Q}} + \bar{\boldsymbol{\gamma}} = \frac{1}{|\Omega_{\square}|}\int_{\Gamma^{+}_{\square}} \lambda^{(\varphi)} [\![\mathbf{x}]\!]_{\square}\, \mathrm{d}\Gamma, \tag{29b}$$

$$\overline{\boldsymbol{\Phi}} = \bar{\mu}^{(\varphi)}, \tag{29c}$$

with the jump operator $[\![\bullet]\!]_{\square}$ defined as $[\![\bullet]\!]_{\square} = \bullet^{+} - \bullet^{-}$. The superscripts $+$ and $-$ are indicative of the RVE boundaries $\Gamma^{+}_{\square}$ and $\Gamma^{-}_{\square}$ respectively, as shown in Fig. 2a. The RVE boundary $\Gamma^{+}_{\square}$ has a positive outward normal, and $\Gamma^{-}_{\square}$ has a negative outward normal in a Cartesian coordinate system . ■

Incorporating the constraint Eqs. (27c), (27d) and (27e) in the RVE problem ensures the fulfilment of the Hill–Mandel macro-homogeneity conditions (Hill, 1963, 1984; Nemat-Nasser, 1999). A formal proof of the same is presented in Appendix A of this manuscript.

Problem Statement 5 allows an independent discretisation of the Lagrange multipliers $\lambda^{(u)}$ and $\lambda^{(\varphi)}$ from that used for the displacement and phase-field. As elucidated in Larsson et al. (2011), theoretically, using the same discretisation for the solution fields and the Lagrange multipliers at the RVE boundary enforces a strongly periodic boundary condition whereas, adopting a single Lagrange multiplier element for the RVE edge as shown in Fig. 2b results in a Neumann boundary condition. However, Svenning et al. (2016a) showed that LBB-stability is ensured only if the solution fields ($\mathbf{u}$ and φ in this manuscript) mesh have at least one node inside each of their corresponding Lagrange multiplier ($\lambda^{(u)}$, $\lambda^{(\varphi)}$) elements. In this manuscript, strongly periodic boundary conditions are enforced through restrictive enrichment of the displacement and phase-field test and trial spaces. This results in:

Problem Statement 6. Find $(\mathbf{u},\, \varphi,\, \bar{\mu}^{(\varphi)}) \in \mathbb{U}^{\mathrm{p}}_{\square}(\bar{\boldsymbol{\epsilon}}) \times \mathbb{P}^{\mathrm{p}}_{\square}(\bar{\boldsymbol{\zeta}}) \times \mathbb{R}$ with

$$\langle \boldsymbol{\sigma} : \boldsymbol{\epsilon}[\delta\mathbf{u}]\rangle_{\square} = 0 \quad \forall\, \delta\mathbf{u} \in \mathbb{U}^{\mathrm{p}}_{\square}(0), \tag{30a}$$

$$\langle \boldsymbol{\gamma} \cdot \boldsymbol{\nabla}\delta\varphi\rangle_{\square} + \langle \boldsymbol{\Phi}\delta\varphi\rangle_{\square} - \bar{\mu}^{(\varphi)}\langle\delta\varphi\rangle_{\square} = 0 \quad \forall\, \delta\varphi \in \mathbb{P}^{\mathrm{p}}_{\square}(0), \tag{30b}$$

$$-\delta\bar{\mu}^{(\varphi)}\langle\varphi\rangle_{\square} = -\delta\bar{\mu}^{(\varphi)}\bar{\varphi} \quad \forall\, \delta\bar{\mu}^{(\varphi)} \in \mathbb{R}, \tag{30c}$$

using the test and trial spaces

$$\mathbb{U}^{\mathrm{p}}_{\square}(\bar{\boldsymbol{\epsilon}}) := \left\{ \mathbf{u} \in [H^1(\Omega)]^{\dim} \,\middle|\, \mathbf{u}^{+} - \mathbf{u}^{-} = \bar{\boldsymbol{\epsilon}} \cdot [\mathbf{x}^{+} - \mathbf{x}^{-}] \text{ on } \Gamma^{+}_{\square}, \int_{\Omega_{\square}} \mathbf{u}\, \mathrm{d}\Omega = 0 \text{ in } \Omega_{\square} \right\}, \tag{31a}$$

$$\mathbb{P}^{\mathrm{p}}_{\square}(\bar{\boldsymbol{\zeta}}) := \left\{ \varphi \in [H^1(\Omega)]^{1} \,\middle|\, \varphi^{+} - \varphi^{-} = \bar{\boldsymbol{\zeta}} \cdot [\mathbf{x}^{+} - \mathbf{x}^{-}] \text{ on } \Gamma^{+}_{\square} \right\}. \tag{31b}$$

■

Remark 4. The RVE Weak/Strong Periodicity problem requires fixing one of the RVE corner nodes (bottom left node is chosen in this manuscript) in order to restrict rigid body translations.

3.4.2. RVE Neumann problem

The RVE Neumann problem arises from choosing trial spaces for the Lagrange multipliers $\lambda^{(u)} \in \mathbb{T}_{\square}$ and $\lambda^{(\varphi)} \in \mathbb{Q}_{\square}$ such that

$$\mathbb{T}_{\square} := \left\{ \lambda^{(u)} \in [L_2(\Gamma^{+}_{\square})]^{\dim} \,\middle|\, \lambda^{(u)} = \bar{\boldsymbol{\sigma}} \cdot \mathbf{n} \text{ on } \Gamma_{\square},\, \bar{\boldsymbol{\sigma}} \in \mathbb{R}^{\dim\times\dim}_{\mathrm{sym}} \right\}, \tag{32a}$$

$$\mathbb{Q}_{\square} := \left\{ \lambda^{(\varphi)} \in [L_2(\Gamma^{+}_{\square})] \,\middle|\, \lambda^{(\varphi)} = \bar{\boldsymbol{\gamma}} \cdot \mathbf{n} \text{ on } \Gamma_{\square},\, \bar{\boldsymbol{\gamma}} \in \mathbb{R}^{\dim} \right\}. \tag{32b}$$

Here, $\bar{\boldsymbol{\sigma}}$ and $\bar{\boldsymbol{\gamma}}$ are homogenised quantities dual to $\bar{\boldsymbol{\epsilon}}$ and $\bar{\boldsymbol{\zeta}}$ respectively, and $\mathbf{n}$ is the surface normal. Adopting the aforementioned trial spaces in Problem Statement 5, along with trivial manipulation results the RVE Neumann problem that reads:

Problem Statement 7. Find $(\mathbf{u},\, \varphi,\, \bar{\boldsymbol{\sigma}},\, \bar{\boldsymbol{\gamma}},\, \bar{\mu}^{(\varphi)}) \in \mathbb{U}_{\square} \times \mathbb{P}_{\square} \times \mathbb{R}^{\dim\times\dim}_{\mathrm{sym}} \times \mathbb{R}^{\dim} \times \mathbb{R}$ with

$$\langle \boldsymbol{\sigma} : \boldsymbol{\epsilon}[\delta\mathbf{u}]\rangle_{\square} - \bar{\boldsymbol{\sigma}} : \langle \boldsymbol{\epsilon}[\delta\mathbf{u}]\rangle_{\square} = 0 \quad \forall\, \delta\mathbf{u} \in \mathbb{U}_{\square}, \tag{33a}$$

$$\langle \boldsymbol{\gamma} \cdot \boldsymbol{\nabla}\delta\varphi\rangle_{\square} + \langle \boldsymbol{\Phi}\delta\varphi\rangle_{\square} - \bar{\boldsymbol{\gamma}} \cdot \langle \boldsymbol{\nabla}\delta\varphi\rangle_{\square} - \bar{\mu}^{(\varphi)}\langle\delta\varphi\rangle_{\square} = 0 \quad \forall\, \delta\varphi \in \mathbb{P}_{\square}, \tag{33b}$$

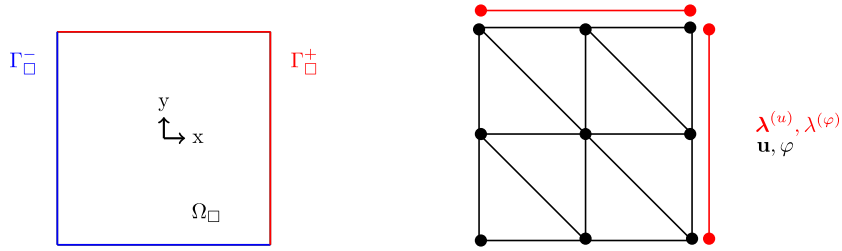

(a) RVE boundary $\Gamma_\square$ split into $\Gamma_\square^+$ and $\Gamma_\square^-$. (b) LBB-stable discretisation.

Fig. 2. Figures showing (a.) RVE $\Omega_\square \in \mathbb{R}^2$ with the boundary split for periodicity constraints, and (b.) an LBB-stable RVE discretisation where • and • indicate solutions fields $(\mathbf{u},\varphi)$ and Lagrange multipliers $(\lambda^{(u)}, \lambda^{(\varphi)})$ nodes respectively. (For interpretation of the references to colour in this figure legend, the reader is referred to the web version of this article.)

$$-\delta\bar{\boldsymbol{\sigma}} : \langle \boldsymbol{\epsilon}[\mathbf{u}] \rangle_\square = -\delta\bar{\boldsymbol{\sigma}} : \bar{\boldsymbol{\epsilon}} \quad \forall\, \delta\bar{\boldsymbol{\sigma}} \in \mathbb{R}^{\dim\times\dim}_{\text{sym}}, \tag{33c}$$

$$-\delta\bar{\boldsymbol{\gamma}} \cdot \langle \boldsymbol{\nabla}\varphi \rangle_\square = -\delta\bar{\boldsymbol{\gamma}} \cdot \bar{\boldsymbol{\zeta}} \quad \forall\, \delta\bar{\boldsymbol{\gamma}} \in \mathbb{R}^{\dim}, \tag{33d}$$

$$-\delta\bar{\mu}^{(\varphi)} \langle \varphi \rangle_\square = -\delta\bar{\mu}^{(\varphi)} \bar{\varphi} \quad \forall\, \delta\bar{\mu}^{(\varphi)} \in \mathbb{R}, \tag{33e}$$

using the test and trial spaces

$$\mathbb{U}_\square := \Big\{ \mathbf{u} \in [H^1(\Omega)]^{\dim} \,\Big|\, \int_{\Omega_\square} \mathbf{u}\, \mathrm{d}\Omega = 0 \text{ in } \Omega_\square, \int_{\Gamma_\square} (\mathbf{u} \otimes \mathbf{n})^{\text{skew}}\, \mathrm{d}\Gamma = 0 \text{ on } \Gamma_\square \Big\}, \tag{34a}$$

$$\mathbb{P}_\square := \Big\{ \varphi \in [H^1(\Omega)]^1 \Big\}. \quad \blacksquare \tag{34b}$$

Remark 5. The RVE Neumann problem requires fixing one of the RVE corner nodes (bottom left node is chosen in this manuscript) in order to restrict rigid body translations. Furthermore, the RVE Neumann problem allows a small discrepancy in the context of consistency with the initial values. However, this discrepancy exists only in the first step of a fully coupled two-scale analysis.

3.4.3. RVE Dirichlet problem

The RVE Dirichlet Problem results from choosing to enforce displacement and phase-field values on the RVE boundary. This results in:

Problem Statement 8. Find $(\mathbf{u}, \varphi, \bar{\mu}^{(\varphi)}) \in \mathbb{U}^{\mathrm{D}}_\square(\bar{\boldsymbol{\epsilon}}) \times \mathbb{P}^{\mathrm{D}}_\square(\bar{\varphi}, \bar{\boldsymbol{\zeta}}) \times \mathbb{R}$ with

$$\langle \boldsymbol{\sigma} : \boldsymbol{\epsilon}[\delta\mathbf{u}] \rangle_\square = 0 \quad \forall\, \delta\mathbf{u} \in \mathbb{U}^{\mathrm{D}}_\square(0), \tag{35a}$$

$$\langle \boldsymbol{\gamma} \cdot \boldsymbol{\nabla}\delta\varphi \rangle_\square + \langle \boldsymbol{\Phi}\delta\varphi \rangle_\square - \bar{\mu}^{(\varphi)} \langle \delta\varphi \rangle_\square = 0 \quad \forall\, \delta\varphi \in \mathbb{P}^{\mathrm{D}}_\square(0), \tag{35b}$$

$$-\delta\bar{\mu}^{(\varphi)} \langle \varphi \rangle_\square = -\delta\bar{\mu}^{(\varphi)} \bar{\varphi} \quad \forall\, \delta\bar{\lambda}^{(\varphi)} \in \mathbb{R}_\square, \tag{35c}$$

using the test and trial spaces

$$\mathbb{U}^{\mathrm{D}}_\square(\bar{\boldsymbol{\epsilon}}) := \Big\{ \mathbf{u} \in [H^1(\Omega)]^{\dim} \,\Big|\, \mathbf{u} = \bar{\boldsymbol{\epsilon}} \cdot [\mathbf{x} - \bar{\mathbf{x}}] \text{ on } \Gamma_\square \Big\}, \tag{36a}$$

$$\mathbb{P}^{\mathrm{D}}_\square(\bar{\varphi}, \bar{\boldsymbol{\zeta}}) := \Big\{ \varphi \in [H^1(\Omega)]^1 \,\Big|\, \varphi = \bar{\varphi} + \bar{\boldsymbol{\zeta}} \cdot [\mathbf{x} - \bar{\mathbf{x}}] \text{ on } \Gamma_\square \Big\}. \quad \blacksquare \tag{36b}$$

Remark 6. Enforcing a Dirichlet boundary condition as stated in Eq. (36b) on the phase-field would lead to a 'undesirable' conflict in the presence of initial fractures on the RVE boundary. It is presented in this manuscript solely as a proof of concept and for the sake of completeness.

So far, the macro-scale kinematic quantities $\bar{\boldsymbol{\epsilon}}$, $\bar{\varphi}$ and $\bar{\boldsymbol{\zeta}}$ have been defined as the volume-average of their RVE counterparts. Therefore, the macro-scale problem in Section 3.3 and the RVE problems (Problem Statements 5–8) derived in this section constitute a volume-average based two-scale phase-field fracture model. In the next sub-section, a surface-average based two-scale phase-field fracture model is introduced that defines the macro-scale phase-field $\bar{\varphi}$ as the surface-average of its RVE counterpart.

3.5. Surface-average based two-scale phase-field fracture model

The surface-average based two-scale phase-field fracture model defines the macro-scale phase-field $\bar{\varphi}$ as the surface-average[5] of the RVE phase-field φ,

$$\bar{\varphi} = \langle\langle \varphi \rangle\rangle_\square, \tag{37}$$

keeping the other kinematic quantities $\boldsymbol{\epsilon}[\bar{\mathbf{u}}]$ and $\boldsymbol{\nabla}\bar{\varphi}$ same as in the volume-average based two-scale phase-field model. This results in the constraints (27e), (30c), (33e) and (35c) being replaced by

$$-\delta\bar{\mu}^{(\varphi)} \langle\langle \varphi \rangle\rangle_\square = -\delta\bar{\mu}^{(\varphi)} \bar{\varphi} \quad \forall\, \delta\bar{\mu}^{(\varphi)} \in \mathbb{R}, \tag{38}$$

with $\bar{\varphi}$ evaluated at a material point $\bar{\mathbf{x}} \in \Omega$. Consequently, the term $\bar{\mu}^{(\varphi)} \langle \delta\varphi \rangle_\square$ is replaced by $\bar{\mu}^{(\varphi)} \langle\langle \delta\varphi \rangle\rangle_\square$ in the RVE phase-field evolution equation. The macro-scale equations in Problem Statement 4, however, remain unchanged. The macro-scale and RVE problem statements for the surface-average based two-scale phase-field fracture model are not explicitly stated in this manuscript for brevity.

Remark 7. Note that the macro-scale phase-field being defined as the volume or surface average of its RVE counterpart, is not indicative of fracture on the macro-scale. Rather, it must be treated as an auxiliary macro-scale variable.

3.6. Selective homogenisation based two-scale phase-field fracture model

Yet another variant of the two-scale phase-field fracture model is proposed in this sub-section, based on '*selective homogenisation*' of the solution fields. '*Selective homogenisation*' refers to the selective upscaling of the solution variables from the sub-scale to the macro-scale. In this regard, a simple choice would be to discard any notion of the phase-field variable at the macro-scale scale, i.e., the phase-field is assumed to live only on the RVE domain. This '*special case*' is not new in the computational homogenisation literature. For instance, the pressure field was assumed to live only on the RVE domain in liquid-phase

[5] The 'surface' here refers to the external boundary. Pertinent averaging definitions are given by (21a) and (21b).

sintering (Ohman et al., 2013), Stokes' flow (Sandstrom et al., 2013) and fluid transport in fractured media (Pollmann et al., 2020) problems, to cite a few.

For the phase-field fracture problem, assuming the phase-field to live only on the RVE domain leads to the non-existence of the macro-scale phase-field evolution equation (24b), thereby circumventing the need to extract the homogenised quantities dual to the macro-scale phase-field and its gradient. The absence of the macro-scale phase-field evolution equation is expected to reduce computational cost compared to the volume-average and surface-average based two-scale phase-field fracture models. However, assuming the phase-field only as an RVE quantity would result in an RVE-based local material model at the macro-scale, similar to the local damage model in continuum damage mechanics. The RVE-based local dissipative material model would render the macro-scale problem mesh sensitive (refer to de Borst et al. (1993) for more on this aspect).

As far as the RVE problems (Problem Statements 5–8) are concerned, considering the phase-field only as an RVE quantity would eliminate the need for constraints (27e), (30c), (33e) and (35c). However, constraints on the RVE phase-field must be enforced such that the Hill–Mandel macro-homogeneity conditions are satisfied. This is achieved through Neumann and Periodic boundary conditions with a zero macro-scale phase-field gradient.

4. Single-scale RVE numerical study

The single-scale numerical study extracts the homogenised dual quantities for the different two-scale phase-field fracture models, discussed earlier in Section 3. To this end, a set of numerical experiments are carried out on artificially created RVEs. The RVEs differ in material constituents and/or initial fracture topology. The initial fractures are modelled by defining interfaces within the RVE domain and prescribing $\varphi = 1$ on these surfaces. All material and geometric parameters pertaining to the RVEs are addressed in the next sub-section. The subsequent sub-sections conduct a three-fold numerical investigation, where

- *Study I* computes the homogenised dual quantities pertaining to the selective homogenisation based two-scale phase-field fracture model (refer to Section 3.6),
- *Study II* compares the volume-average and surface-average based two-scale phase-field fracture models, based on their homogenised stress–strain response, and
- *Study III* involves a parametric study in order to ascertain the influence of the macro-scale phase-field gradient on the homogenised dual quantities in the volume-average and surface-average based two-scale phase-field fracture models.

4.1. Artificially created RVEs

Three different artificially created RVEs are considered in this manuscript with varying initial fracture topology and/or material constituents, as shown in Fig. 3. All of them are two-dimensional unit squares (in mm).

Fig. 3a shows an RVE with an initial vertical fracture. This RVE is symmetric w.r.t the fracture topology. The second RVE in Fig. 3b is devoid of initial fractures, instead, the matrix is embedded with randomly placed inclusions of varying size (shown in dark blue colour). These inclusions fulfil wall-periodicity as they are allowed to penetrate through the RVE boundary and appear on the opposite edge. As such, material periodicity is invoked. Finally, Fig. 3c shows an RVE with random initial fractures, that fulfils wall-periodicity. Note that the latter two RVEs are not symmetric as far as the material and fracture topology are concerned.

The material and geometric properties for the different RVEs are presented in Table 1. Note that the matrix material remains the same in all the RVEs, and the inclusion properties apply only to the RVE in Fig. 3b.

Table 1
RVE geometric and material information.

Property	Value
RVE	1 mm × 1 mm, Plane strain
λ_{matrix}, $\lambda_{\text{inclusion}}$	131.154 GPa, 13 100.154 GPa
μ_{matrix}, $\mu_{\text{inclusion}}$	80.769 GPa, 8000.769 GPa
$G_{\text{c,matrix}}$, $G_{\text{c,inclusion}}$	2700 N/m, 270 000 N/m
l	1.5e − 2 mm
max. element size	$l/2$

Table 2
RVE loading conditions for *Study I*.

RVE	$\Delta\bar{\epsilon}_{xx}$ [–]	$\bar{\zeta}_x$ [mm^{-1}]	$\bar{\zeta}_y$ [mm^{-1}]
Single fracture	1e−5	0	0
Stiff inclusions	1e−5	0	0
Random fractures	1e−5	0	0

Throughout the entire numerical investigation, the RVEs are subjected to a strain-loading in the x-direction. The loading is quasi-static, and the solution-based error measure (16) is adopted to terminate the iterations with a tolerance $1e-3$.

4.2. Study I

Study I pertains to the selective homogenisation based two-scale phase-field fracture model that considers the phase-field only as an RVE (sub-scale) solution field. (refer to Section 3.6 for details). As such, the problem is driven only through a quasi-static strain-loading in the x-direction. Table 2 presents the strain increments adopted for the different RVEs. When the strain-loading is enforced through DBC and NBC, the phase-field evolution equation is augmented with NBC. However, when the strain loading is applied through SPBC, the SPBC is also enforced on the phase-field.

In the selective homogenisation based two-scale phase-field fracture model, the macro-scale phase-field evolution equation ceases to exist. As such, the homogenised stress $\bar{\sigma}$ (dual to the homogenised strain $\bar{\epsilon}$) is the only macro-scale quantity that requires upscaling. Fig. 4 presents the homogenised stress–strain curves for the three RVEs with different displacement boundary conditions (DBC, NBC, and SPBC). Each sub-figure corresponds to a single RVE, while the curves of different colour represent the different boundary conditions. It is observed from all the sub-figures that the phase-field variable implicitly contained in the definition of the homogenised stress (see Eq. (25a)) manifests in the form of a dissipative-type behaviour. Furthermore, the DBC is found to yield a stiffer stress–strain response in comparison to the NBC, while the SPBC stress–strain curve lies in between the DBC and NBC response. The stiff behaviour of the DBC, owing to the rather restrictive enforcement of linearly varying displacements, is established in the computational homogenisation literature.

Fig. 5 shows the phase-field fracture topology at failure for the RVE with a single initial fracture. Irrespective of the applied boundary conditions, this fracture topology remains the same, i.e., through elongation of the initial vertical crack. This explains the closeness homogenised stress–strain curves in Fig. 4 with different boundary conditions. However, in the case of DBC, the fracture is not allowed to reach the RVE boundary, rather it spreads horizontally as seen in the red curve in Fig. 5a. This prevents the total loss of material integrity and results in an artificial stiffening (evident from the horizontal plateau). The artificial stiffening is, however, not observed with the NBC and SPBC as observed from the green and blue curves in Fig. 4.

Figs. 6 and 7 show the phase-field at the fracture initiation stage and at the final step of the analysis respectively, for the RVE with stiff inclusions. It is observed that NBC and SPBC results in fracture initiation on the RVE boundary (see Figs.6b and 6c) which propagate into

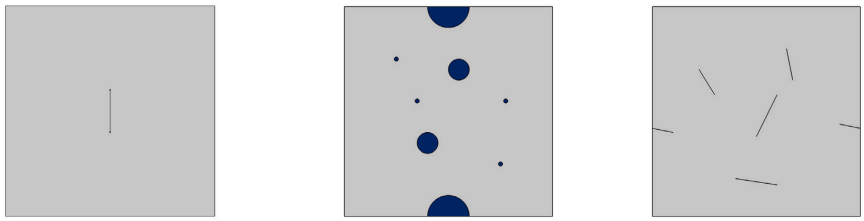

(a) RVE with single fracture (b) RVE with stiff inclusions (c) RVE with random fractures

Fig. 3. Figure showing the different RVEs used for the numerical study. (For interpretation of the references to colour in this figure legend, the reader is referred to the web version of this article.)

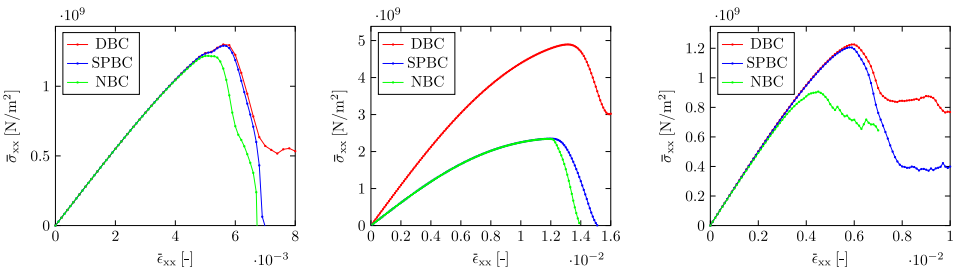

(a) RVE with single fracture (b) RVE with stiff inclusions (c) RVE with random fractures

Fig. 4. Figure showing homogenised stress–strain (x-direction) curves for the different RVEs. (For interpretation of the references to colour in this figure legend, the reader is referred to the web version of this article.)

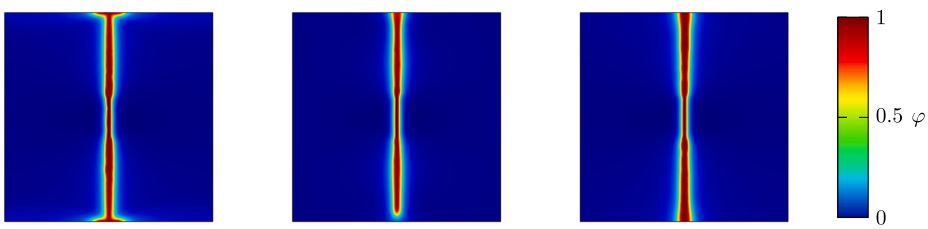

(a) DBC (b) NBC (c) SPBC

Fig. 5. Figures showing phase-field φ in the final time-step for the RVE with single fracture. (For interpretation of the references to colour in this figure legend, the reader is referred to the web version of this article.)

the RVE with increase in loading until total loss of integrity of the RVE (see Figs.7b and 7c). However, for the DBC, fracture initiation occurs inside the RVE domain and not on the RVE boundary as observed from Fig. 6a. Furthermore, similar to the RVE with single initial fracture, total loss of integrity is not achieved as the fracture is not allowed to develop at the RVE boundary. This manifests in the form of an artificial stiffening in the stress–strain curve shown in Fig. 4b. Moreover, the restrictive nature of linearly varying displacements enforced by the DBC in conjunction with stiff inclusions on the RVE boundary yields a stiffer response compared to NBC and SPBC in the pre-peak regime of the stress–strain curve.

The phase-field fracture topologies at failure for the different RVEs with varying boundary conditions poses a question as to which of them are reasonable. In this context, the DBC that results in an unphysical artificially stiffened response is ruled out. Next, the NBC circumvents the issue with the artificially stiffened response resulting in a realistic fracture pattern for the RVEs with no initial fractures on the boundaries as observed from Figs. 5b and 7b. However, when the RVE has initial fractures at the boundary, the NBC leads to widening of these existing fractures as seen in Fig. 8b, resulting in an unrealistic response. The SPBC, however, circumvents both the artificial stiffening and widening of existing boundary fractures, at the cost of wall-periodicity (see Figs. 5c, 7c and 8c). Therefore, subsequent studies in this manuscript (i.e., *Study II* and *III*) involve only the SPBC.

Next, in Fig. 9, the macro-scale phase-field $\bar{\varphi}$ (obtained as a post-processing step) is plotted against the homogenised strain $\bar{\epsilon}_{xx}$ (in x-direction) for the SPBC. The blue and the red curve correspond to the volume and the surface-averaged definition of $\bar{\varphi}$ respectively. In either case, $\bar{\varphi}$ is far below one, even after the total loss of material integrity. Thus, the macro-scale phase-field is not an indicator of a fully developed fracture. Rather, upon reaching the total loss of material integrity, the $\bar{\varphi}$ curve flattens to form a horizontal plateau. The formation of the

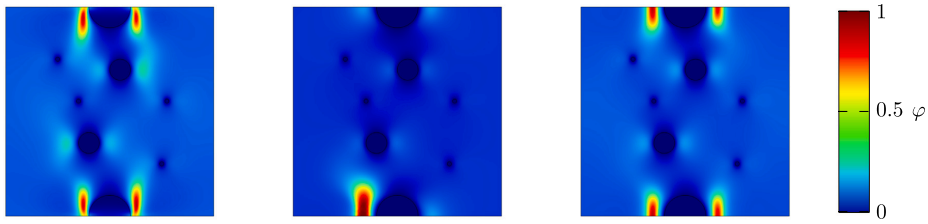

(a) DBC (b) NBC (c) SPBC

Fig. 6. Figures showing phase-field φ initiation for the RVE with stiff inclusions. (For interpretation of the references to colour in this figure legend, the reader is referred to the web version of this article.)

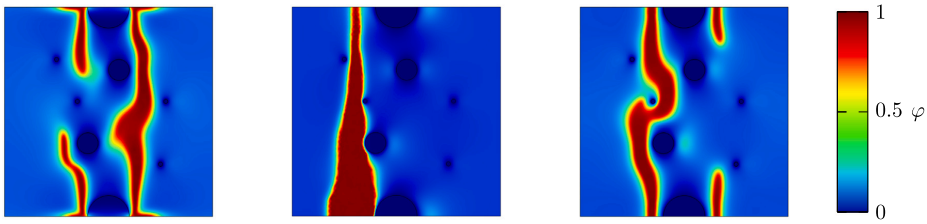

(a) DBC (b) NBC (c) SPBC

Fig. 7. Figures showing phase-field φ in the final time-step for the RVE with stiff inclusions. (For interpretation of the references to colour in this figure legend, the reader is referred to the web version of this article.)

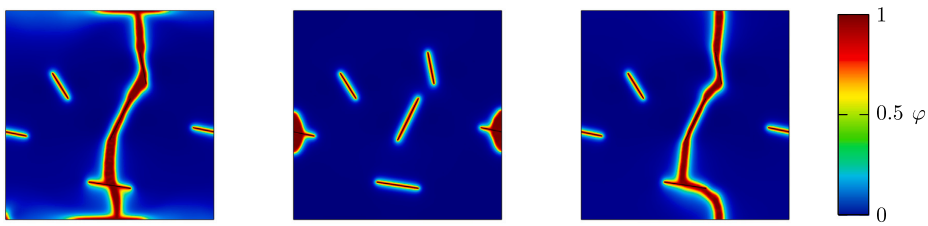

(a) DBC (b) NBC (c) SPBC

Fig. 8. Figures showing phase-field φ in the final time-step for the RVE with random fractures. (For interpretation of the references to colour in this figure legend, the reader is referred to the web version of this article.)

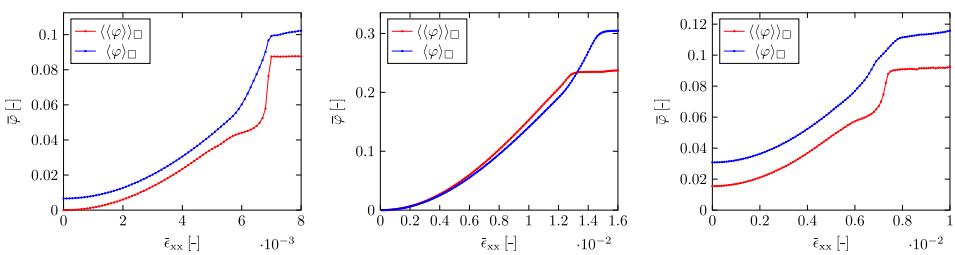

(a) RVE with a single fracture (b) RVE with stiff inclusions (c) RVE with random initial cracks

Fig. 9. Figure showing homogenised phase-field $\overline{\varphi}$ as a function of the homogenised strain (in x-direction) for the different RVEs. Here, $\langle\langle\varphi\rangle\rangle_{\square}$ and $\langle\varphi\rangle_{\square}$ indicate the volume average and surface average definitions of the macro-scale phase-field $\overline{\varphi}$. (For interpretation of the references to colour in this figure legend, the reader is referred to the web version of this article.)

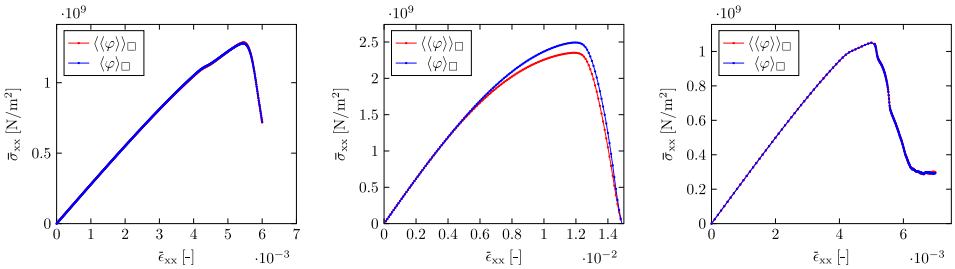

(a) RVE with single fracture (b) RVE with stiff inclusions (c) RVE with random fracture

Fig. 10. Figure showing homogenised stress–strain (x-direction) curves for the different RVEs. (For interpretation of the references to colour in this figure legend, the reader is referred to the web version of this article.)

plateau signifies a halt in the formation of new fracture or propagation of existing fractures. Later, in *Study II* and *III*, the blue $\bar{\varphi}$ curve is used to enforce the constraint (30c) for the volume-average based two-scale phase-field fracture model. Likewise, the constraint (38), pertaining to the surface-average based two-scale phase-field fracture model is enforced using the red $\bar{\varphi}$ curve.

4.3. Study II

This sub-section concerns the volume-average and surface-average based two-scale phase-field fracture models. The numerical aspects of both models (space-variational equations and constraints) are discussed in Section 3. Similar to *Study I*, a strain-loading is applied to the three RVEs (cf. Tables 2 and 3), albeit using the only SPBC. Additionally, the constraint (30c) in the volume-average based two-scale phase-field model is enforced using $\bar{\varphi}$ parametrised by the blue curves in Fig. 9. Likewise, for the surface constraint (38) in the surface-average based two-scale model, $\bar{\varphi}$ is parametrised by the red curves in Fig. 9. Apart from the aforementioned constraints, the macro-scale phase-field gradient is set to zero.

Fig. 10 shows the homogenised stress–strain response obtained for the different RVEs. In all the sub-figures, the blue curves correspond to the volume-average based two-scale phase-field fracture model, while the red curves belong to the surface-average based two-scale phase-field fracture model. It is observed that blue and the red curves are comparable (maximum relative difference in stresses $\approx$ 6% in Fig. 10b) when the surface and volume-average phase-field is imposed in a consistent manner using the curves in Fig. 9. Moreover, the fracture at the final time-step also remains similar to those presented in Figs. 5c, 7c and 8c.

4.4. Study III

This sub-section extends *Study II* in order to assess the influence of zero/non-zero macro-scale phase-field gradient $\bar{\boldsymbol{\zeta}}$ on the RVE homogenised dual quantities. To this end, numerical experiments are carried out on the RVE with inclusions (see Fig. 3b). The RVE loading conditions remain the same as presented in Table 3, the only change being, the SPBC on the RVE phase-field is enforced with a $\bar{\boldsymbol{\zeta}}$, which is not explicitly set to zero. Instead, $\bar{\boldsymbol{\zeta}}$ is parametrised as

$$\bar{\boldsymbol{\zeta}} = \boldsymbol{\alpha}\bar{\varphi} = [\alpha_x, \alpha_y]^T \beta(\bar{\varepsilon}_{xx}). \tag{39}$$

where α_x [mm^{-1}] and α_y [mm^{-1}] are constants, and $\beta(\bar{\varepsilon}_{xx})$ is chosen as a linear function of the homogenised strain.[6] Based on the choice of these quantities, different parametrisations of $\bar{\boldsymbol{\zeta}}$ is achieved. For instance, choosing $\alpha_x = \alpha_y = 0$ or $\beta(\bar{\varepsilon}_{xx}) = 0$ results in $\bar{\boldsymbol{\zeta}} = 0$. In this study, α_y is set to zero and α_x is chosen randomly, such that the macro-scale phase-field does not result in $\varphi \notin [0, 1]$. Appendix B explains this aspect in detail.

Fig. 11 presents the homogenised dual quantities for the volume-average based two-scale phase-field fracture model. The homogenised dual quantities are defined in the Problem Statement 4 (see Eqs. (25a)–(25d)). The homogenised stress shown in Fig. 11a is dual to the homogenised strain. It is observed that the stress–strain response is objective w.r.t. the chosen α_x values. As the macro-scale phase-field gradient is parametrised using α_x, the aforementioned observation indicates that the homogenised stress–strain is not influenced by the macro-scale phase-field gradient. The dual quantity $\bar{\Phi}$, defined in (25d) represents the volume-average of the imbalance between the fracture driving and resisting forces, excluding the gradient term. It is dual to the macro-scale phase-field $\bar{\varphi}$. Fig. 11b shows that $\bar{\Phi}$ is objective w.r.t the chosen macro-scale phase-field gradient parametrisation. Finally, the homogenised quantity $\bar{\gamma}_x + \bar{Q}_x$[7] dual to the macro-scale phase-field gradient $\bar{\zeta}_x$ is presented in Fig. 11c. This dual quantity does exhibit a dependence on the chosen macro-scale phase-field gradient parametrisation. This behaviour is attributed to varying local phase-field gradients within the RVE in the vicinity of the fracture zone, with different values of α_x. Moreover, on comparing Fig. 11c with Fig. 11d, it is observed that $\bar{Q}_x$ is the dominant term in the overall homogenised quantity $\bar{\gamma}_x + \bar{Q}_x$, dual to $\bar{\zeta}_x$.

Fig. 12 presents the homogenised dual quantities for the surface-average based two-scale phase-field model. The homogenised dual quantities are defined in (25a)–(25d). Fig. 12a presents the homogenised stress–strain response, which is found to be objective w.r.t the chosen parametrisation of the macro-scale phase-field gradient. This observation is similar to one with the volume-average based two-scale phase-field fracture model in Fig. 11a. However, the homogenised quantity $\bar{\Phi}$, dual to the surface-averaged macro-scale phase-field does exhibit a dependency on the chosen macro-scale phase-field gradient parametrisation. It is important to note that $\bar{\Phi}$ evolution in the surface-average based model differs from the volume-average based model (cf. Figs. 12b and 11b) since they are dual to different quantities, volume-averaged phase-field and surface-averaged phase-field. Furthermore, the homogenised quantity dual to the x-component of the macro-scale phase-field gradient $\bar{\zeta}_x$ also exhibits a dependency on the chosen α_x values, as seen from Fig. 12c. This behaviour is similar to that observed in the case of the volume-average based two-scale phase-field model (cf. Figs. 11c and 12c). The reason for this behaviour is mentioned in

[6] In this manuscript, β is chosen as linearly dependent on $\bar{\varepsilon}_{xx}$ in order to impose a (pseudo) time-varying macro-scale phase-field gradient. There may be other ways to carry out such a parametric study.

[7] The subscript x indicates the x-component. Similarly, the subscript y would mean the y-component.

Table 3
RVE loading conditions for *Study II*.

RVE	$\Delta\bar{\epsilon}_{xx}$ [–]	$\bar{\varphi}$ [–] in the constraint equation		$\bar{\zeta}_x$ [mm^{-1}]	$\bar{\zeta}_y$ [mm^{-1}]
		(30c)	(38)		
Single fracture	1e−5	Fig. 9a blue curve	Fig. 9a red curve	0	0
Stiff inclusions	1e−5	Fig. 9b blue curve	Fig. 9b red curve	0	0
Random fractures	1e−5	Fig. 9c blue curve	Fig. 9c red curve	0	0

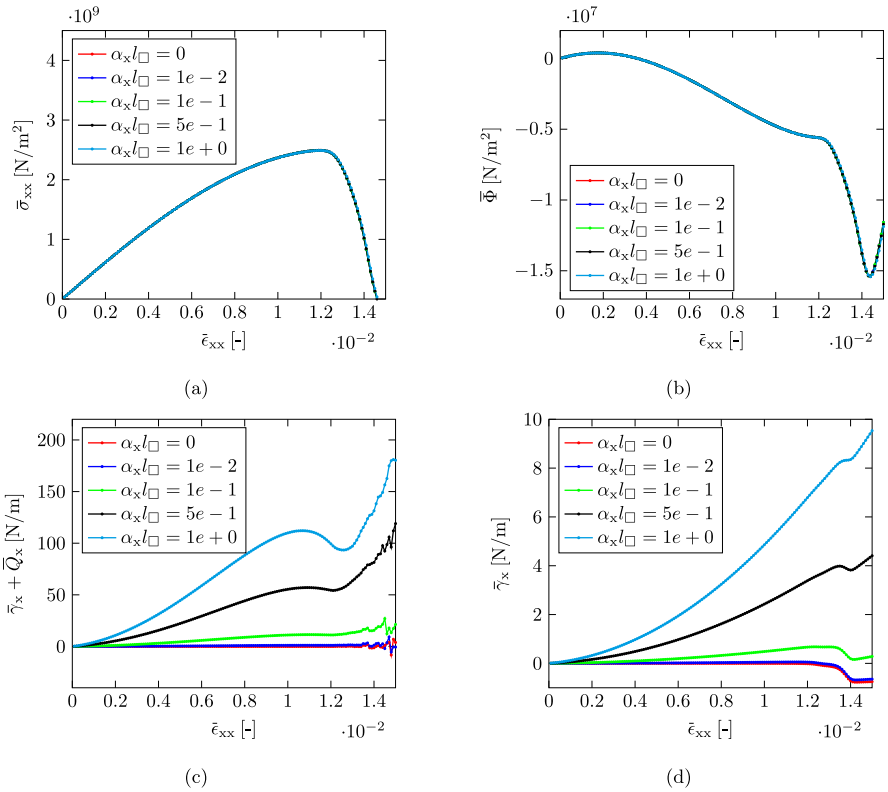

Fig. 11. Figure showing homogenised macro-scale terms defined in (25a)–(25d) for the volume-average based two-scale phase-field fracture model. (For interpretation of the references to colour in this figure legend, the reader is referred to the web version of this article.)

the previous paragraph. Finally, for the surface-average based two-scale phase-field model too, $\bar{Q}_x$ remains the dominant term in the overall quantity $\bar{\gamma}_x + \bar{Q}_x$ (cf. Figs. 12c and 12d).

Both, volume and surface-average based two-scale phase-field fracture model yield dual quantities to the macro-scale phase-field and its gradient, in addition to stress. In this context, it is imperative to carry out a fully coupled two-scale simulation in order to ascertain the effect of these model choices on the macro-scale structural behaviour (for instance, the load–displacement relation). The next section deals precisely with this aspect.

5. Multi-scale FE^2 numerical study

In this section, the two-scale phase-field fracture models based on selective homogenisation and volume-average homogenisation of the phase-field (presented in Section 3) are investigated in the context of a fully coupled two-scale application. To this end, a one-dimensional uniaxial strain macro-scale problem is set up as shown in Fig. 13a. The one-dimensional bar is discretised with four linear elements, 1 metre each in length. The bar is fixed at the left end and loading is applied at the right end in the form of prescribed displacement. Moreover, the cross-sectional area is set to unity apart from the element adjacent to the fixed boundary, where the area has been reduced by 10%. This has been done in order to induce a localisation in that element. Finally, note that all lateral strains are set to zero, in order to ensure a one-dimensional continuum behaviour.

As shown schematically in the two-scale problem in Fig. 13a, each macro-scale Gauss point is associated with a two-dimensional RVE. In this regard, the RVEs with stiff inclusions and random fractures are not chosen for this study as they would require pre-refinement of the mesh along rather complex fracture path to reduce computational expense. Instead, the RVE with a single vertical fracture is chosen for this study

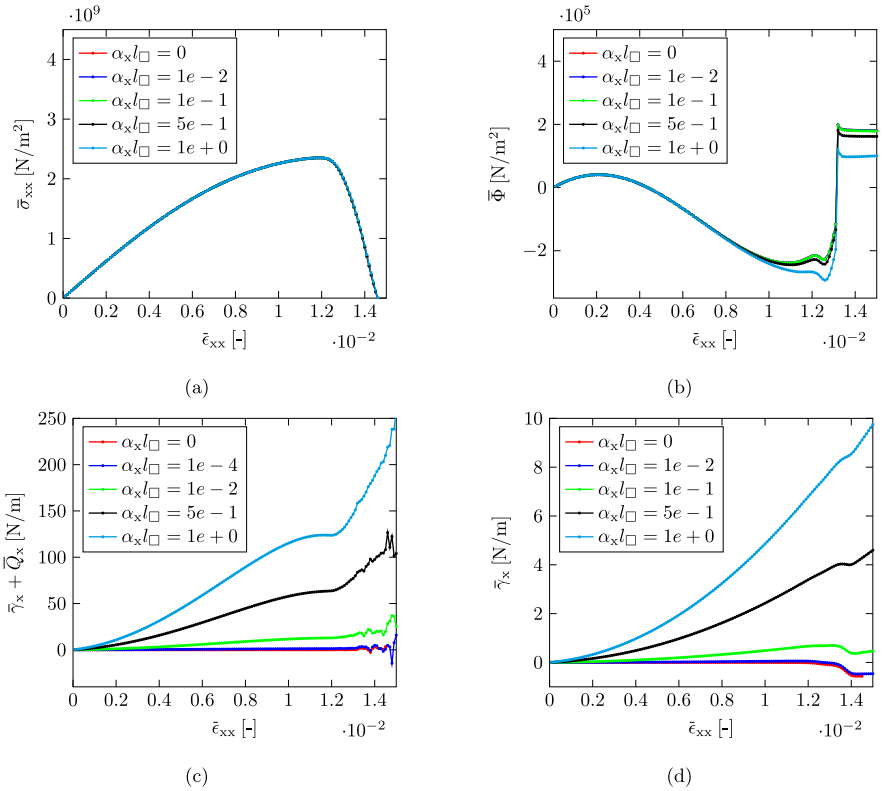

Fig. 12. Figure showing homogenised macro-scale terms defined in (25a)–(25d) for the surface-average based two-scale phase-field fracture model. (For interpretation of the references to colour in this figure legend, the reader is referred to the web version of this article.)

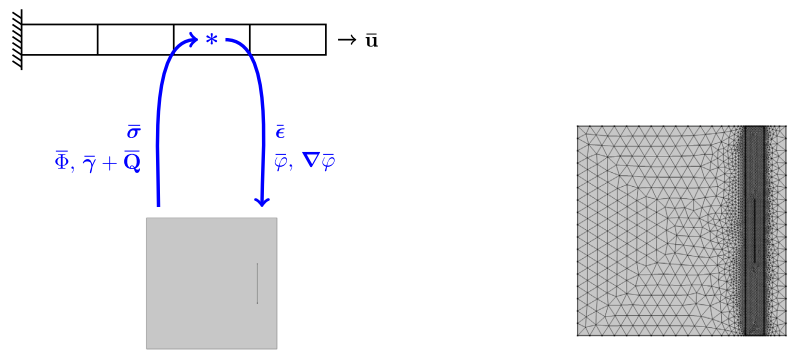

Fig. 13. Figures showing (a) two-scale FE^2 problem schematic with a one-dimensional bar under uniaxial tension and its corresponding two-dimensional RVE, and (b) RVE discretisation used in the study. (For interpretation of the references to colour in this figure legend, the reader is referred to the web version of this article.)

with 0.35 mm offset of the initial fracture (compare RVEs in Figs. 13a and 3a). The material properties remain the same as in Table 1. The RVE mesh is pre-refined in the expected fracture propagation sub-domain as shown in Fig. 13b in order to reduce the computational expenses. The element-size in the sub-domain containing the fracture is set to half of the length-scale parameter in accordance with the recommendations put forward in Miehe et al. (2010b). Moreover, for the volume-average based two-scale phase-field fracture model, a stationary analysis is carried out solely using the phase-field evolution equation to ascertain the initial value of the macro-scale phase-field.

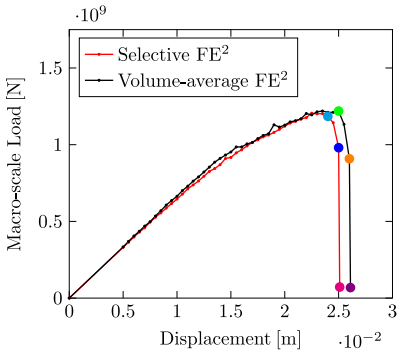

Fig. 14. Figure showing the macro-scale load–displacement curves for the selective homogenisation (in red) and volume-average based (in black) two-scale phase-field fracture models. Moreover, the coloured markers correspond to the coordinates for which the macro-scale Gauss point phase-field is presented in Fig. 15. (For interpretation of the references to colour in this figure legend, the reader is referred to the web version of this article.)

Finally, the solution-based error measure (16) is adopted to terminate the iterations with a tolerance $1e-3$.

Fig. 14 presents the macro-scale load–displacement curves for the two-scale phase-field fracture models with selective and volume-average based homogenisation of the phase-field. Furthermore, for the markers in these curves, the corresponding macro-scale phase-field $\overline{\varphi}$ at the macro-scale Gauss Points (GPs) are presented in Fig. 15. Note that for the selective homogenisation based two-scale phase-field fracture model, $\overline{\varphi}$ is computed as a post-processing quantity as the macro-scale phase-field evolution equation does not exist. Such a modelling choice also renders a local macro-scale behaviour as observed from Fig. 15a, where $\overline{\varphi}$ grows only in one element beyond the peak load (indicated with a cyan and blue markers in Fig. 15a). However, in the case of the volume-average based two-scale phase-field fracture model, $\overline{\varphi}$ is distributed across all the elements from the peak load until failure (indicated with a green, orange and purple markers in Fig. 15b), thereby exhibiting a non-local material behaviour at the macro-scale. This non-local macro-scale material behaviour manifests in the form of higher peak load and prescribed displacement at failure for the volume-average based two-scale phase-field fracture model compared to selective homogenisation based model, as far as the macro-scale load–displacement curves are concerned.

The numerical investigation in this section formally establishes the proof of concept pertaining to solvability of the selective homogenisation and volume-average based two-scale phase-field fracture models in the context of solvability of the fully coupled macro-scale and RVE problems. Furthermore, for the volume-average based two-scale phase-field fracture model, the macro-scale phase-field $\overline{\varphi}$ and its gradients is self-regulated and there is no need for artificial bounds on the macro-scale phase-field gradient while solving the RVE problems. In this regard, it is important to note that $\overline{\varphi}$ is an auxiliary variable regularising the macro-scale problem, and is not indicative of failure. For instance, the RVE attached to the element close to the fixed boundary incurs a total loss of integrity when $\overline{\varphi} \approx 0.1415\%$ (shown in Fig. 15b).

Remark 8. The macro-scale length-scale for the non-selective volume-average based two-scale phase-field fracture model is a priori unknown. Numerical methods for estimation of this length-scale and choosing appropriate discretisation thereafter would be a part of future work.

6. Concluding remarks

A novel two-scale phase-field fracture framework is proposed for computational homogenisation of fractures in complex microstructures (RVEs). The framework has been developed using the Variationally Consistent Homogenisation technique (Larsson et al., 2010b), and it allows the use of several homogenisation measures (volume-averaging, surface-averaging, or selective homogenisation). Within this framework, a family of two-scale phase-field fracture models are developed using the different homogenisation measures w.r.t the phase-field variable. In this context, the macro-scale phase-field is defined as the volume-average and surface-average of its RVE counterpart, resulting in a 'volume-average based two-scale phase-field fracture model' and 'surface-average based two-scale phase-field fracture model' respectively. In both models, the phase-field represent fractures in the RVE (sub-scale), while at the macro-scale, it is treated as an auxiliary variable. The macro-scale phase-field is not indicative of material point failure (does not reach a value ≈ 1 on the total loss of integrity), however, its evolution reaches a horizontal plateau, indicating a halt in the initiation of new fracture(s) or propagation of existing fracture(s). For both, volume and surface-average based two-scale phase-field fracture models, the pertinent coupled momentum balance and phase-field evolution equation are formulated at the macro-scale and sub-scale, along with macro-homogeneity conforming prolongation/homogenisation rules. Furthermore, numerical studies on artificially created RVEs indicate that the homogenised stress–strain response is similar for both models, even though the homogenised dual quantities in the macro-scale phase-field evolution equation differ. In this regard, it is observed that prolongation of the phase-field through first order homogenisation results in a higher order term, which has a dominant contribution compared to the conventional boundary flux term. Furthermore, for a single-scale parametric RVE study, the macro-scale phase-field gradient is required to be bounded in order to obtain physically acceptable meaningful results, i.e., $\varphi \in [0, 1]$ everywhere within the RVE. This manuscript provides an initial estimate of the upper and the lower bound of the macro-scale phase-field gradient. The authors would like to stress that the bounds remain relevant only for parametric studies on RVEs and not in an FE^2 (Feyel, 1999) analysis.

Yet another two-scale phase-field fracture model is developed based on selective homogenisation of the phase-field variable. By construction, this model yields a local material behaviour at the macro-scale, similar to local damage model in continuum mechanics. This phenomenon has been demonstrated in this manuscript using a fully coupled two-scale application. On the contrary, in the same application, the volume-average based two-scale phase-field fracture model yielded a non-local macro-scale material. This behaviour is attributed to the presence of a macro-scale phase-field evolution equation which regularises the macro-scale phase-field. Nonetheless, the fully coupled two-scale application provides a numerical proof of concept that the macro-scale and RVE equations are solvable without the need for bounds on the macro-scale phase-field gradient.

Future studies may involve the determination of the macro-scale length-scale for the volume and the surface-average based two-scale phase-field fracture model. Also, another homogenisation measure could be incorporated in the current framework which results in a macro-scale phase-field that is indicative of material point failure (reaches a value ≈ 1 on the total loss of integrity). In this regard, the failure-zone averaging scheme proposed in Nguyen et al. (2010) offers a good starting point. Another extension could be the incorporation of weak micro-periodicity constraints (or weakly periodic boundary conditions) proposed in Larsson et al. (2011), in order to circumvent the enforcement of periodic fractures. The RVE problems in this manuscript were of saddle point nature, owing to the use of Lagrange multipliers, and were solved using a direct solver. The use of iterative solvers with an exploration into the preconditioning techniques offer yet another research dimension. Finally, the two-scale phase-field fracture framework may be extended to complex multi-physics problems (e.g., fluid flow, cement hydration) and validation studies may be carried out.

7. Software implementation and data

The RVE studies in the Section 4 were carried out in the software package COMSOL Multiphysics 5.5. The multi-scale FE^2 studies in Section 5 were carried out in the open-source software package openFE2 (https://github.com/rbharali/openFE2). Additional data will be made available upon request.

CRediT authorship contribution statement

Ritukesh Bharali: Conceptualisation, Methodology, Software, Formal analysis, Writing - original draft, Writing - review & editing. **Fredrik Larsson:** Conceptualization, Methodology, Supervision, Project administration. **Ralf Jänicke:** Conceptualization, Methodology, Supervision, Project administration, Funding acquisition.

Declaration of competing interest

The authors declare that they have no known competing financial interests or personal relationships that could have appeared to influence the work reported in this paper.

Acknowledgements

The authors would like to acknowledge the financial support from the Swedish Research Council for Sustainable Development (FORMAS) under Grant 2018-01249 and the Swedish Research Council (VR) under Grant 2017-05192.

Appendix A. Hill–Mandel macro-homogeneity

The Hill–Mandel macro-homogeneity condition establishes the coupling (bridging) between the smooth macro-scale and sub-scale through energy equivalence (Hill, 1963, 1984; Nemat-Nasser, 1999). To this end, the RVE weak periodicity problem is re-stated:

$$\langle \boldsymbol{\sigma} : \boldsymbol{\epsilon}[\delta\mathbf{u}]\rangle_{\square} - \frac{1}{|\Omega_{\square}|} \times \int_{\Gamma^{+}_{\square}} \lambda^{(u)} \cdot [\![\delta\mathbf{u}]\!]\, \mathrm{d}\Gamma = 0 \quad \forall\, \delta\mathbf{u} \in \mathbb{U}_{\square}, \tag{A.1a}$$

$$\langle \boldsymbol{\gamma} \cdot \boldsymbol{\nabla}\delta\varphi\rangle_{\square} + \langle \boldsymbol{\Phi}\delta\varphi\rangle_{\square} - \frac{1}{|\Omega_{\square}|}\int_{\Omega_{\square}} \bar{\mu}^{(\varphi)}\delta\varphi\, \mathrm{d}\Omega - \frac{1}{|\Omega_{\square}|} \times \int_{\Gamma^{+}_{\square}} \lambda^{(\varphi)} \cdot [\![\delta\varphi]\!]\, \mathrm{d}\Gamma = 0 \quad \forall\, \delta\varphi \in \mathbb{P}_{\square}, \tag{A.1b}$$

$$-\frac{1}{|\Omega_{\square}|}\int_{\Gamma^{+}_{\square}} \delta\lambda^{(u)} \cdot [\![\mathbf{u}]\!]\, \mathrm{d}\Gamma = -\frac{1}{|\Omega_{\square}|} \times \int_{\Gamma^{+}_{\square}} \delta\lambda^{(u)} \cdot \mathbf{u}^{\mathrm{M}}\, \mathrm{d}\Gamma : \bar{\boldsymbol{\epsilon}} \quad \forall\, \delta\lambda^{(u)} \in \mathbb{T}_{\square}, \tag{A.1c}$$

$$-\frac{1}{|\Omega_{\square}|}\int_{\Gamma^{+}_{\square}} \delta\lambda^{(\varphi)} \cdot [\![\varphi]\!]\, \mathrm{d}\Gamma = -\frac{1}{|\Omega_{\square}|} \times \int_{\Gamma^{+}_{\square}} \delta\lambda^{(\varphi)} \cdot \varphi^{\mathrm{M}}\, \mathrm{d}\Gamma \cdot \bar{\boldsymbol{\xi}} \quad \forall\, \delta\lambda^{(\varphi)} \in \mathbb{Q}_{\square}, \tag{A.1d}$$

$$-\delta\bar{\mu}^{(\varphi)}\langle\varphi\rangle_{\square} = -\delta\bar{\mu}^{(\varphi)}\bar{\varphi} \quad \forall\, \delta\bar{\mu}^{(\varphi)} \in \mathbb{R}, \tag{A.1e}$$

with

$$\mathbf{u}^{\mathrm{M}} = \bar{\boldsymbol{\epsilon}} \cdot [\mathbf{x} - \bar{\mathbf{x}}], \tag{A.2a}$$

$$\varphi^{\mathrm{M}} = \bar{\varphi} + \bar{\boldsymbol{\xi}} \cdot [\mathbf{x} - \bar{\mathbf{x}}]. \tag{A.2b}$$

Moreover, using (25a)–(25d), and the perturbations

$$\mathrm{d}\mathbf{u}^{\mathrm{M}} = \mathrm{d}\bar{\boldsymbol{\epsilon}} \cdot [\mathbf{x} - \bar{\mathbf{x}}], \tag{A.3a}$$

$$\mathrm{d}\varphi^{\mathrm{M}} = \mathrm{d}\bar{\varphi} + d\bar{\boldsymbol{\xi}} \cdot [\mathbf{x} - \bar{\mathbf{x}}], \tag{A.3b}$$

in (A.1c)–(A.1e) yields

$$\bar{\boldsymbol{\sigma}} : \mathrm{d}\bar{\boldsymbol{\epsilon}} = \langle \boldsymbol{\sigma} : \boldsymbol{\epsilon}[\mathrm{d}\mathbf{u}^{\mathrm{M}}]\rangle_{\square}, \tag{A.4a}$$

$$\bar{\boldsymbol{\Phi}}\mathrm{d}\bar{\varphi} + \bar{\mathbf{Q}} \cdot \mathrm{d}\bar{\boldsymbol{\xi}} = \langle \boldsymbol{\Phi}\mathrm{d}\varphi^{\mathrm{M}}\rangle_{\square}, \tag{A.4b}$$

$$\bar{\boldsymbol{\gamma}} \cdot \mathrm{d}\bar{\boldsymbol{\xi}} = \langle \boldsymbol{\gamma} \cdot \mathrm{d}\boldsymbol{\xi}^{\mathrm{M}}\rangle_{\square}. \tag{A.4c}$$

Furthermore, the constraint Eqs. (A.1c)–(A.1e) are re-formulated in the rate form as

$$-\frac{1}{|\Omega_{\square}|}\int_{\Gamma^{+}_{\square}} \delta\lambda^{(u)} \cdot [\![\mathrm{d}\mathbf{u}]\!]\, \mathrm{d}\Gamma = -\frac{1}{|\Omega_{\square}|} \times \int_{\Gamma^{+}_{\square}} \delta\lambda^{(u)} \cdot \mathrm{d}\mathbf{u}^{\mathrm{M}}\, \mathrm{d}\Gamma : \bar{\boldsymbol{\epsilon}} \quad \forall\, \delta\lambda^{(u)} \in \mathbb{T}_{\square}, \tag{A.5a}$$

$$-\frac{1}{|\Omega_{\square}|}\int_{\Gamma^{+}_{\square}} \delta\lambda^{(\varphi)} \cdot [\![\mathrm{d}\varphi]\!]\, \mathrm{d}\Gamma = -\frac{1}{|\Omega_{\square}|} \times \int_{\Gamma^{+}_{\square}} \delta\lambda^{(\varphi)} \cdot \mathrm{d}\varphi^{\mathrm{M}}\, \mathrm{d}\Gamma \cdot \bar{\boldsymbol{\xi}} \quad \forall\, \delta\lambda^{(\varphi)} \in \mathbb{Q}_{\square}, \tag{A.5b}$$

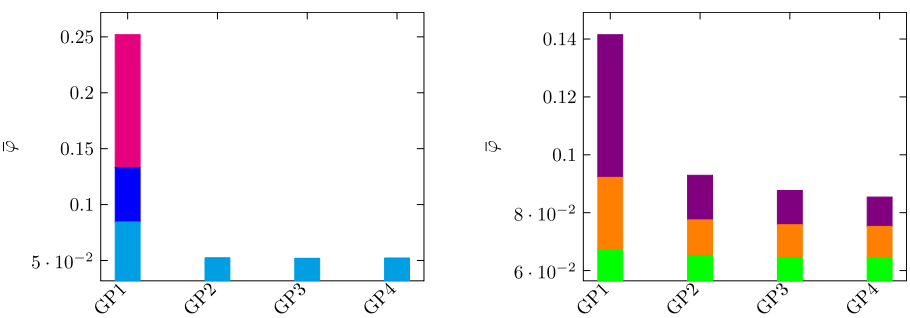

(a) SH (b) VA

Fig. 15. Figures showing the macro-scale phase-field $\bar{\varphi}$ at the macro-scale Gauss Points (GP) for the Selective Homogenisation (SH) and Volume-Average (VA) based two-scale phase-field fracture model. GP1 and GP4 belong to the elements closest and farthest to the fixed boundary respectively. Furthermore, the colour in the bar plot correspond to the markers in Fig. 14. For the selective homogenisation model, $\bar{\varphi}$ is computed as a post-processing quantity. (For interpretation of the references to colour in this figure legend, the reader is referred to the web version of this article.)

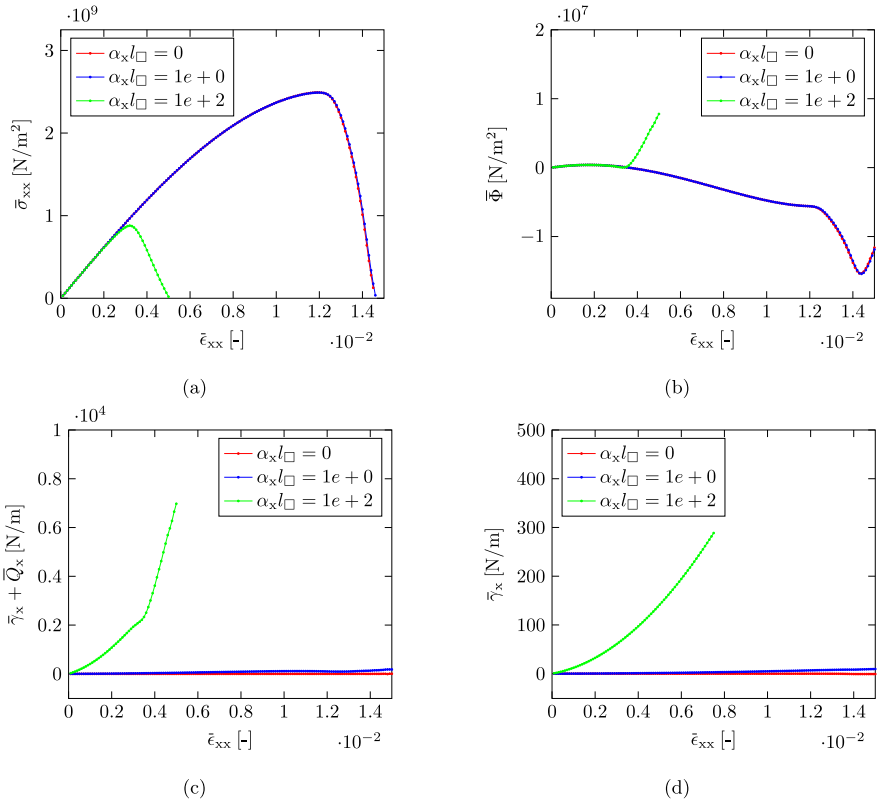

Fig. B.1. Figure showing homogenised macro-scale terms defined in (25a)–(25d) for the volume-average based two-scale phase-field fracture model. (For interpretation of the references to colour in this figure legend, the reader is referred to the web version of this article.)

$$-\delta\bar{\mu}^{(\varphi)}\langle \mathrm{d}\varphi\rangle_\square = -\delta\bar{\mu}^{(\varphi)}\mathrm{d}\bar{\varphi} \quad \forall\, \delta\bar{\mu}^{(\varphi)} \in \mathbb{R}. \tag{A.5c}$$

The macroscopic power for the two-scale phase-field fracture given by

$$\bar{\boldsymbol{\sigma}} : \mathrm{d}\bar{\boldsymbol{\epsilon}} + \bar{\Phi}\mathrm{d}\bar{\varphi} + \bar{\mathbf{Q}}\cdot\mathrm{d}\bar{\boldsymbol{\zeta}} + \bar{\boldsymbol{\gamma}}\cdot\mathrm{d}\bar{\boldsymbol{\zeta}} = \langle \boldsymbol{\sigma} : \boldsymbol{\epsilon}[\mathrm{d}\mathbf{u}^{\mathrm{M}}]\rangle_\square + \langle \Phi \mathrm{d}\varphi^{\mathrm{M}}\rangle_\square + \langle \boldsymbol{\gamma}\cdot\mathrm{d}\boldsymbol{\zeta}^{\mathrm{M}}\rangle_\square, \tag{A.6a}$$

using (A.4a)–(A.4c). Using $\delta\mathbf{u} = \mathrm{d}\mathbf{u}^{\mathrm{M}}$ and $\delta\varphi = \mathrm{d}\varphi^{\mathrm{M}}$ in (A.1a) and (A.1b) gives

$$\begin{aligned}\langle \boldsymbol{\sigma} : \boldsymbol{\epsilon}[\mathrm{d}\mathbf{u}^{\mathrm{M}}]\rangle_\square + \langle \Phi \mathrm{d}\varphi^{\mathrm{M}}\rangle_\square + \langle \boldsymbol{\gamma}\cdot\mathrm{d}\boldsymbol{\zeta}^{\mathrm{M}}\rangle_\square = {} & \frac{1}{|\Omega_\square|}\int_{\Gamma^+_\square} \lambda^{(u)}\cdot[\![\mathrm{d}\mathbf{u}^{\mathrm{M}}]\!]\,\mathrm{d}\Gamma \\ & + \frac{1}{|\Omega_\square|}\int_{\Omega_\square} \bar{\mu}^{(\varphi)}\mathrm{d}\varphi^{\mathrm{M}}\,\mathrm{d}\Omega \\ & + \frac{1}{|\Omega_\square|}\int_{\Gamma^+_\square} \lambda^{(\varphi)} \\ & \cdot[\![\mathrm{d}\varphi^{\mathrm{M}}]\!]\,\mathrm{d}\Gamma,\end{aligned} \tag{A.6b}$$

Utilising the constraint equations in rate form (A.5a)– (A.5c) together with (A.6a) and (A.6b) results in

$$\begin{aligned}\bar{\boldsymbol{\sigma}} : \mathrm{d}\bar{\boldsymbol{\epsilon}} + \bar{\Phi}\mathrm{d}\bar{\varphi} + \bar{\mathbf{Q}}\cdot\mathrm{d}\bar{\boldsymbol{\zeta}} + \bar{\boldsymbol{\gamma}}\cdot\mathrm{d}\bar{\boldsymbol{\zeta}} = {} & \frac{1}{|\Omega_\square|}\int_{\Gamma^+_\square} \lambda^{(u)}\cdot[\![\mathrm{d}\mathbf{u}]\!]\,\mathrm{d}\Gamma \\ & + \frac{1}{|\Omega_\square|}\int_{\Gamma^+_\square} \lambda^{(\varphi)}\cdot[\![\mathrm{d}\varphi]\!]\,\mathrm{d}\Gamma + \bar{\mu}^{(\varphi)}\langle \mathrm{d}\varphi\rangle_\square,\end{aligned} \tag{A.6c}$$

with $\delta\lambda^{(u)} = \lambda^{(u)}$, $\delta\lambda^{(\varphi)} = \lambda^{(\varphi)}$ and $\delta\bar{\mu}^{(\varphi)} = \bar{\mu}^{(\varphi)}$.

Finally, on choosing $\delta\mathbf{u} = \mathrm{d}\mathbf{u}$ and $\delta\varphi = \mathrm{d}\varphi$ in (A.1a) and (A.1b) results in the RVE power expression

$$\bar{\boldsymbol{\sigma}} : \mathrm{d}\bar{\boldsymbol{\epsilon}} + \bar{\Phi}\mathrm{d}\bar{\varphi} + \bar{\mathbf{Q}}\cdot\mathrm{d}\bar{\boldsymbol{\zeta}} + \bar{\boldsymbol{\gamma}}\cdot\mathrm{d}\bar{\boldsymbol{\zeta}} = \langle \boldsymbol{\sigma} : \boldsymbol{\epsilon}[\mathrm{d}\mathbf{u}]\rangle_\square + \langle \Phi \mathrm{d}\varphi\rangle_\square + \langle \boldsymbol{\gamma}\cdot\mathrm{d}\boldsymbol{\zeta}\rangle_\square. \tag{A.6d}$$

This concludes the Hill–Mandel macro-homogeneity proof.

Appendix B. Bounds on the macro-scale phase-field gradient

In this section, the bounds for the macro-scale phase-field gradient is established that ensures that the RVE response remains realistic. To this end, Fig. B.1 presents the homogenised dual quantities pertaining to the volume-averaged two-scale phase-field fracture model with arbitrarily chosen α_x, while α_y is set to zero. The homogenised dual quantities are defined in (25a)–(25d).

It is observed that for $\alpha_x = 1e+2$ (green curve), the post-peak branch develops sooner compared to $\alpha_x = 0$ and $1e+0$. This behaviour is attributed to unrealistic phase-field values at the RVE boundaries, evident from Fig. B.2a. The phase-field $\varphi \notin [0, 1]$, and as such the simulation results are bogus. This observation asserts the fact that in a 'single-scale' RVE analysis, the macro-scale phase-field gradient cannot be chosen arbitrarily for a parametric study. Rather, the macro-scale phase-field gradient must be chosen such that, $\varphi \in [0, 1]$, everywhere in the RVE domain.

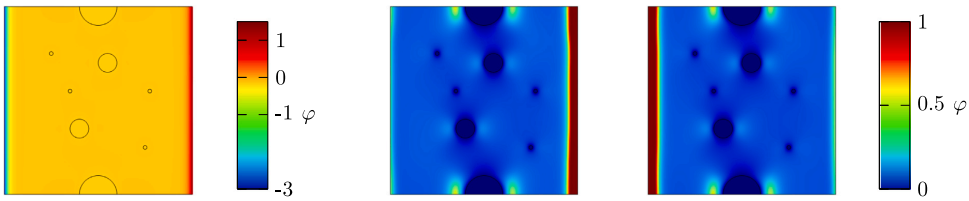

(a) $\alpha_x = 1e + 2.$ (b) $\alpha_x = 2e + 0$ (c) $\alpha_x = -2e + 0$

Fig. B.2. Figure showing phase-field fracture patterns for varying α_x, with α_y set to zero. For Figures (b) and (c), refer to the legend on the extreme right. (For interpretation of the references to colour in this figure legend, the reader is referred to the web version of this article.)

The parametrisation of the macro-scale phase-field gradient may be carried out adopting a trial and error method to arrive at a set of admissible values of α_x and α_y. However, such a procedure could be tedious in the absence of a good initial guess. This problem is circumvented using the DBC for the φ (36b), and requiring $\varphi \in [0, 1]$ everywhere on the RVE boundary. This results in

$$-\frac{2}{l_\square} \leq (\alpha_x + \alpha_y) \leq \frac{2}{l_\square}, \tag{B.1}$$

where, $l_\square$ denotes the RVE edge length. Note that, (B.1) ensures $\varphi \in [0, 1]$ strictly, only in the case of DBC. For other boundary conditions, choosing α_x and α_y based on (B.1) serves as an initial guess. For instance, in the case of SPBC, $\alpha_x = \pm 2$ [mm^{-1}] and $\alpha_y = 0$ result in the fracture patterns shown in Figs. B.2b and B.2c. From the mathematical point of view, these fracture patterns are acceptable as $\varphi \in [0, 1]$. However, from the physical point of view, the chosen α_x and α_y would result in a vertical edge fracture irrespective of the RVE topology and material constituents, which is unrealistic.

References

Alessi, R., Marigo, J.-J., Vidoli, S., 2015. Gradient damage models coupled with plasticity: Variational formulation and main properties. Mech. Mater. 80, 351–367. http://dx.doi.org/10.1016/j.mechmat.2013.12.005, Materials and Interfaces.

Ambati, M., Gerasimov, T., De Lorenzis, L., 2015. Phase-field modeling of ductile fracture. Comput. Mech. 55 (5), 1017–1040. http://dx.doi.org/10.1007/s00466-015-1151-4.

Borden, M.J., Verhoosel, C.V., Scott, M.A., Hughes, T.J., Landis, C.M., 2012. A phase-field description of dynamic brittle fracture. Comput. Methods Appl. Mech. Engrg. 217–220, 77–95. http://dx.doi.org/10.1016/j.cma.2012.01.008, URL: http://www.sciencedirect.com/science/article/pii/S0045782512000199.

de Borst, R., Sluys, L.-J., Muhlhaus, H., Pamin, J., 1993. Fundamental issues in finite element analyses of localization of deformation. Eng. Comput. Int. J. Comput. Aided Eng. 10 (2), 99–121. http://dx.doi.org/10.1108/eb023897.

Bourdin, B., 2007. Numerical implementation of the variational formulation for quasi-static brittle fracture. Interfaces Free Bound. 9, 411–430. http://dx.doi.org/10.4171/IFB/171.

Bourdin, B., Francfort, G., Marigo, J.-J., 2000. Numerical experiments in revisited brittle fracture. J. Mech. Phys. Solids 48 (4), 797–826. http://dx.doi.org/10.1016/S0022-5096(99)00028-9.

Burke, S., Ortner, C., Süli, E., 2010. An adaptive finite element approximation of a variational model of brittle fracture. SIAM J. Numer. Anal. 48 (3), 980–1012. http://dx.doi.org/10.1137/080741033.

Cajuhi, T., Sanavia, L., De Lorenzis, L., 2018. Phase-field modeling of fracture in variably saturated porous media. Comput. Mech. 61 (3), 299–318. http://dx.doi.org/10.1007/s00466-017-1459-3.

Fantoni, F., Bacigalupo, A., Paggi, M., Reinoso, J., 2019. A phase field approach for damage propagation in periodic microstructured materials. Int. J. Fract. http://dx.doi.org/10.1007/s10704-019-00400-x.

Feyel, F., 1999. Multiscale FE2 elastoviscoplastic analysis of composite structures. Comput. Mater. Sci. 16 (1), 344–354. http://dx.doi.org/10.1016/S0927-0256(99)00077-4.

Francfort, G., Marigo, J.-J., 1998. Revisiting brittle fracture as an energy minimization problem. J. Mech. Phys. Solids 46 (8), 1319–1342. http://dx.doi.org/10.1016/S0022-5096(98)00034-9.

Gerasimov, T., De Lorenzis, L., 2016. A line search assisted monolithic approach for phase-field computing of brittle fracture. Comput. Methods Appl. Mech. Engrg. 312, 276–303. http://dx.doi.org/10.1016/j.cma.2015.12.017.

Gerasimov, T., De Lorenzis, L., 2019. On penalization in variational phase-field models of brittle fracture. Comput. Methods Appl. Mech. Engrg. 354, 990–1026. http://dx.doi.org/10.1016/j.cma.2019.05.038.

Gitman, I., Askes, H., Sluys, L., 2007. Representative volume: Existence and size determination. Eng. Fract. Mech. 74 (16), 2518–2534. http://dx.doi.org/10.1016/j.engfracmech.2006.12.021.

Griffith, A.A., Taylor, G.I., 1921. VI. The phenomena of rupture and flow in solids. Phil. Trans. R. Soc. Lond. Ser. A, 221 (582–593), 163–198. http://dx.doi.org/10.1098/rsta.1921.0006.

He, B., Schuler, L., Newell, P., 2020. A numerical-homogenization based phase-field fracture modeling of linear elastic heterogeneous porous media. Comput. Mater. Sci. 176, 109519. http://dx.doi.org/10.1016/j.commatsci.2020.109519.

Heister, T., Wheeler, M.F., Wick, T., 2015. A primal-dual active set method and predictor-corrector mesh adaptivity for computing fracture propagation using a phase-field approach. Comput. Methods Appl. Mech. Engrg. http://dx.doi.org/10.1016/j.cma.2015.03.009.

Hill, R., 1963. Elastic properties of reinforced solids: Some theoretical principles. J. Mech. Phys. Solids 11 (5), 357–372. http://dx.doi.org/10.1016/0022-5096(63)90036-X.

Hill, R., 1984. On macroscopic effects of heterogeneity in elastoplastic media at finite strain. Math. Proc. Camb. Phil. Soc. 95 (3), 481–494. http://dx.doi.org/10.1017/S0305004100061818.

Hintermüller, M., Ito, K., Kunisch, K., 2002. The primal-dual active set strategy as a semismooth Newton method. SIAM J. Optim. 13 (3), 865–888. http://dx.doi.org/10.1137/S1052623401383558.

Hughes, T.J., Feijóo, G.R., Mazzei, L., Quincy, J.-B., 1998. The variational multiscale method—a paradigm for computational mechanics. Comput. Methods Appl. Mech. Engrg. 166 (1), 3–24. http://dx.doi.org/10.1016/S0045-7825(98)00079-6, Advances in Stabilized Methods in Computational Mechanics.

Irwin, G., 1957. Analysis of stresses and strains near the end of a crack traversing a plate. J. Appl. Mech. Trans. ASME E24, 351–369.

Jänicke, R., Larsson, F., Runesson, K., 2020. A poro-viscoelastic substitute model of fine-scale poroelasticity obtained from homogenization and numerical model reduction. Comput. Mech. http://dx.doi.org/10.1007/s00466-019-01808-x.

Klinsmann, M., Rosato, D., Kamlah, M., McMeeking, R.M., 2015. An assessment of the phase field formulation for crack growth. Comput. Methods Appl. Mech. Engrg. 294, 313–330. http://dx.doi.org/10.1016/j.cma.2015.06.009.

Larsson, F., Runesson, K., Saroukhani, S., Vafadari, R., 2011. Computational homogenization based on a weak format of micro-periodicity for RVE-problems. Comput. Methods Appl. Mech. Engrg. 200 (1), 11–26. http://dx.doi.org/10.1016/j.cma.2010.06.023.

Larsson, F., Runesson, K., Su, F., 2010a. Computational homogenization of uncoupled consolidation in micro-heterogeneous porous media. Int. J. Numer. Anal. Methods Geomech. 34 (14), 1431–1458. http://dx.doi.org/10.1002/nag.862.

Larsson, F., Runesson, K., Su, F., 2010b. Variationally consistent computational homogenization of transient heat flow. Internat. J. Numer. Methods Engrg. 81 (13), 1659–1686. http://dx.doi.org/10.1002/nme.2747.

Lee, S., Wheeler, M.F., Wick, T., Srinivasan, S., 2017. Initialization of phase-field fracture propagation in porous media using probability maps of fracture networks.. Mech. Res. Commun. 80, 16–23. http://dx.doi.org/10.1016/j.mechrescom.2016.04.002.

Martínez-Pañeda, E., Golahmar, A., Niordson, C.F., 2018. A phase field formulation for hydrogen assisted cracking. Comput. Methods Appl. Mech. Engrg. 342, 742–761. http://dx.doi.org/10.1016/j.cma.2018.07.021.

May, S., Vignollet, J., de Borst, R., 2015. A numerical assessment of phase-field models for brittle and cohesive fracture: *Gamma*-convergence and stress oscillations. Eur. J. Mech. A Solids 52, 72–84. http://dx.doi.org/10.1016/j.euromechsol.2015.02.002.

Mesgarnejad, A., Bourdin, B., Khonsari, M., 2013. A variational approach to the fracture of brittle thin films subject to out-of-plane loading. J. Mech. Phys. Solids 61 (11), 2360–2379. http://dx.doi.org/10.1016/j.jmps.2013.05.001.

Miehe, C., Aldakheel, F., Raina, A., 2016. Phase field modeling of ductile fracture at finite strains: A variational gradient-extended plasticity-damage theory. Int. J. Plast. 84, 1–32. http://dx.doi.org/10.1016/j.ijplas.2016.04.011.

Miehe, C., Hofacker, M., Schänzel, L.M., Aldakheel, F., 2015a. Phase field modeling of fracture in multi-physics problems. Part II. coupled brittle-to-ductile failure criteria and crack propagation in thermo-elastic-plastic solids. Comput. Methods Appl. Mech. Engrg. 294, 486–522. http://dx.doi.org/10.1016/j.cma.2014.11.017.

Miehe, C., Hofacker, M., Welschinger, F., 2010a. A phase field model for rate-independent crack propagation: Robust algorithmic implementation based on operator splits. Comput. Methods Appl. Mech. Engrg. 199 (45–48), 2765–2778. http://dx.doi.org/10.1016/j.cma.2010.04.011.

Miehe, C., Mauthe, S., 2016. Phase field modeling of fracture in multi-physics problems. Part III. crack driving forces in hydro-poro-elasticity and hydraulic fracturing of fluid-saturated porous media. Comput. Methods Appl. Mech. Engrg. 304, 619–655. http://dx.doi.org/10.1016/j.cma.2015.09.021.

Miehe, C., Schänzel, L.M., Ulmer, H., 2015b. Phase field modeling of fracture in multi-physics problems. Part i. balance of crack surface and failure criteria for brittle crack propagation in thermo-elastic solids. Comput. Methods Appl. Mech. Engrg. 294, 449–485. http://dx.doi.org/10.1016/j.cma.2014.11.016.

Miehe, C., Welschinger, F., Hofacker, M., 2010b. Thermodynamically consistent phase-field models of fracture: Variational principles and multi-field FE implementations. Internat. J. Numer. Methods Engrg. 83 (10), 1273–1311. http://dx.doi.org/10.1002/nme.2861.

Mikelić, A., Wheeler, M.F., Wick, T., 2019. Phase-field modeling through iterative splitting of hydraulic fractures in a poroelastic medium. GEM - International Journal on Geomathematics, Vol. 10. Springer International Publishing, ISBN: 0123456789, http://dx.doi.org/10.1007/s13137-019-0113-y.

Mumford, D., Shah, J., 1989. Optimal approximations by piecewise smooth functions and associated variational problems. Comm. Pure Appl. Math. 42 (5), 577–685. http://dx.doi.org/10.1002/cpa.3160420503.

Nagaraja, S., Elhaddad, M., Ambati, M., Kollmannsberger, S., De Lorenzis, L., Rank, E., 2019. Phase-field modeling of brittle fracture with multi-level hp-FEM and the finite cell method. Comput. Mech. 63 (6), 1283–1300. http://dx.doi.org/10.1007/s00466-018-1649-7.

Nemat-Nasser, S., 1999. Averaging theorems in finite deformation plasticity. Mech. Mater. 31 (8), 493–523. http://dx.doi.org/10.1016/S0167-6636(98)00073-8.

Nguyen, V.P., Lloberas-Valls, O., Stroeven, M., Sluys, L.J., 2010. On the existence of representative volumes for softening quasi-brittle materials – a failure zone averaging scheme. Comput. Methods Appl. Mech. Engrg. 199 (45), 3028–3038. http://dx.doi.org/10.1016/j.cma.2010.06.018.

Nguyen, T.T., Réthoré, J., Baietto, M.-C., 2017. Phase field modelling of anisotropic crack propagation. Eur. J. Mech. A Solids 65, 279–288. http://dx.doi.org/10.1016/j.euromechsol.2017.05.002.

Ohman, M., Larsson, F., Runesson, K., 2013. Computational homogenization of liquid-phase sintering with seamless transition from macroscopic compressibility to incompressibility. Comput. Methods Appl. Mech. Engrg. 266, 219–228. http://dx.doi.org/10.1016/j.cma.2013.07.006.

Ostoja-Starzewski, M., 2006. Material spatial randomness: From statistical to representative volume element. Probab. Eng. Mech. 21 (2), 112–132. http://dx.doi.org/10.1016/j.probengmech.2005.07.007.

Patil, R., Mishra, B., Singh, I., 2018a. An adaptive multiscale phase field method for brittle fracture. Comput. Methods Appl. Mech. Engrg. 329, 254–288. http://dx.doi.org/10.1016/j.cma.2017.09.021.

Patil, R., Mishra, B., Singh, I., 2019. A multiscale framework based on phase field method and XFEM to simulate fracture in highly heterogeneous materials. Theor. Appl. Fract. Mech. 100, 390–415. http://dx.doi.org/10.1016/j.tafmec.2019.02.002.

Patil, R., Mishra, B., Singh, I., Bui, T., 2018b. A new multiscale phase field method to simulate failure in composites. Adv. Eng. Softw. 126, 9–33. http://dx.doi.org/10.1016/j.advengsoft.2018.08.010.

Pollmann, N., Larsson, F., Runesson, K., Janicke, R., 2020. Diffuse interface modeling and variationally consistent homogenization of fluid transport in fractured porous media. Eur. J. Mech. A Solids 84, 104067. http://dx.doi.org/10.1016/j.euromechsol.2020.104067, URL: http://www.sciencedirect.com/science/article/pii/S0997753820304551.

Runesson, K., Ekh, M., Larsson, F., 2017. Computational homogenization of mesoscale gradient viscoplasticity. Comput. Methods Appl. Mech. Engrg. 317, 927–951. http://dx.doi.org/10.1016/j.cma.2016.11.032.

Sandstrom, C., Larsson, F., 2013. Variationally consistent homogenization of Stokes flow in porous media. Int. J. Multiscale Comput. Eng. 11 (2), 117–138. http://dx.doi.org/10.1615/IntJMultCompEng.2012004069.

Sandstrom, C., Larsson, F., Runesson, K., Johansson, H., 2013. A two-scale finite element formulation of Stokes flow in porous media. Comput. Methods Appl. Mech. Engrg. 261–262, 96–104. http://dx.doi.org/10.1016/j.cma.2013.03.025.

Svenning, E., Fagerstr, M., Larsson, F., 2016a. Computational homogenization of microfractured continua using weakly periodic boundary conditions. Comput. Methods Appl. Mech. Engrg. 299, 1–21. http://dx.doi.org/10.1016/j.cma.2015.10.014.

Svenning, E., Fagerström, M., Larsson, F., 2016b. On computational homogenization of microscale crack propagation. Internat. J. Numer. Methods Engrg. 108 (1), 76–90. http://dx.doi.org/10.1002/nme.5220.

Svenning, E., Larsson, F., Fagerström, M., 2017. Two-scale modeling of fracturing solids using a smeared macro-to-micro discontinuity transition. Comput. Mech. 60 (4), 627–641. http://dx.doi.org/10.1007/s00466-017-1426-z.

Wick, T., 2016. Goal functional evaluations for phase-field fracture using PU-based dwr mesh adaptivity. Comput. Mech. 57 (6), 1017–1035. http://dx.doi.org/10.1007/s00466-016-1275-1.

Wick, T., 2017a. An error-oriented Newton/inexact augmented Lagrangian approach for fully monolithic phase-field fracture propagation. SIAM J. Sci. Comput. 39 (4), B589–B617. http://dx.doi.org/10.1137/16m1063873.

Wick, T., 2017b. Modified Newton methods for solving fully monolithic phase-field quasi-static brittle fracture propagation. Comput. Methods Appl. Mech. Engrg. http://dx.doi.org/10.1016/j.cma.2017.07.026.

Wilson, Z.A., Landis, C.M., 2016. Phase-field modeling of hydraulic fracture. J. Mech. Phys. Solids 96, 264–290. http://dx.doi.org/10.1016/j.jmps.2016.07.019.

Zhou, S., Zhuang, X., Rabczuk, T., 2018. A phase-field modeling approach of fracture propagation in poroelastic media. Eng. Geol. 240 (March), 189–203. http://dx.doi.org/10.1016/j.enggeo.2018.04.008.